



National Library
of Canada

Acquisitions and
Bibliographic Services Branch

395 Wellington Street
Ottawa, Ontario
K1A 0N4

Bibliothèque nationale
du Canada

Direction des acquisitions et
des services bibliographiques

395, rue Wellington
Ottawa (Ontario)
K1A 0N4

Your No. Votre référence

Our No. Notre référence

NOTICE

The quality of this microform is heavily dependent upon the quality of the original thesis submitted for microfilming. Every effort has been made to ensure the highest quality of reproduction possible.

If pages are missing, contact the university which granted the degree.

Some pages may have indistinct print especially if the original pages were typed with a poor typewriter ribbon or if the university sent us an inferior photocopy.

Reproduction in full or in part of this microform is governed by the Canadian Copyright Act, R.S.C. 1970, c. C-30, and subsequent amendments.

AVIS

La qualité de cette microforme dépend grandement de la qualité de la thèse soumise au microfilmage. Nous avons tout fait pour assurer une qualité supérieure de reproduction.

S'il manque des pages, veuillez communiquer avec l'université qui a conféré le grade.

La qualité d'impression de certaines pages peut laisser à désirer, surtout si les pages originales ont été dactylographiées à l'aide d'un ruban usé ou si l'université nous a fait parvenir une photocopie de qualité inférieure.

La reproduction, même partielle, de cette microforme est soumise à la Loi canadienne sur le droit d'auteur, SRC 1970, c. C-30, et ses amendements subséquents.

Canada

University of Alberta

Radial Array Slab Laser Excitation With A Resonant Cavity

by

Walter D. Bilida



**A thesis submitted to the Faculty of Graduate Studies and Research in partial
fulfillment of the requirements for the degree of Doctor of Philosophy**

Department of Electrical Engineering

Edmonton, Alberta

Spring, 1996



National Library
of Canada

Acquisitions and
Bibliographic Services Branch

395 Wellington Street
Ottawa, Ontario
K1A 0N4

Bibliothèque nationale
du Canada

Direction des acquisitions et
des services bibliographiques

395, rue Wellington
Ottawa (Ontario)
K1A 0N4

Your file / Votre référence

Our file / Notre référence

The author has granted an irrevocable non-exclusive licence allowing the National Library of Canada to reproduce, loan, distribute or sell copies of his/her thesis by any means and in any form or format, making this thesis available to interested persons.

L'auteur a accordé une licence irrévocable et non exclusive permettant à la Bibliothèque nationale du Canada de reproduire, prêter, distribuer ou vendre des copies de sa thèse de quelque manière et sous quelque forme que ce soit pour mettre des exemplaires de cette thèse à la disposition des personnes intéressées.

The author retains ownership of the copyright in his/her thesis. Neither the thesis nor substantial extracts from it may be printed or otherwise reproduced without his/her permission.

L'auteur conserve la propriété du droit d'auteur qui protège sa thèse. Ni la thèse ni des extraits substantiels de celle-ci ne doivent être imprimés ou autrement reproduits sans son autorisation.

ISBN 0-612-10573-3

Canada

University of Alberta
Library Release Form

Name of Author: Walter David Bilida

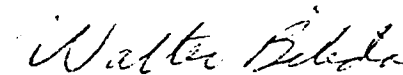
Title of Thesis: Radial Array Slab Laser Excitation With A Resonant Cavity

Degree: Doctor of Philosophy

Year this Degree Granted: 1996

Permission is hereby granted to the University of Alberta Library to reproduce single copies of this thesis and to lend or sell such copies for private, scholarly, or scientific research purposes only.

The author reserves all other publication and other rights in association with the copyright in the thesis, and except as hereinbefore provided, neither the thesis nor any substantial portion thereof may be printed or otherwise reproduced in any material form whatsoever without the author's prior written permission.



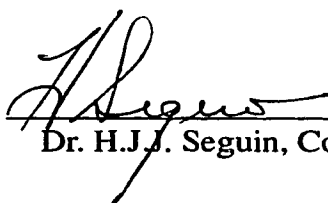
Walter Bilida
Apt. 401 17327-69 ave.
Edmonton Alberta T5T 3S9

29 January 1996


University of Alberta

Faculty of Graduate Studies and Research

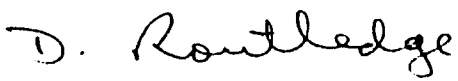
The undersigned certify that they have read, and recommend to the Faculty of Graduate Studies and Research for acceptance, a thesis entitled Radial Array Slab Laser Excitation With A Resonant Cavity submitted by Walter D. Bilida in partial fulfillment of the requirements for the degree of Doctor of Philosophy.



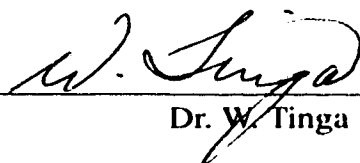
Dr. H.J.J. Seguin, Co-Supervisor



Dr. C.E. Capjack, Co-Supervisor



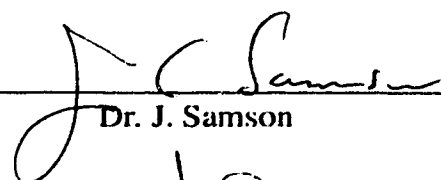
Dr. D. Routledge



Dr. W. Tinga



Dr. F. Vermeulen



Dr. J. Samson



Dr. G. Enright, External Examiner

Date 29 JAN 96

Dedication

To my family and friends, for all their encouragement and support.

Abstract

Materials processing applications increasingly demand compact, efficient and high power laser systems. Long dominant in materials processing, the carbon dioxide laser has recently undergone significant further advancement in compactness and efficiency. Use of large area, diffusion cooled electrodes, typified by slab lasers, has enabled this important and exciting advancement. Techniques employing excitation of multiple slab discharges all embodied into a single unit have also brought the realm of high output power to these new devices.

This investigation examines the feasibility of driving several slab discharge channels uniformly, and independently but all contained within a single compact laser structure. Initial experiments show that use of a coaxial resonant cavity provides an efficient means of splitting energy from a single RF source, thereby creating a practical technique in scaling this technology to high powers. Power isolation between the load and cavity, necessary for independent RF drive to each laser channel, is also shown.

High cavity Q's, characteristic of resonant cavities, enable extremely high power transfer efficiencies from the source to multiple loads. Efficiencies of 95% have been measured between a single source, and four resistive loads. A theoretical design criterion has been developed for resonant cavities emphasizing: length, loss mechanisms, coupling measurement and techniques, efficiency, and loading effects of magnetically coupled loops.

Power supply development and construction was necessary to drive the laser system. Integration of a high power triode oscillator into the coaxial resonant cavity was accomplished by using a tuned-grid, tuned-plate grid separation oscillator design. Tuned circuitry used resonant cavities, as opposed to normal lumped inductor and capacitor elements. This unorthodox design enabled direct drive of many independent outputs from a single RF source. In addition, this oscillator design makes the generation of a high power RF source much less costly than traditional RF power generators or amplifiers. Output powers of over 25 kW have been achieved thus far, at efficiencies of 65% in Class C operation, while driving 8 gas discharge loads.

Laser power of over 1,200 watts has been extracted from 8 discharge channels, creating the highest power multi-channel slab laser currently in the world. For efficient optical power extraction, a uniform power distribution along the entire length of the planar electrode array was necessary. Data confirming power deposition uniformity of 95% was provided via optical luminosity measurements. Extraction of the laser beamlets showed that a composite beam of radial geometry exhibits circular symmetry, low divergence, and excellent focal properties. These features were derived without benefit of corrective optics, a feature usually necessary on other slab laser systems. The implications and impact of this laser system are enormous as it brings forth the next generation in high power laser development. With lasers of this geometry, the size, and cost of current commercial laser systems will be reduced by an order of magnitude. With a truly portable laser in the 10's of kilowatts range, many new applications will undoubtedly be created.

Acknowledgment

I would like to thank my supervisors Dr. C. E. Capjack, and Dr. H. J. J. Seguin for their support, guidance, and the opportunity to work on such an interesting project.

Additional thanks goes to all the members of this laser research group for their assistance and advice. Mr. H. Reshef for being there to help run the laser system, fabricate optical components, and many other tasks too numerous to mention. Mr. H. Dixel for his expertise and precision in the machine shop, enabling the fabrication of complex components necessary for the success of this project. Mr. V. Pohnert for many of the detailed technical drawings used in this thesis. Mr. K. Rogozinski for the assembly of the cooling system, as well as numerous other tasks. Mr. D. Presakarchuk for keeping the RF power supply running, and all the electrical assembly. Finally thanks goes to Mr. J. Strohschein, and Mr. S. Scott for their countless discussions and advice.

Table of Contents

Chapter 1	1
1.0 Introduction.....	1
1.1 Historical Development of the Carbon Dioxide laser.....	1
1.2 Methods of Excitation.....	2
1.2.1 RF Excitation	3
1.3 Waveguide Lasers.....	9
1.3.1 Hybrid Waveguide Lasers.....	10
1.3.2 Multi-Channel Systems.....	14
Chapter 2.....	19
2.0 Resonant Cavities.....	19
2.1 Half Wavelength Resonators.....	21
2.2 Quarter Wavelength Resonators.....	21
2.3 T Resonators	23
2.4 Determining the Cavity Q.....	23
2.5 Coupling Loading	26
2.6 Material and Dielectric Loading	34
2.7 Coupling Effects upon Power Transfer.....	35
Chapter 3.....	39
3.0 Triode Oscillator	39
3.1 Oscillator Design	41
3.2 Tank and Cavity Circuits.....	45
3.3 Oscillator Operational Characteristics	51
3.3.1 Grid Separation Oscillator Design.....	54
3.3.2 Grid Separation Oscillator Operating Conditions.....	57
Chapter 4.....	65
4.0 Results.....	65
4.1 Discharge Uniformity	66
4.2 Laser Output Power	74

4.2.1	Single Channel Optical Extraction.....	74
4.2.2	Multi-Channel Optical Extraction.....	78
4.3	Optical Resonance	82
4.4	Beam Characteristics	85
4.5	Focal Beam Quality	89
4.6	Radiation Safety.....	93
Chapter 5	96
5.0	Conclusions And Proposals For Future Research.....	96
5.1	Summary Of This Investigation.....	96
5.2	Proposals For Future Research	99
References	101

List of Tables

Table 1.1	Advantages with RF excitation.....	5
Table 2.1	Loop area(cm ²) vs. load impedance and number of loops for Q _L of 10 @ 100 Mhz.....	32
Table 2.2	Loop area vs. frequency for Q _L = 10.....	32
Table 2.3	Theoretical loop area using a loop of 14.6 cm ²	33
Table 2.4	Theoretical loop area using a loop of 44.4 cm ²	34
Table 2.5	Unloaded Q vs. material loading @ 40.68 MHz.	35
Table 2.6	Power transfer into four 50 ohm loads from a resonant cavity with a loaded Q of 38.5.....	38
Table 3.1	Technical data for industrial 3CW45,000H3 triode Class C oscillator.....	54
Table 3.2	Triode operating conditions while driving two 50 ohm loads.....	59
Table 3.3	Operating conditions driving four 50 ohm loads.....	60
Table 3.4	Triode operating conditions while driving two discharge channels @ 80.5 MHz.....	61
Table 3.5	Triode operating conditions while driving five discharge loads @ 80.5 MHz...	62
Table 3.6	Triode operating conditions while driving eight discharge loads @ 80.5 MHz.	62
Table 3.7	Triode optimized operating conditions while driving eight discharge loads @ 80.5 MHz.....	64
Table 4.1	Phase shift for TE ₁ , or TM ₁ mode after 1.06 m propagation with respect to a 3 mm parallel plate waveguide.....	84

List of Figures

Figure 1.1 Energy Level Diagram of a CO ₂ Laser.	4
Figure 1.2 Vibrational Modes in a CO ₂ Molecule (a) unexcited (b) symmetric stretch (c) bending (d) asymmetric stretch.	4
Figure 1.3 Optical Luminosity of an RF Excited Discharge Between the Electrodes.	6
Figure 1.4 Space-Time Structure of an RF Discharge.....	6
Figure 1.5 Plasma and Sheath Voltage-Current Characteristics.....	8
Figure 1.6 Frequency Dependencies on Sheath and Plasma Voltages.	8
Figure 1.7 Slab Waveguide Laser.....	11
Figure 1.8 Slab Waveguide Mode Divergences.	11
Figure 1.9 Near and Far Field Beam Profiles of a Slab Mode.	12
Figure 1.10 Scaling Law for Slab Lasers.	13
Figure 1.11 Triple Slab Laser.	15
Figure 1.12 Phase Locked Mode from a Triple Slab Laser.....	15
Figure 1.13 Eight Channel Zodiac Laser System.....	16
Figure 2.1 Half Wavelength Resonator.	20
Figure 2.2 Quarter Wavelength Resonator.	20
Figure 2.3 T Resonator.	22
Figure 2.4 Equivalent Circuit of a Coaxial Cavity Loaded by a Single Loop.	29
Figure 2.5 Coupling Loop Area(cm ²) vs. Number of Loops and Loop Impedance.....	31
Figure 2.6 Power Transmission Through a 2 Port Cavity.	36
Figure 3.1 Eimac 3CW45,000H3 Triode.....	40
Figure 3.2 Voltage, Current, and Power Relations in a Class C Amplifier.....	43
Figure 3.4 Colpitts Oscillator Circuit.....	46
Figure 3.3 Hartley Oscillator Circuit.....	46
Figure 3.5 Tuned-Grid Tuned-Plate Circuit.	47

Figure 3.6 Two Cavity Grid Separation Oscillator.....	48
Figure 3.7 Electrical Schematic of Two Cavity Grid Separation Oscillator.....	49
Figure 3.8 Schematic of Zodiac Laser System.....	53
Figure 4.1 Radial Slab Electrode Array.....	66
Figure 4.2 End Fed Electrode.....	66
Figure 4.3 Discharge Uniformity Detector.....	69
Figure 4.4 Discharge Luminosity at Various Pressures.....	71
Figure 4.5 Electrical Schematic of Detector Amplifier Circuit.....	71
Figure 4.6 Discharge Uniformity With Two Inductors At 20 Torr Gas Pressure.....	73
Figure 4.7 Four Inductor Discharge Uniformity at 20 Torr Gas Pressure Driven Weakly....	73
Figure 4.8 Four Inductor Discharge Uniformity At 20 Torr Gas Pressure Driven Optimally.....	74
Figure 4.9 Laser Power with 13% Output Coupling.....	76
Figure 4.10 Laser Power with 25% Output Coupling.....	76
Figure 4.11 Laser Power with 35% Output Coupling.....	77
Figure 4.12 Optimum Output Coupling.....	77
Figure 4.13 Theoretical Discharge Uniformity with 4 Inductors at 40 torr Gas Pressure.....	79
Figure 4.14 Loop Placement along Short Circuit Plane.....	80
Figure 4.15 Multi-Channel Laser Power.....	80
Figure 4.16 Comparison Between Single and Multi-Channel Laser Power.....	81
Figure 4.17 Toric Resonator.....	85
Figure 4.18 Near Field Burn Pattern In Plexiglass.....	86
Figure 4.19 Digitized 3-D View Of Near Field Burn Pattern.....	86
Figure 4.20 Far Field Burn Pattern In Plexiglass 3.7 m From Laser.....	88
Figure 4.21 Focal Burn Pattern 12 m From Laser.....	88
Figure 4.22 Zodiac Radiation Profile Side View.....	94

Figure 4.23 Zodiac Radiation Profile Top View.....94
Figure 4.24 Zodiac Laser System.....95

List of Symbols

a	inner radius
A	cross sectional area of the loop
b	outer radius
c	speed of light
C	capacitance
d	electrode separation
E_b	anode or plate DC voltage
E_c	external DC grid bias
E_g	grid voltage
E_L	AC plate voltage
E_{max}	maximum AC grid voltage
E_{min}	minimum AC plate voltage
E_p	plate voltage
E_s	AC grid voltage
f	frequency
g_m	transconductance
G	conductance
I_p	plate current
IL	insertion loss

k	wavenumber
k_c	cutoff wavenumber
K	coupling constant
L	inductance
L_r	length of optical resonator
P	power
Q	quality factor
Q_{ext}	external Q
Q_L	loaded Q
Q_u	unloaded Q
r	radial distance from the cavity to the effective center of the loop
R	resistance
R_e	equivalent resistance in series with the short-circuited resistance of the cavity
R_g	series resistance of the coupling loop
R_p	dynamic plate resistance
R_s	surface resistance
RL	return loss
SWR	standing wave ratio
$\tan\delta$	loss tangent of a dielectric
v_g	group velocity
w	electrode width

W	beam spot size of a real or non ideal laser beam
W_0	beam waist of a non ideal laser beam
X_L	inductive reactance of the loop
X_L	inductive reactance of the cavity
X_M	mutual reactance between the resonant circuit and loop
z_0	Rayleigh range
Z	impedance
Z_0	characteristic impedance of a transmission line
α_c	conductor loss
α_d	dielectric loss
β	propagation constant
γ	complex propagation constant
ϵ	permittivity
Γ	reflection coefficient
δ_s	surface resistivity
η	efficiency of power transfer, or impedance of free space
θ	angular distance the effective center of the loop is from the short circuited plane
θ_g	grid conduction period
θ_p	plate conduction period
λ	wavelength
μ	permeability or amplification factor for a triode

σ	electrical conductivity
ω	angular frequency or beam spot size
ω_0	beam waist

Chapter 1

1.0 Introduction

Since its invention by Patel¹ in 1964, the CO₂ laser has assumed an increasingly important role in scientific, medical and industrial applications. Vast increases in output power, developed over time, have permitted this laser to dominate the materials processing field. Further advancement in compactness, efficiency and reliability guarantee continued dominance of the CO₂ laser in materials processing for the foreseeable future.

This thesis focuses on development of an even more compact high power carbon dioxide laser that is particularly suited to industrial applications. The device features multiple gain channels, mounted in a radial array, and all separately driven from a common RF source. Resonant cavity techniques are employed for both impedance matching and power splitting in this multi-channel system.

A brief discussion of the historical development of the CO₂ laser will be presented, followed by a description of excitation methodologies. Primary emphasis will be on radio frequency techniques. Methods for driving large area discharge channels are discussed, and the scaling of such discharges into multi-channel arrays to achieve very high average power performance is examined.

1.1 Historical Development of the Carbon Dioxide laser

The CO₂ laser was first developed as a continuous wave device. Initial units were of an axial geometry, with little or no gas flow. As laser excitation mechanisms became

better understood, operational efficiencies rose above 10%. Fully optimized systems with efficiencies in excess of 20% were subsequently reported. Notwithstanding these relatively high efficiencies, nearly 80% of the input energy still had to be extracted as waste heat. In early devices, waste heat was removed via diffusion to the outer water-cooled walls of the discharge tube. Since discharge tubes featured a relatively large internal diameter, wall diffusion cooling proved ineffective, thereby yielded only relatively low power devices. Substantial further increases in output power were attained by forced convection cooling, achieved by fast axial flow sub-systems. Unfortunately, these units were much more costly and bulky than their lower power, diffusion cooled counterparts. These aspects limited, in large measure, the potential growth of CO₂ lasers in industry.

Application of radio frequency excitation techniques to the waveguide CO₂ laser developed in 1977², soon became the methodology of choice for output powers in the tens of watts. Apart from ease of usage, the compactness of such systems provided a further desirable operational aspect. Development of large planar RF excited electrode systems made it possible for these simple and reliable devices to achieve much larger average powers. Indeed, next generation devices, such as that described in this thesis, rival fast axial flow lasers in terms of output power.

1.2 Methods of Excitation

Excitation of the upper energy level in a laser device maybe accomplished in several ways, depending upon the type of laser. For solid state lasers, optical pumping is most common. In gas lasers, direct current and radio frequency excitation are the most frequently employed methods.

The CO₂ laser is a 4 level laser, whose energy levels are determined by quantized molecular vibration. Figure 1.1 shows the energy level diagram for such a CO₂ system. Upper and lower lasing levels involve different vibrational modes. These modes, illustrated in Figure 1.2, are the symmetric stretch, bending, and asymmetric stretch. Energy levels are identified as (N 0 0), (0 N 0), and (0 0 N) respectively, where N is an integer representing the degree of excitation. Lasing occurs between the upper laser level (0 0 1) and one of two lower energy levels. The most common, or highest gain, laser transition has a (1 0 0) lower level and radiates at 10.6 μm. A lower gain transition occurs at the second bending mode of (0 2 0) and emits 9.6 μm radiation. In a three level laser, the lower level decays to the ground state, while a four level laser has one more transition. For the CO₂ molecule this intermediate level is the lowest bending mode of (0 1 0). This level is then depopulated by collisional relaxation to the ground state. In Figure 1.1 is also illustrated the energy level diagram of N₂. The use of this gas in the excitation of the carbon dioxide laser is for an efficient means to excite the upper laser level. This is clearly seen from Figure 1.1 as the energy of the excited vibrational state of nitrogen is nearly the same energy of the upper carbon dioxide laser level. Energy is then transferred between the two species by collisions.

1.2.1 RF Excitation

Radio frequency energy excitation of CO₂ lasers is becoming more prevalent for high power industrial lasers of both fast axial flow^{4,5}, and sealed off diffusion cooled systems^{6,7}. Although more complicated and costly, compared to DC excitation, the advantages of RF excitation are numerous. Some of the more important features are listed in

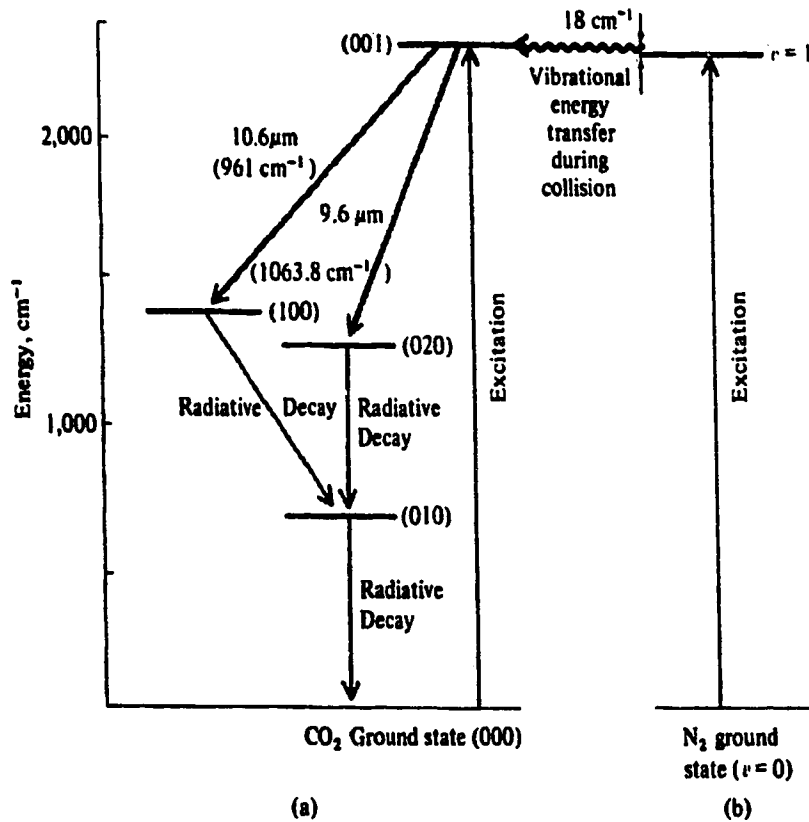


Figure 1.1 Energy Level Diagram of a CO₂ Laser³.

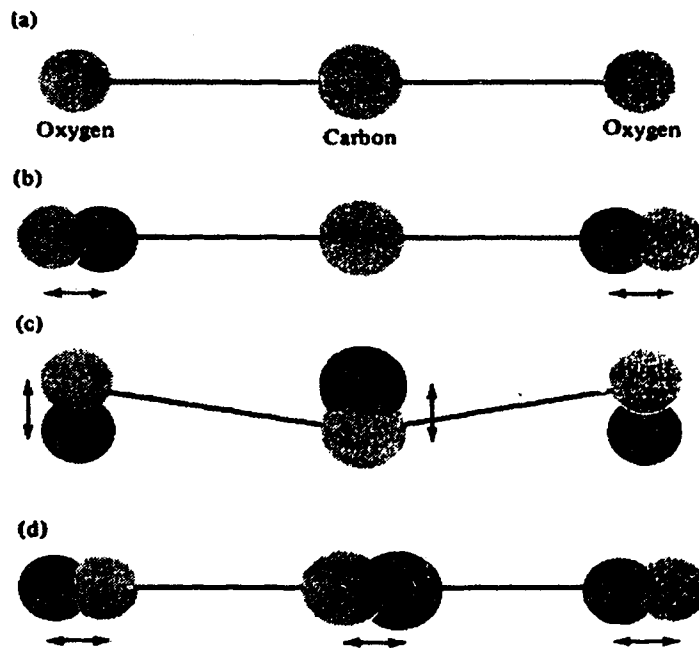


Figure 1.2 Vibrational Modes in a CO₂ Molecule (a) unexcited (b) symmetric stretch (c) bending (d) asymmetric stretch³.

Table 1.1. These advantages, in many cases, outweigh the inherent problems encountered with RF systems, namely RFI shielding and impedance matching.

Table 1.1 Advantages with RF excitation.

<p>The positive dynamic impedance of the RF discharge eliminates the need for ballast resistors, improving the electrical efficiency.</p> <p>The absence of a cathode fall region improves stability against glow-to-arc transitions at high gas pressure.</p> <p>Low striking voltage and low sustaining voltage of an RF discharge.</p> <p>Capability of electrode-less discharge, increases the life of sealed off lasers.</p> <p>Permits a uniform discharge sustained between large area parallel electrodes.</p> <p>Versatility in RF supply enables beam shape profiling from modulation, and/or pulse shaping the RF exciting voltage.</p>
--

When laser gas is excited in an RF discharge, the most prominent feature observed is formation of discharge sheaths. Figure 1.3 depicts optical luminosity of these sheaths as well as the luminosity of the positive column, or plasma region. These RF sheaths are created by positive ions whose positions remain stationary, due to the high oscillation frequency of the RF energy. Figure 1.4 illustrates these sheath regions, with electron and ion motion displayed as a function of time. Since the E/N , or electric field to particle number density, ratio in the sheath region is not appropriate for efficient CO_2 vibrational pumping, a lower frequency bound exists for effective RF laser excitation. In practice, this somewhat arbitrary frequency limit is defined as that for which the ion sheaths reduce the positive column region to half the electrode separation.

A more physical interpretation of the upper and lower frequency bounds for RF excitation arises from conditions affecting onset of discharge instabilities. The two common types of discharge instabilities are alpha to gamma transitions, and thermal instabil-

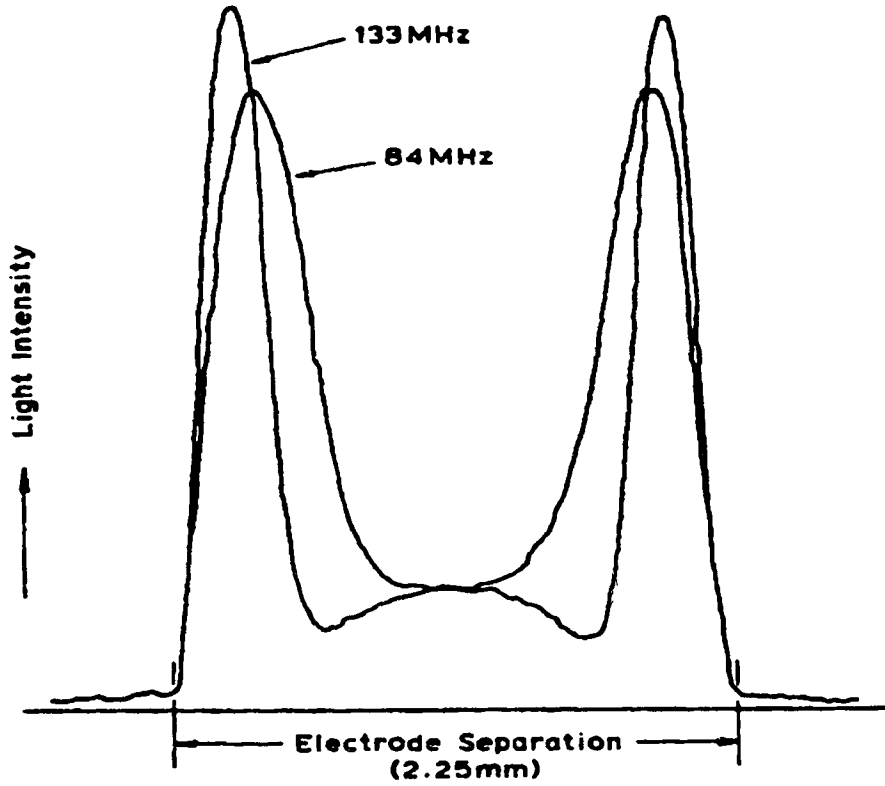


Figure 1.3 Optical Luminosity of an RF Excited Discharge Between the Electrodes⁸.

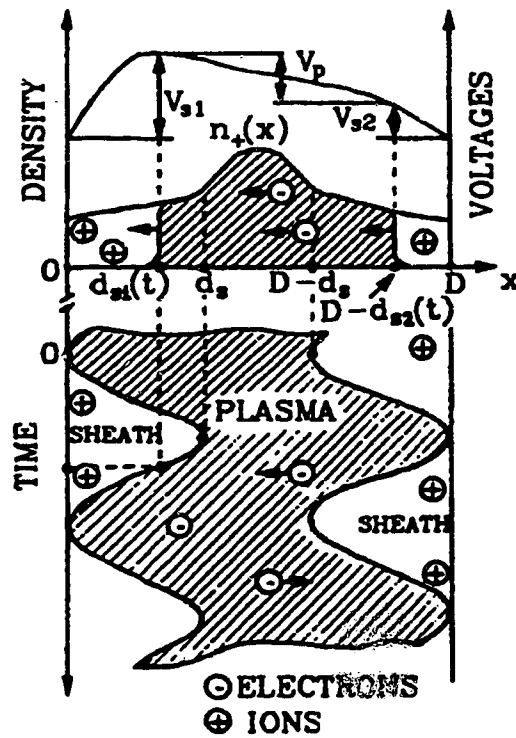


Figure 1.4 Space-Time Structure of an RF Discharge⁹.

ity. An alpha discharge is characterized by sustained volumetric ionization, which depends upon the first Townsend ionization coefficient α . The near-electrode ionization processes characteristic of the gamma mode of an RF discharge depend upon the third Townsend ionization coefficient γ . A normal α discharge features a stable positive column region exhibiting positive impedance behavior and is capable of high efficiency CO_2 vibrational excitation. Sheath regions are typically of low loss under these conditions. As the RF drive frequency is lowered, the sheath voltage increases. At a specific threshold level there is sufficient energy for positive ions to generate secondary emission from the metal electrode surfaces. If the excitation frequency becomes too low, then these secondary electrons can contribute to the plasma column region, thereby creating a γ discharge. Conditions appropriate for the existence of thermal instabilities are created when the heating mechanisms within the discharge become higher than the rate of gas cooling to the cold electrode surfaces.

A thermal growth analysis is unable to explain the stability of the α discharge⁹. Indeed, research has revealed that α discharge stability is a direct result of plasma sheath phenomena. Figure 1.5 illustrates that the positive column region of an RF discharge exhibits a constant voltage, regardless of current flow magnitude. Sheaths, on the other hand, have a positive voltage-current characteristic. Consequently, these sheaths act like ballast elements placed in series with a load having a non-positive voltage-current behavior. The fact that these sheath voltages are much greater than that of the plasma region insures overall stability. As the frequency of the RF discharge is increased, voltage across the increased sheath capacitance is reduced. As the sheath voltage is reduced to a level comparable to the plasma voltage, the stabilizing feature of the sheath regions has a

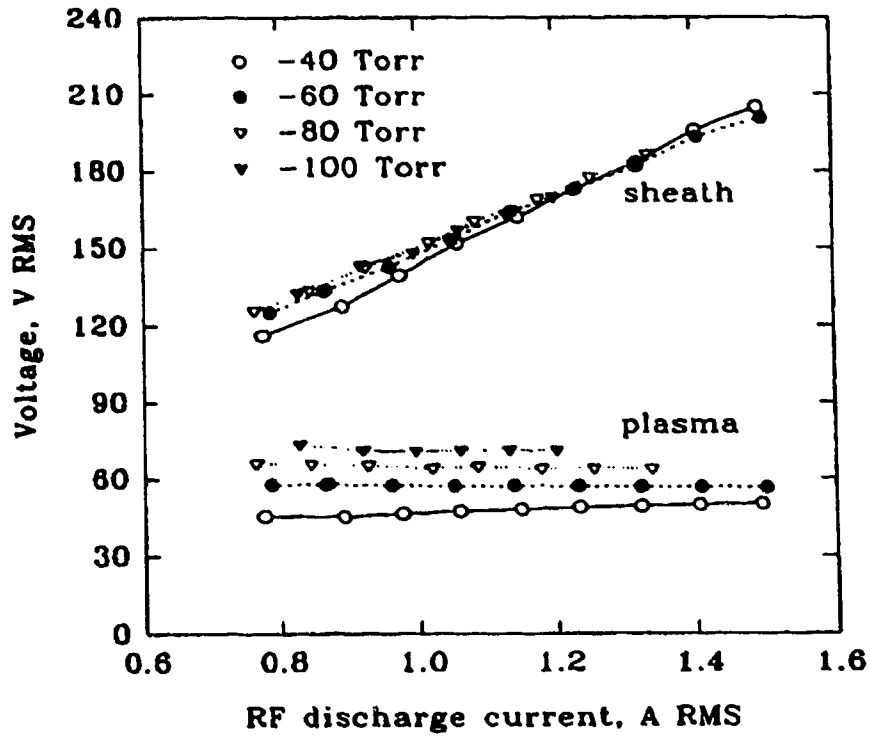


Figure 1.5 Plasma and Sheath Voltage-Current Characteristics³⁶.

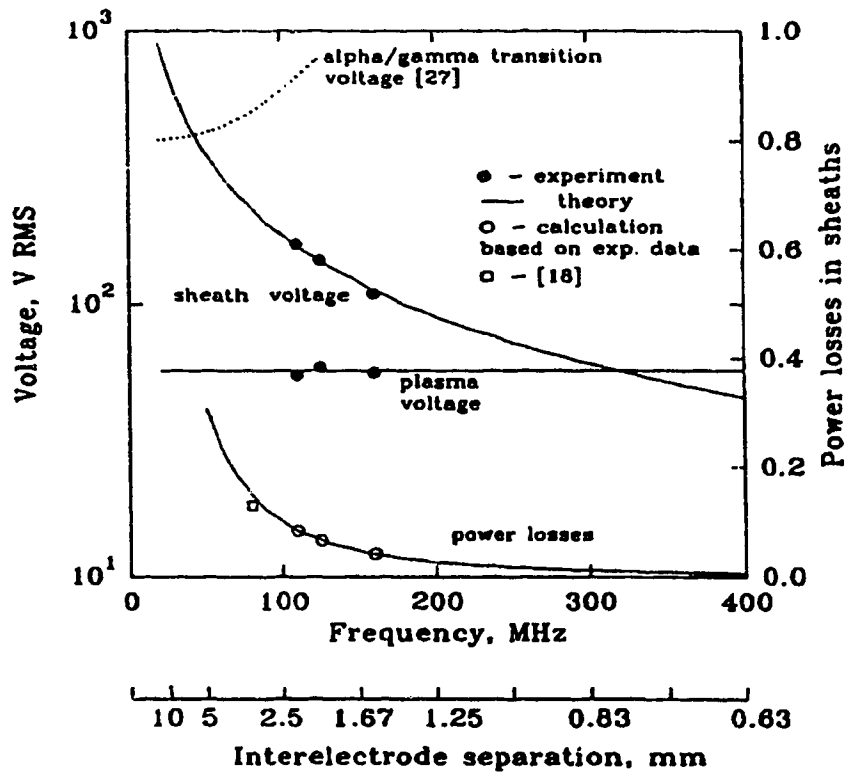


Figure 1.6 Frequency Dependencies on Sheath and Plasma Voltages³⁶.

diminishing effect. As such, the upper frequency limit of an RF discharge, shown in Figure 1.6, occurs at frequencies above 300 MHz.

Optimized electrode separation for a given frequency of operation is also shown in Figure 1.6. For typical electrode separations of 2 to 3 mm, sheath voltages are well below the α/γ transition region, yet well above the plasma voltage. Consequently, discharge instabilities are not of major concern with RF excitation of slab laser systems.

1.3 Waveguide Lasers.

Radio frequency excitation is ideal for extended-length narrow-gap gas devices typical of waveguide lasers. Initial versions of these RF excited waveguide lasers used bore sizes between 1 to 3 mm. Optical output is a single EH_{11} mode, determined primarily by the quality and dimensions of the guiding channel. With these lasers, the output power scales directly with device length. Specific output power is generally limited to values near 0.8 W/cm for static gas fills¹⁰. Systems featuring gas flow yield still higher powers, with powers well into the kilowatts range having been reported¹¹.

A primary advantage of waveguide lasers is their small size. Low RF power requirements also make it possible to integrate a transistor power supply into the laser head. Development of turnkey laser systems featuring diffusion cooling, and sealed off operation, is then possible. The disadvantage of these devices is that they are limited to output powers near 100 watts. Linear¹², and hexagonal¹³ waveguide arrays embodying many laser channels were investigated as a means to overcome these limitations. Although

increases in power were achievable, the added beam handling complexity of these systems has thus far precluded their use for industrial purposes.

1.3.1 Hybrid Waveguide Lasers

Hybrid waveguide lasers were developed to overcome power limitations of conventional waveguide devices. These lasers still maintained transverse waveguide dimensions, but the cross-sectional width has been broadened into a rectangular cross-sectional shape. Such a shape is referred to as a slab, because its electrodes are in effect large area plates separated by a small gap. Figure 1.7 illustrates such a device. A hybrid resonator is employed¹⁴ for optical energy extraction. This optical system maintains a flat curvature in the transverse direction to sustain a waveguide mode, while an unstable configuration is utilized in the longitudinal dimension. As such, a beam having a rectangular shape is created. Beam profile is defined by the waveguide dimension in height, and by the unstable resonator's output coupling and electrode shape in width. Consequently, a waveguide with a cross-sectional dimension of $100 \times 2 \text{ mm}^2$, with an output coupling of 25%, yields a beam of cross-sectional dimensions $25 \times 2 \text{ mm}^2$. If a confocal unstable resonator is used, then a beam with low divergence in this unstable dimension is generated. However, divergence in the waveguide or transverse dimension is a function of the transverse electrode separation. These factors give rise to a hybrid beam having different divergences in its transverse and longitudinal directions. A typical slab waveguide mode divergence is shown in Figure 1.8, where the beam waist, given by $\omega(z)$, is the beam radius as it propagates away from the laser. Near and far field mode profiles are illustrated in Figure 1.9. Because of this characteristic beam profile, correction for

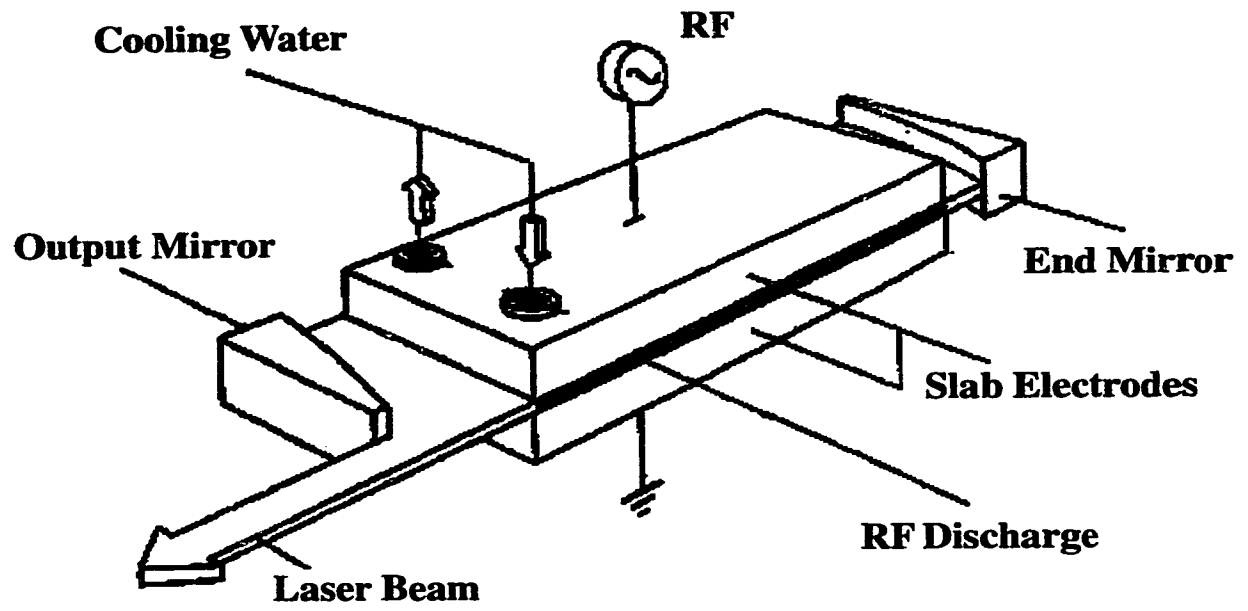


Figure 1.7 Slab Waveguide Laser⁶.

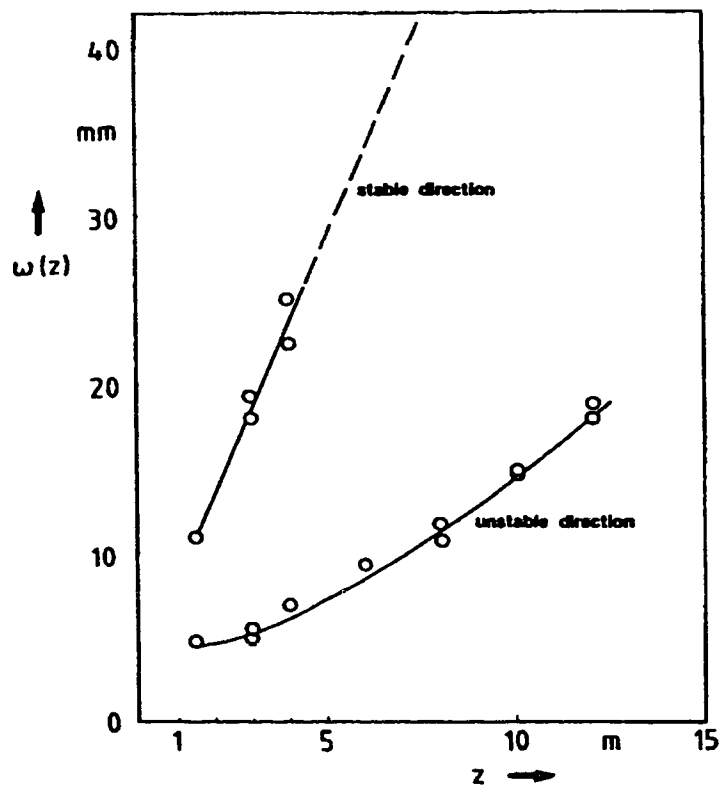


Figure 1.8 Slab Waveguide Mode Divergences⁶.

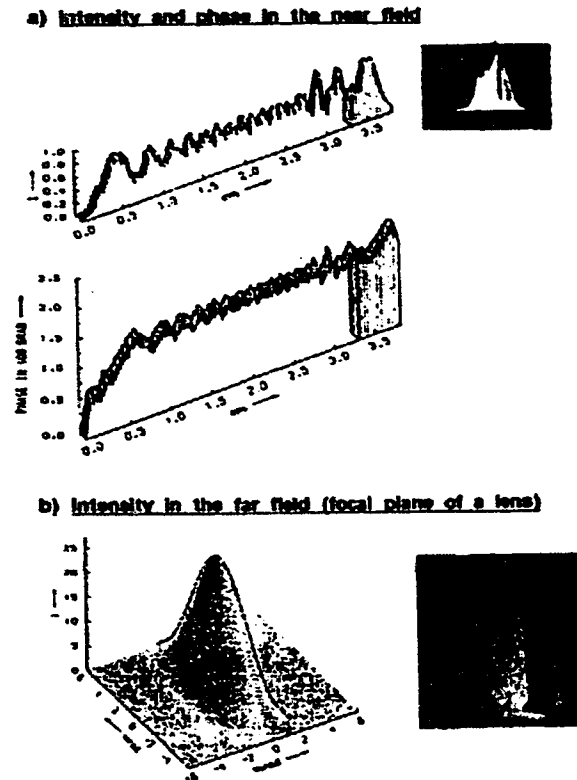


Figure 1.9 Near and Far Field Beam Profiles of a Slab Mode⁶.

asymmetry then becomes necessary for many laser applications. With appropriate asymmetry compensation, CO₂ lasers with good optical quality and operating in the 1 kW category have been achieved⁶.

Advancement of laser output power levels into the multi-kilowatt range has been difficult for single slab devices. Power scaling laws developed for slab waveguide lasers^{15,16} have shown that laser power scales directly with electrode area. Figure 1.10 shows the extractable output power in terms of electrode area for a specific electrode separation. At first it may seem plausible that if the electrode area were made large enough, then an arbitrarily powerful laser could be constructed from a single slab. To

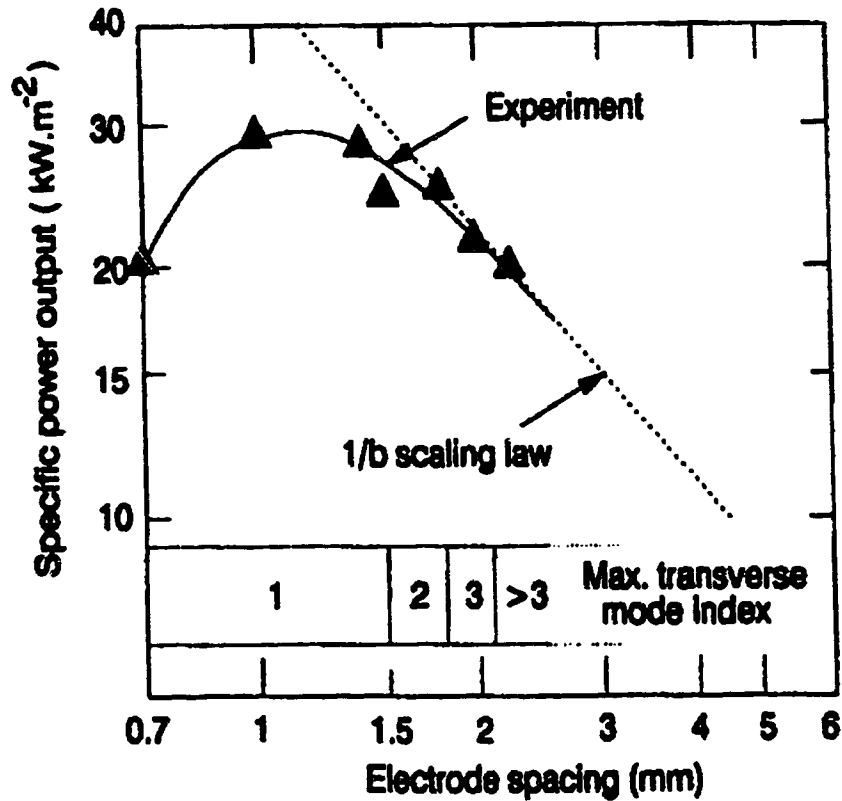


Figure 1.10 Scaling Law for Slab Lasers¹⁵.

illustrate this point, a 5 kW slab laser should in principle be achieved with an electrode 10 x 250 cm² in area and separated by a 2 mm gap. For a large slab, significant output coupling approaching 50% is necessary. This will result in an output beam with cross-sectional dimensions of 50 x 2 mm². Such a beam profile must then be heavily corrected for astigmatism. In addition, a beam with an average power density of 5 kW/cm² will heavily overstress the anti-reflecting coatings on ZnSe windows and thereby induce premature failure. Because of these technological problems, multi-kilowatt single slab lasers, though technically feasible, are not commercially viable.

Further difficulties encountered with single slab devices occur in establishing stable power deposition. As the area of the electrodes increases, so does the chance of a locally non-uniform region undergoing an alpha to gamma discharge transition. When this happens, the total input power is deposited within this small region, resulting in electrode failure. To reduce this occurrence it is preferable to use multiple electrodes, of smaller area, to distribute the input power over several independent discharge regions.

1.3.2 Multi-Channel Systems.

In extending slab laser concepts into multi-channel systems two scaling approaches are of interest, these being linear and radial arrays. In a linear array, the slabs are stacked one upon the other in a vertical manner. A device successfully employing this method is the triple open slab laser developed by Lapucci et al.¹⁷. This device, shown in Figure 1.11, uses a fork shaped electrode for the RF drive, and another, inter-digital, fork shaped electrode as ground. Array water cooling is introduced along the outer edge. A significant distance exists between the active discharge region of the electrode and the cooled surfaces. Because of this fact, this geometry is restricted in slab width, since cooling efficiency of the device would decrease rapidly if the slab width were much more than a few centimeters. Success in phase locking¹⁸, and the potential extension of the array to 11 channels¹⁹, may yet yield a useful device of up to 500 watts in power. A disadvantage of the device is again beam astigmatism. Device operation in a phase locked mode is illustrated in Figure 1.12. As can be seen from this figure, each beam has the same profile, but is offset by a fixed distance. The consequence of stacking several such beams in a linear array is that the resulting composite beam has the same beam divergence asymmetry char-

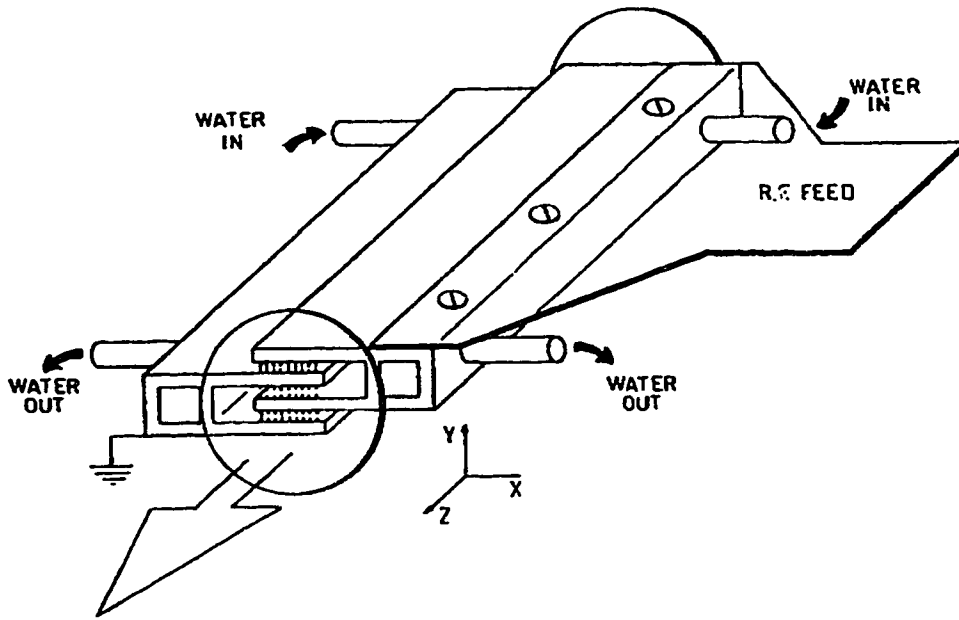


Figure 1.11 Triple Slab Laser¹⁷.

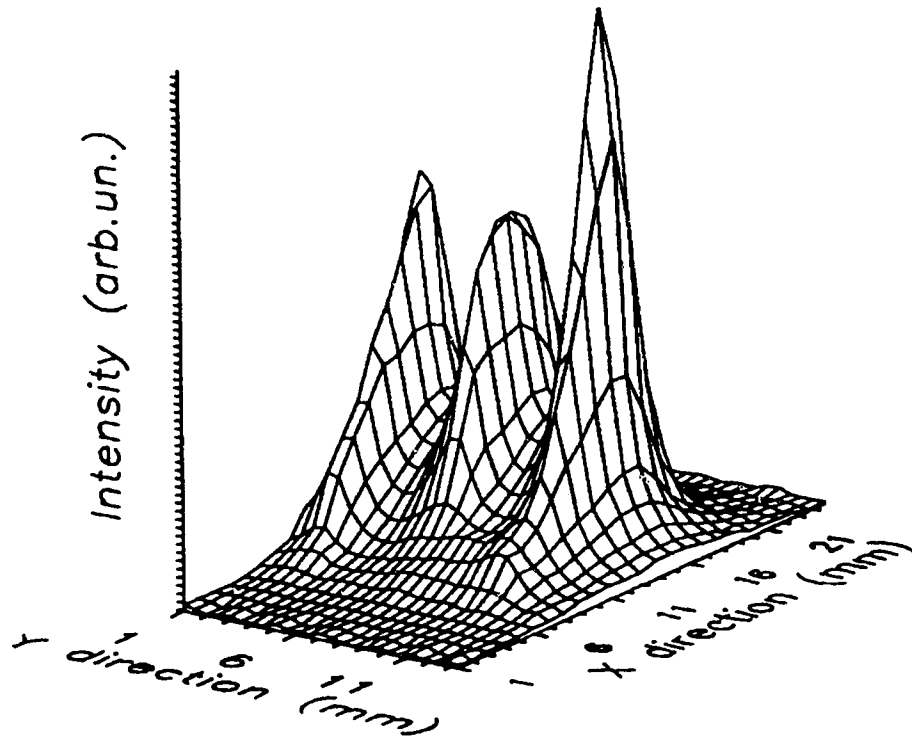


Figure 1.12 Phase Locked Mode from a Triple Slab Laser¹⁸.

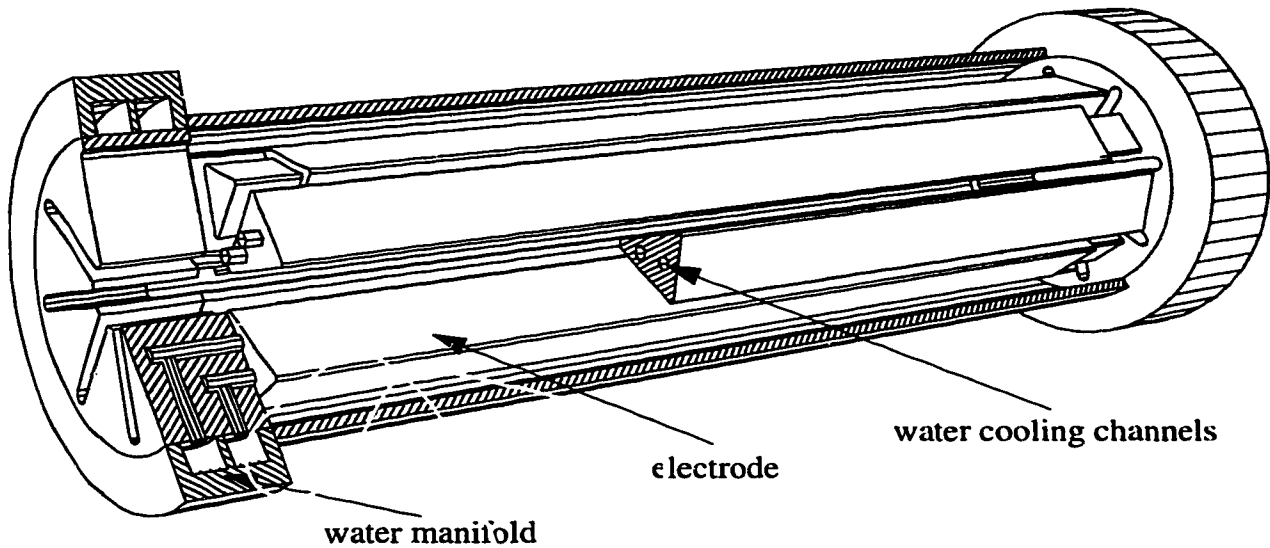


Figure 1.13 Eight Channel Zodiac Laser System.

acteristic of a single slab device. Although unique, this laser offers no apparent advantage over a single slab laser. In fact the device will have difficulties approaching the power levels of current single slab lasers.

The other configuration mentioned employs radial arrays. Yelden et al.²⁰ first published details of a radial array slab geometry. This device, shown in Figure 1.13, was an 8 channel slab laser with dimensions of $5 \times 35 \times 500 \text{ mm}^3$. The unit was driven from a single RF generator, through a PI matching network. Every second electrode was grounded, and the resulting unbalanced circuit consisted of alternating RF driven and grounded electrode pairs. Unlike the triple slab device of Lapucci et al., these electrodes were cooled by two water channels bored directly into the electrode structure. This aspect provides a more efficient and uniform method of heat extraction. As such, scaling of this device in width is not an issue. Furthermore, in this structure, the outer edge of the electrode is exposed, thereby enabling inductors to be mounted along the electrode length, to reduce any stand-

ing waves that may result. Because of this feature, scaling of the electrode in length is also feasible.

The radial array is sufficiently compact that all discharge channels may share a common optical resonator. This enables full flexibility in selecting resonator geometries and output coupling features. Two common optical resonators are the toric²¹, and unstable²² resonator. Both of these optical cavities are unstable in operation, in that a ray will not retrace a path before being coupled out of the structure. The major difference between these optical extraction systems lies in the manner optical energy walks out of the resonator. In a toric resonator, beams walk toward the center, while in an unstable resonator the beams walk toward the outer edge of the electrode. The use of an unstable resonator permits creation of a common core oscillator region. Consequently, a self-injection phase locked output will be produced as the beamlets propagate outward through the multiple channels.

Once these beamlets have exited the laser structure, the question remains whether any further optics are necessary to condition the beam for practical applications. Using the simplest resonator, the toric, these beams were extracted through a common AR coated ZnSe window²³. The study by Yelden et al. showed that when these individual beamlets were radially stacked, a composite beam of circular symmetry, uniform divergence, and no net polarization was produced. Experiments with this composite output radiation revealed that cutting performance was as good as with many commercial systems currently available. It is particularly noteworthy that this level of beam quality was achiev-

able without any beam conditioning optics, or phase locking. With a phase locked system superior cutting performance is expected due to the greatly reduced focal spot size.

The performance of the Zodiac laser system was compromised by the fact that the discharge channels were connected to each other in a parallel geometry. Because of this condition, the laser was limited to output powers of slightly greater than 200 watts, at an input drive of 3 kW. From the slab scaling law data mentioned previously, a laser with a 5 mm electrode gap should deliver output powers scaling as 0.9 W/cm^2 of electrode area. With the 8 channel device, total electrode area was $1,400 \text{ cm}^2$, and consequently it should have yielded an output power over 1,200 watts. The reduced power rating of this device was directly related to the RF feed employed. This resulted in discharge channels collapsing from 8 active regions to only one channel when operating pressure was increased beyond 20 torr. The optimum pressure for a device with a 5 mm gap is 30 torr. In addition, because of the unbalanced RF feed incorporated into the initial design, corona to the vacuum vessel became a problem if the input RF drive exceeded 3 kW. These two constructional factors limited the potential of this first Zodiac device, and prompted re-design and development of a vastly improved version, which constitutes the primary topic of this thesis.

Chapter 2

2.0 Resonant Cavities

With the potential of the initial zodiac laser not being realized due to drive considerations, this problem must be addressed if such a system is to become commercially viable. By using transmission line resonant cavities between the RF generator and laser head, an intermediate device is utilized to store and extract this energy. Due to the nature of cavity resonators to store energy with low resistive losses, such a device is ideal for high efficiency isolation of the RF energy, and redistribution into several independent loads.

This chapter will describe the use of a resonant cavity as a high power splitter and impedance transformer, which in turn makes multi-channel excitation practical. Previous work with slab lasers has been limited primarily to single channel excitation, due to difficulties in RF energy deposition into multiple electrodes. Although extensive research world wide has been done on single slabs,^{29, 17} an effective solution to high power independent drive to multi-channels has thus far eluded the research community.

Since transmission line cavity resonators are basic devices, only a brief description of the structure will be given. This chapter will therefore emphasize design and operational characteristics of coaxial cavity resonators, and their application as high powersplitters and impedance transformers.

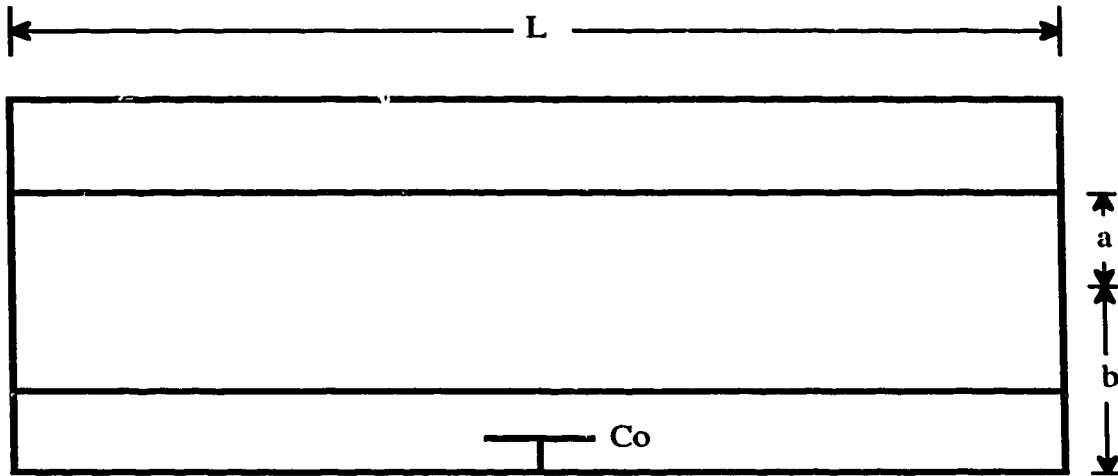


Figure 2.1 Half Wavelength Resonator.

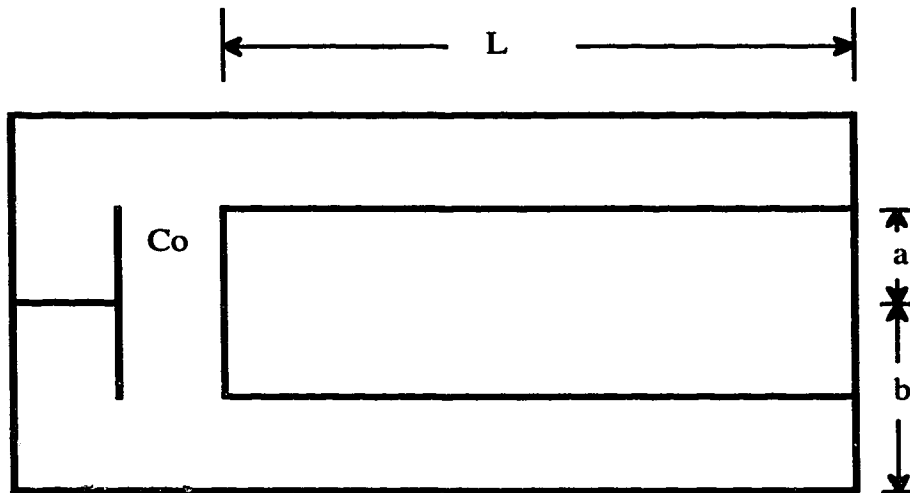


Figure 2.2 Quarter Wavelength Resonator.

2.1 Half Wavelength Resonators

The design of a half wavelength cavity, shown in Figure 2.1, proceeds as follows. A half wavelength section of transmission line is short circuited at both ends. This feature creates a resonant cavity in which tuning may be accomplished by capacitive loading at the midplane. The configuration can also be thought of as two quarter wavelength cavities stacked in series and sharing a common open circuited plane.

2.2 Quarter Wavelength Resonators

The design of a quarter wavelength resonator is similar to that of a half wavelength coaxial resonator, except that the resonator length is reduced by a factor of two. Because of this, one end is open circuited while the other is shorted. Figure 2.2 is a schematic of this type of resonator. It is often desirable to further shorten the length of such a cavity. This is easily accomplished by capacitively loading the open circuited end. The effect of adding capacitive reactance, when resonated by the inductive section of the cavity, is a resonance at lower frequency. In this design the length of the cavity, L , is given by the following equation.

$$\frac{1}{\omega C_o} = Z_o \tan(\beta L) \quad (2.1)$$

Rearranging terms, the effective length of the cavity becomes:

$$L = \frac{\tan^{-1}(1/\omega C_o Z_o)}{\beta} \quad \text{where,} \quad (2.2)$$

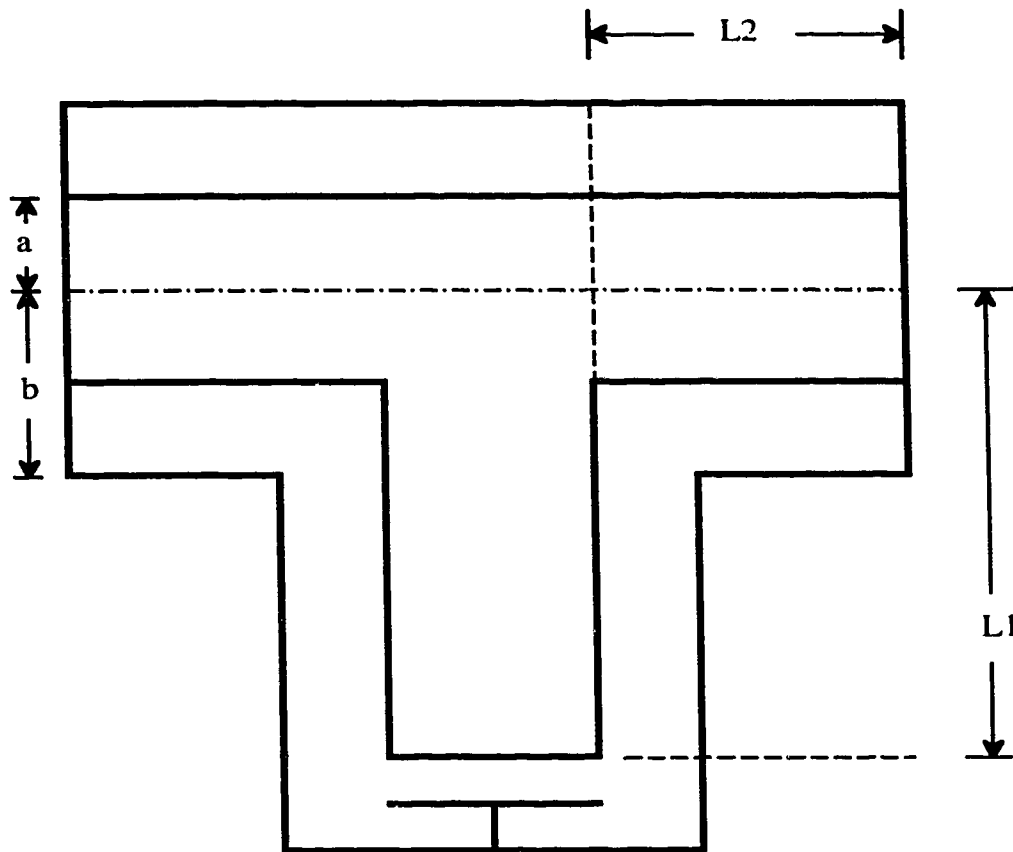


Figure 2.3 T Resonator.

$$Z_o = \frac{1}{2\pi} \sqrt{\frac{\mu}{\epsilon}} \ln\left(\frac{b}{a}\right) \quad \text{and,} \quad (2.3)$$

$$\beta = \frac{2\pi}{\lambda} \quad (2.4)$$

The equation 2.2 is derived for the case of a lossless transmission line, where the impedance $Z_{in} = jZ_o \tan(\beta L)$, is inductive for lengths less than a quarter wavelength. From

the above equations it is clear that the added lumped capacitive reactance $1/\omega C_0$ makes the circuit resonant at a lower frequency as compared to the case of no capacitive loading.

2.3 T Resonators

Design of a coaxial T cavity is more complicated, since the effective inductive length L has to be determined. Figure 2.3 is a schematic of such a system. The upper arm of the T is essentially two transmission lines connected in parallel. This has the effect of making each arm's electrical length half of its physical dimension. The effective length of this cavity as described in equation 2.2 is $L1 + L2/2$. Due to its shape, it is more difficult to change frequency by changing cavity length. This is due to the fact that two moveable short circuit planes are needed. Changing the capacitive loading has the same effect, and is the preferred method of tuning such a cavity.

2.4 Determining the Cavity Q

The Q of a coaxial cavity is given by ²⁴:

$$Q = \frac{2\pi f \sqrt{\epsilon}}{2c(\alpha_c + \alpha_d)} \quad (2.5)$$

where f is the frequency in Hertz, ϵ is the dielectric constant, c is the speed of light, α_c and α_d are the conductor and dielectric losses in Nepers per meter given respectively by:

$$\alpha_c = \frac{R_s \sqrt{\epsilon}}{2\eta \ln(b/a)} \left(\frac{1}{a} + \frac{1}{b} \right) \quad (2.6)$$

$$\alpha_d = \frac{\pi f \sqrt{\epsilon}}{c} \tan \delta \quad (2.7)$$

Here η is the impedance of free space, b is the outside radius, a the inner radius, and $\tan \delta$ is the loss tangent of the dielectric material. R_s is the surface resistance of the material and is given by ²⁴:

$$R_s = \sqrt{\frac{\pi \mu_0 f}{\sigma}} \quad (2.8)$$

where μ_0 is the permeability of free space and σ is the conductivity in S/m.

Measurement of cavity Q is possible by examination of either transmission or reflection characteristics. Transmission loss or insertion loss (IL) is a measure of power loss, with respect to the input signal. When the frequency is swept off resonance the transmitted power decreases. The upper and lower frequencies at which the signal has decreased by 3 dB are specified as the half power points, which define the cavity bandwidth. This bandwidth, given by Δf , is used to determine the loaded Q according to the following equation:

$$Q_L = \frac{f_0}{\Delta f} \quad (2.9)$$

Here f_0 is the center, or resonance frequency. Measuring the Q using the reflection, or return loss (RL), signal is more complicated. For a matched case where all the energy enters the cavity the bandwidth as given by Δf is determined by measuring the frequency between the points -3 dB down from the 0 dB reference level. If however, not all of the

energy enters the cavity, the bandwidth is determined by measuring the frequency bandwidth between the half power points represented by the following equation ²⁵:

$$\Delta f_{1/2 \text{ Power}} = 10 \log_{10} \left(\frac{2}{1 + 10^{-RL(@f_o)/10}} \right) \text{ dB} \quad (2.10)$$

where the RL is measured in units of dB.

For a return loss of 3 dB, the bandwidth is then given by the frequency separation between the -1.25 dB points of the network analyzer.

Once the loaded Q is determined experimentally, the unloaded Q can be inferred from the relationship between the loaded and unloaded Q. This relationship is given by:

$$\frac{1}{Q_L} = \frac{1}{Q_{\text{ext1}}} + \frac{1}{Q_{\text{ext2}}} + \dots + \frac{1}{Q_u} \quad (2.11)$$

where Q_{ext1} , and Q_{ext2} are circuit Q's of the external loads connected to the cavity.

It is thus possible to calculate the unloaded Q of a cavity from a knowledge of the external coupling into the cavity and the loaded Q. For example, consider a one port network with a return loss of 30 dB. First Δf is obtained from equation 2.10 via a measurement of the -3 dB power points. With this information, the loaded Q is calculated with equation 2.9. Using equation 2.11 and understanding that a RL of 30 dB signifies a matched condition, it is clear that the external Q is equal to the unloaded Q, which indeed is the requirement of a matched condition. As such, the unloaded Q is equal to twice the

loaded Q. The value of Q_u obtained in this manner is used subsequently in determining cavity efficiency.

2.5 Coupling Loading

Coupling loading refers to cavity loading by external means. Three cases define the possible loading of a resonant cavity, these are: undercoupled, critically coupled, or overcoupled. An undercoupled situation arises when the external load connected to the cavity has an external Q higher than that of the cavity itself. The level of coupling to an external circuit is easily determined from the standing wave ratio on the line. A reflection coefficient (Γ) can be determined from the standing wave ratio (SWR) of a line, by:

$$\text{SWR} = \frac{1 + |\Gamma|}{1 - |\Gamma|} \quad (2.12)$$

and the level of coupling is related to the reflection coefficient, Γ ²⁵:

$$K = \frac{1 \pm \Gamma}{1 \mp \Gamma} \quad (2.13)$$

where K is the coupling constant.

Two values are possible, one for undercoupled, and the other for an overcoupled case. This technique for measuring coupling applies only to a one port network. If such a network exists, then the actual level of coupling can be determined by increasing the coupling in the cavity and noting the change in the reflection coefficient. A decreasing reflection coefficient, with increasing coupling, signifies an undercoupled case. However if the reflection coefficient increases, then an overcoupled situation exists.

Since the level of coupling is directly related to cavity Q , the coupling constant can also be defined as:

$$K = \frac{Q_u}{Q_{ext}} \quad (2.14)$$

A matched condition implies that $K = 1$. Since the level of coupling is related to the unloaded Q , the relationship between the loaded Q and the unloaded Q with respect to coupling may be expressed as:

$$Q_u = (1 + K)Q_L \quad (2.15)$$

Determining the level of coupling for each port becomes more difficult in the case of multiple ports all connected to the same cavity. Measurement is simplified when all ports are matched and coupled by the same amount, such that there are no reflections along the external line. Fortunately, this is the most common or desirable mode of operation in a cavity used as a power splitter, or combiner. When this situation occurs all the external Q 's are the same and equation 2.11 becomes:

$$\frac{1}{Q_L} = \frac{N}{Q_{ext}} + \frac{1}{Q_u} \quad (2.16)$$

where N is the number of external ports coupled into the cavity. Determination of the coupling level at each port requires one further relationship, that being the efficiency of power transfer. If both input and output coupling are equal, the cavity's insertion loss may be expressed in terms of cavity Q 's as²⁷:

$$IL(\text{dB}) = 20 \log_{10} \left(\frac{1}{1 - Q_L/Q_u} \right) \quad (2.17)$$

Equation 2.17 permits a calculation of the unloaded Q from a knowledge of the measured insertion loss and loaded cavity Q . Substituting these values into equation 2.16 enables determination of the external Q and hence the coupling factor K .

An equivalent way of expressing equation 2.17 in terms of efficiency is:

$$\eta = \left(1 - \frac{Q_L}{Q_u} \right)^2 \quad (2.18)$$

Examination of this equation reveals that it is desirable to have a loaded Q very much lower than the unloaded Q of the cavity, if efficient power transfer is to be achieved.

Once the cavity Q 's relation to power transfer is known, the remaining question is how to couple energy into and out of the coaxial structure. Historically two methods have been employed for this purpose; capacitive or electric coupling, and inductive or magnetic coupling. Capacitive coupling is useful in high impedance situations and is achieved by using a probe inserted into the high electric field region of the cavity. In the case of a quarter wavelength cavity this is at the open circuited region of the structure. The disadvantage of electric coupling is that a change in load requires retuning the coupling probe's impedance. Inductive coupling uses loops to couple energy out of the high magnetic field regions of the cavity. Magnetic coupling has two important advantages. The first stems from the fact that a wide range of load impedances can be matched into the loop, since it acts like a voltage source. In addition, coupling is easily adjusted by rotating the loop to

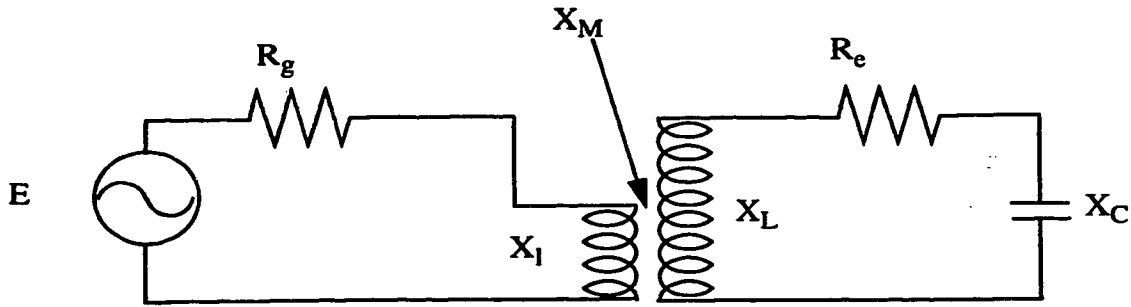


Figure 2.4 Equivalent Circuit of a Coaxial Cavity Loaded by a Single Loop.

give a greater or lesser cross sectional area that is exposed to the circulating magnetic field. Another advantage is that the loop presents minimal perturbation to the cavity. Consequently, only a slight shift in resonant frequency is observed as the impedance of the loop is changed. For these reasons, loops are ideal for coupling energy into and out of cavities.

When extracting energy out of a resonant cavity by using loops, it is essential to ascertain what loop size should be used to give the desired loading. Such a determination may be made with the aid of an equivalent circuit model of a resonant structure driven by a loop. Consider the schematic illustrated in Figure 2.4. The inductive reactance of the resonant cavity, X_L is given by ²⁸ $Z_0 n \pi / 4$, where Z_0 is the characteristic impedance of the cavity and n is the length of the cavity in units of quarter wavelengths. Since the loaded Q is given by X_L / R_e , where R_e is the equivalent resistance in series with the short-circuited resistance of the cavity, the loaded Q can be written as:

$$Q_L = \frac{\pi n Z_0}{4 R_e} \quad (2.19)$$

If the loaded Q is not much lower than the unloaded Q , equation 2.19 then needs to be expanded to account for the effects of this in the following way:

$$Q_L = \frac{\pi n Z_0 Q_u / 4 R_e}{\pi n Z_0 / 4 R_e + Q_u} \quad (2.20)$$

An expression linking loop size with the equivalent resistance of the cavity is thus required. This expression is related to X_M , the mutual reactance between the resonant circuit and the loop. For a coaxial resonant system this reactance is given by ²⁸:

$$X_M = \frac{A \mu_o f \cos \theta}{r} \quad (2.21)$$

where A is the cross sectional area of the loop, f the resonant frequency, r the radial distance from the cavity of the effective center of the loop, and θ is the angular distance the effective center of the loop is from the short circuited plane. If X_M , and X_L are small with respect to X_L , then the equivalent resistance, R_e , will be equal to $(X_M)^2/R_g$. Now equation 2.19 can be written as:

$$Q_L = \left(\frac{\pi n Z_0}{4} \right) \left(\frac{r^2 R_g}{A^2 \mu_o^2 f^2 \cos^2 \theta} \right) \quad (2.22)$$

If more than one loop is used in the circuit, and each loop has the same level of coupling, then the effective series resistance will add and be equal to N times R_e . Thus for a cavity with more than one loop the expression for the loaded Q becomes:

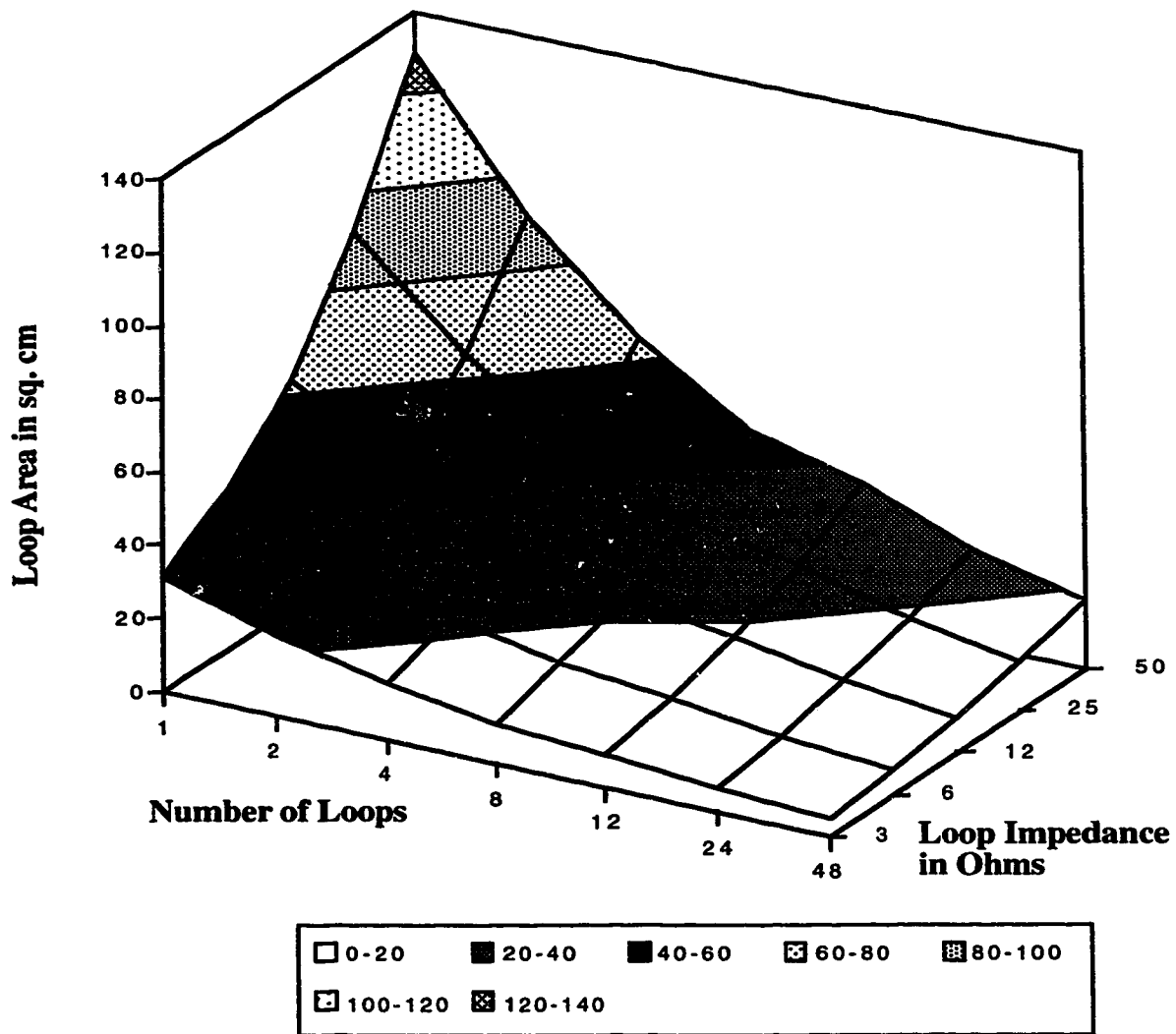


Figure 2.5 Coupling Loop Area(cm^2) vs. Number of Loops and Loop Impedance.

$$Q_L = \left(\frac{\pi n Z_o}{4N} \right) \left(\frac{r^2 R_g}{A^2 \mu_o^2 f^2 \cos^2 \theta} \right) \quad (2.23)$$

Where N is the number of loops coupled into the cavity.

Equation 2.23 can be used to determine how big a loop should be to achieve a desired loaded Q. In Table 2.1 the size, number of loops, and their effect upon the loaded Q is shown. Figure 2.5 is a plot of this table. Table 2.1 specifies the size of the loops that give a loaded Q of 10 at a frequency of 100 MHz in a coaxial structure 434 mm in diameter and having a characteristic impedance of 18 ohms. From this table it is evident that as the impedance of the load decreases the loop area necessary for the same cavity loading also decreases.

Table 2.1 Loop area(cm²) vs. load impedance and number of loops for Q_L of 10 @ 100 Mhz.

Number of Loops	Loop Area 3 Ohm Load	Loop Area 6 Ohm Load	Loop Area 12 Ohm Load	Loop Area 25 Ohm Load	Loop Area 50 Ohm Load
1	31.5	44.6	63.0	90.9	129
2	22.3	31.5	44.6	64.3	90.9
4	15.8	22.3	31.5	45.5	64.3
8	11.1	15.8	22.3	32.2	45.5
12	9.09	12.9	18.2	26.3	37.1
24	6.43	9.09	12.9	18.6	26.3
48	4.55	6.43	9.09	13.1	18.6

Table 2.2 Loop area vs. frequency for Q_L = 10.

Frequency in MHz	Loop Area in cm ²
40.68	312
50	254
60	212
70	182

Table 2.2 Loop area vs. frequency for $Q_L = 10$.

Frequency in MHz	Loop Area in cm^2
80	160
90	143
100	129

In Table 2.2 the effect of frequency on loop size is shown. In this case the loaded Q is 10, there is one loop driving a 50 ohm load, and the cavity again has a diameter of 434 mm and an impedance of 18 ohms. As expected, at lower frequencies wavelengths are larger and this in turn necessitates loops of larger cross sectional area to couple the same amount of power out of the structure.

Experimental verification of equation 2.23 was achieved by using a small coaxial cavity with inner and outer diameters of 4.12 cm, and 16.6 cm respectively. Two loops were used, one of 14.6 cm^2 and the other of 44.4 cm^2 , both terminated in a HP network analyzer of 50 ohms. In Table 2.3 the theoretical loop size is compared with actual measured loaded Q values for several different frequencies.

Table 2.3 Theoretical loop area using a loop of 14.6 cm^2 .

Frequency in MHz	Loaded Q (Measured)	Theoretical Loop Area (cm^2)
60	124	23.6
69.5	103	22.3
100	80.5	18.0
113	69.0	17.2
150	60.2	14.0
200	49.5	11.7

In Table 2.4 loop size is compared with loaded Q values, using a loop of 44.4 cm^2 in area.

Table 2.4 Theoretical loop area using a loop of 44.4 cm².

Frequency in MHz	Loaded Q (Measured)	Theoretical Loop Area (cm ²)
60	25.7	54.0
100	25.1	33.0
150	27	21.5

As can be seen from Tables 2.3 and 2.4 the agreement between actual and predicted results is not very good. This is partly due to the fact that the loop sizes are quite large, so that the approximation that X_L , and X_M are small as compared to X_L is no longer correct. Also the derivation of equation 2.23 assumed no capacitive coupling. Since the loops extended far into the cavity, and due to their rectangular shape, the assumption that there is no electric coupling is again invalid. However, equation 2.23 does provide an approximation to the size that loops should be, within a factor of 2, and as such is useful in design.

2.6 Material and Dielectric Loading

The choice of materials used for construction also affects the cavity Q. Material loading effects arise due to attenuation or loss of the electromagnetic wave as it propagates along the coaxial structure. Materials with a large conductivity clearly reduce resistive losses where currents are high. Dielectric losses arise from the fact that all insulators have some loss when exposed to electric fields. Ohmic losses dominate near the short circuit plane of the cavity where magnetic fields and surface currents are greatest. In the construction of co-axial cavities, it is usual to solder the inner and outer assemblies together. This places an interface of solder in the current path and hence a greater loss occurs here. This loss is greatly reduced for structures which are silver plated afterward. The electric

fields are maximized at the open circuited plane. Thus dielectric losses have the largest impact in this region, since electric energy is stored in the capacitive junction. Values for the unloaded Q were calculated by applying equation 2.5 to a cavity with an outer diameter of 16.6 cm, an inner diameter of 4.12 cm, operating at a frequency of 40.68 MHz. These values illustrating the material effects upon the resonant cavity Q are shown in Table 2.5. From the data it is evident that even a low loss dielectric like Teflon ($\tan\delta$ of 0.0004) filling the coaxial cavity produces a much greater attenuation than the metal structure alone. As such, loading or tuning capacitors always have a negative effect on the unloaded Q of a resonant system.

Table 2.5 Unloaded Q vs. material loading @ 40.68 MHz.

Cavity Material	Cavity Q no dielectric	Cavity Q with teflon
Silver	4580	1617
Copper	4445	1600
Aluminum	3601	1476
Brass	2952	1354
Solder	1542	954

2.7 Coupling Effects upon Power Transfer

As stated in section 2.5, maximum power transfer is achieved when the resonant cavity is heavily coupled. Another effect is that the loading or coupling of the input and output must be matched for the most efficient and greatest power transfer. A formula describing the ratio of transmitted power to input power for a two port cavity at resonance is ²⁵;

Power transmission through a 2 port cavity

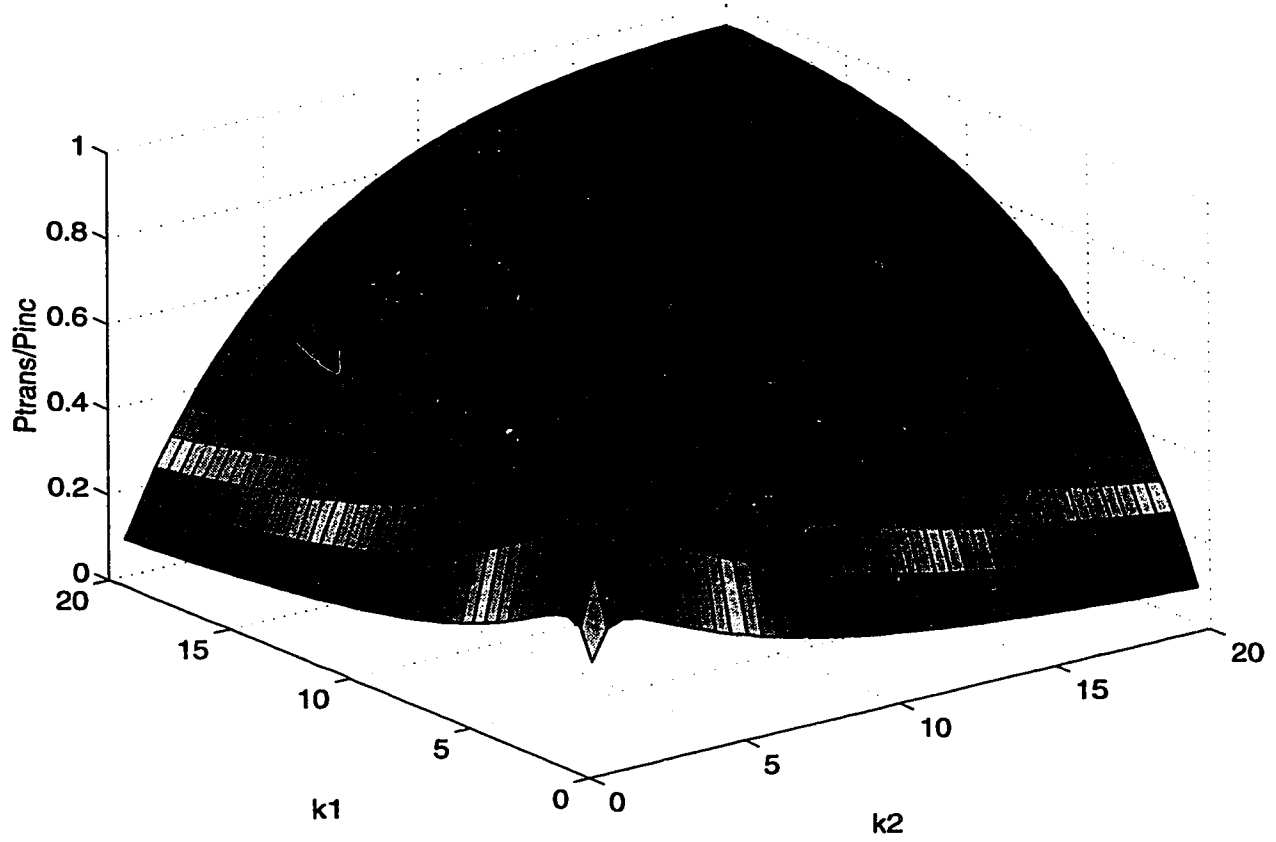


Figure 2.6 Power Transmission Through a 2 Port Cavity.

$$\frac{P_{\text{trans}}}{P_{\text{inc}}} = \frac{4K_1K_2}{(1 + K_1 + K_2)^2} \quad (2.24)$$

where K_1 , and K_2 , are coupling constants of the input and output sections of the resonator. From inspection, it is apparent that for the largest transfer of power, K_1 and K_2 should both be large. A plot of equation 2.24 with K_1 and K_2 as variables is given in Figure 2.6. Figure 2.6 further shows that input and output coupling factors should be equal for maximum power transfer. The question thus becomes how can this condition be modeled for multiple outputs? Since the loaded Q is a measure of the coupling factor, input and output loops should be designed such that each will give the same value for the loaded Q ; thereby providing a matched input and output condition. As an example, consider the case of a single input feeding 10 outputs and an unloaded Q of 1000. For an efficient resonator, high coupling is required so both the input and output coupling are designed with a coupling factor of $K = 20$. This implies that on each side the input and output will produce a loaded Q equal to $1/20$ of Q_u , or a value of 50 as given by equation 2.14. For the input side, the size of the loop needed to give this level of coupling can be determined by equation 2.23. For the situation of 10 identical loops coupling energy out of the cavity, how multiple loops affect the loaded Q of the resonator must be considered. Since each loop is effectively in parallel in the resonator from equation 2.16, it is apparent that if we place 10 loops, with each loop having an external Q near 500, the total loaded Q will be 50, thereby matching the input loading. This will give a system loaded Q of 25 and an overall energy transfer efficiency of 95%. Since each output loop has an external Q that is ten times that of the total loaded output, power isolation with other loops is inversely proportional to the number of loops.

In order to verify these numbers, tests were performed on a T shaped cavity with an unloaded Q of ≈ 2055 . This value was measured by using a network analyzer via injecting a low level signal into the structure and calculating the resultant unloaded Q. The cavity was loaded with four identical loops, each $15 \times 4 \text{ cm}^2$ in area and terminated into 50Ω loads. A loaded Q of 38.5 was subsequently determined from a bandwidth measurement on a network analyzer. Extracted output power is given in Table 2.6 was measured using Bird thurline wattmeters. Equation 2.18 predicts a theoretical efficiency of 96%. This is in excellent agreement with the experimentally measured values of 98.6%, and 94.4% illustrated in Table 2.6.

Table 2.6 Power transfer into four 50 ohm loads from a resonant cavity with a loaded Q of 38.5.

Input Power	Output Loop #1	Output Loop #2	Output Loop #3	Output Loop #4	Total Output Power
1000 W	225 W	271 W	260 W	230 W	986 W
2000 W	460 W	507 W	480 W	440 W	1887 W

Chapter 3

3.0 Triode Oscillator

A means of splitting a high power RF source into many independent loads was presented in Chp. 2. The remaining task for application in high power laser generation is to create a suitable source of high power RF energy. Traditional RF amplifiers or generators are too costly for our presents needs, and indeed these systems provide a linearity and frequency stability that is not essential in exciting a gas discharge. The use of a triode oscillator as a high power RF source will be investigated in this chapter.

All high power radio frequency excited laser systems require large amounts of excitation power. Radio frequency energy may be generated with solid state high power FETs, or with high power vacuum tubes. For power requirements under 1,000 watts, solid state generators are preferable, due to their compact size. Since CO₂ lasers are typically only about 10 - 20% efficient, 1,000 watts will only drive a laser to 200 watts of optical output power. Correspondingly, multi-kilowatt lasers require excitation RF generators considerably in excess of 10 kW. It follows that RF generators which can produce hundreds of kilowatts of RF power are often required in practical high power CO₂ laser systems. Since solid state generators are not practical or economically viable in producing these high power levels, the only logical method for RF generation at this time is to use vacuum tubes.

Three types of high power vacuum tubes are common, namely, triodes, tetrodes, and pentodes. Of these triodes are the least expensive and easiest to use. A typical triode,

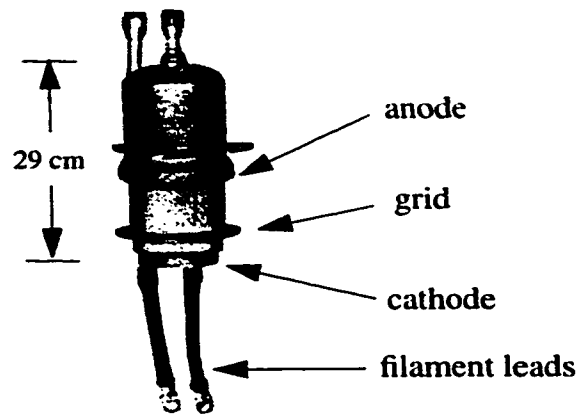


Figure 3.1 Eimac 3CW45,000H3 Triode.

shown in Figure 3.1, consists of a cathode, grid, and anode. Operation of these tubes is categorized into four classes; Class A, AB, B, and C. In addition, the devices may be employed as amplifiers or oscillators. In Class C operation, the plate or anode current of the tube flows for a duration of less than half a cycle, or less than 180 degrees. In order to achieve good efficiency and output power, the plate current will typically be on for 120 to 150 degrees per cycle. Because plate current flows only when the plate supply voltage is high, Class C amplifiers are quite efficient, typically in the 60 to 80% range. One disadvantage of Class C operation is distortion. Distortion arises because the tube's load line is not linear over its entire operating range. As a consequence, low level harmonics will be present in the output. Fortunately, and unlike the case of RF communication, low level harmonic distortion has no adverse effect upon excitation of a laser discharge since the power level contained within these frequencies is so low.

The operation of a triode as an amplifier is considerably more complicated and expensive as compared to running the triode as an oscillator. This is due to the fact that

significant amplification is generally required to raise the low level input signal (typically 0 dBm) to the desired output power level, which is in the tens of kilowatts range. The total amplification required may be 70 dB, and will often require several cascaded stages. In addition, high power triodes with high mu's or amplification factors are more scarce and more expensive than low mu tubes. Because of these factors, an oscillator design was selected, for reasons of reduced overall cost and simplicity, and this has been the subject matter of this investigation.

3.1 Oscillator Design

In the design of any oscillator, the tube constants which define its electronic capabilities must be carefully considered. In triodes, the amplification factor, plate resistance, and transconductance describe in large measure the tube operation. These three parameters are referred to as constants even though they may change significantly over a broad operating range. The amplification factor, more commonly referred to as the mu of the tube, is defined as the rate of change in plate voltage with grid voltage under conditions where plate current remains constant. This parameter is given by²⁶:

$$\mu = \left. \frac{\partial E_p}{\partial E_g} \right|_{I_p} \quad (3.1)$$

The effective resistance of the plate circuit of the tube is known as the dynamic plate resistance and is defined by²⁶:

$$R_p = \left. \frac{\partial E_p}{\partial I_p} \right|_{E_g} \quad (3.2)$$

Transconductance defines the relationship between ac components of grid voltage and plate current. Transconductance is defined by²⁶:

$$g_m = \left. \frac{\partial I_p}{\partial E_g} \right|_{E_p} \quad (3.3)$$

These tube constants are related to each other in the following manner:

$$g_m R_p = \mu \quad (3.4)$$

Transconductance provides a measure of the amplification characteristics of a tube. Plate resistance gives an indication of the desired load impedance. The mu of a tube plays an equally important role in calculating an amplifier's or oscillator's operational behavior.

Voltage and current characteristics of a Class C amplifier configured as a tuned grid and tuned plate circuit will now be discussed. The essential difference between an amplifier and an oscillator is that an oscillator derives its exciting energy from the output circuit. Thus, the output power of an oscillator is reduced accordingly. Figure 3.2 shows a series of typical waveforms. In the electrical schematic of Figure 3.2a, E_b represents the anode DC voltage, while E_c is the external DC grid bias. During operation, the plate voltage oscillates about the DC voltage level with an amplitude of E_L , as shown in Figure 3.2b. It is important to note that the minimum potential on the plate, E_{min} is reached at a point during the cycle at which the grid potential is maximum. Because of this, the value of E_L must always be greater than the maximum peak grid potential, E_{max} . In Figure 3.2c, the peak driving voltage on the grid is indicated by E_s . This potential is either supplied by

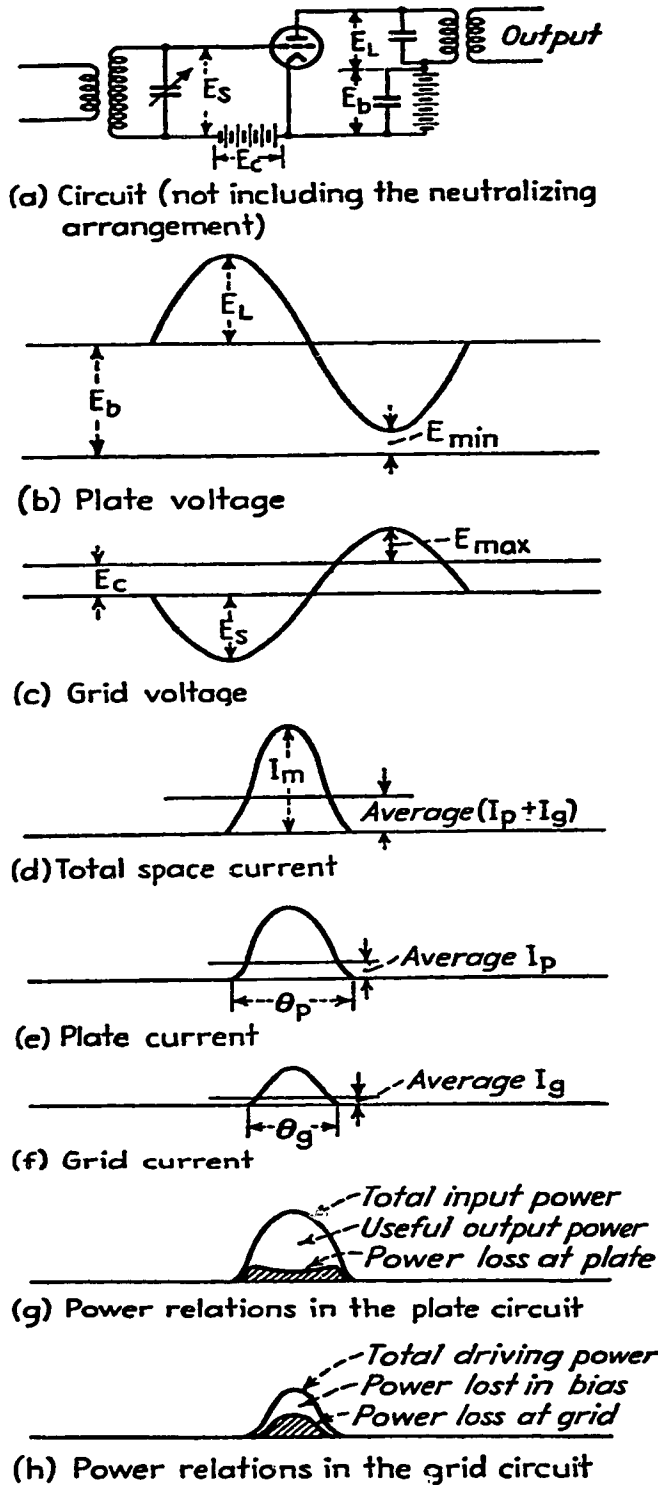


Figure 3.2 Voltage, Current, and Power Relations in a Class C Amplifier³⁰.

an external source or by feedback from the output. An important feature in this design is that the voltage on the grid must be sufficient to drive the grid positive while being 180 degrees out of phase with the output signal. The angular period, θ_g , over which the grid current is positive is given by³⁰:

$$\cos\left(\frac{\theta_g}{2}\right) = \frac{E_c}{E_s} \quad (3.5)$$

For good efficiency and power output, the value for θ_g is usually chosen to be between 120 and 150 degrees. The plate conduction interval is related to the grid parameters in the following manner³⁰:

$$\cos\left(\frac{\theta_p}{2}\right) = \frac{1}{1 + \frac{\mu E_{\max} + E_{\min}}{\mu E_c - E_b}} \quad (3.6)$$

The only parameter not directly affected by the grid is E_{\min} . This value is determined by the load impedance. If the load impedance connected across the tube is very small, it is difficult to generate a large RF voltage. Thus, the efficiency of the tube as an RF energy source is reduced. A further design equation can be derived from the above potentials and current durations, that being the optimum grid bias. For conditions of external bias this becomes³⁰:

$$-E_c = \frac{E_b}{\mu} + \left(E_{\max} + \frac{E_{\min}}{\mu} \right) \frac{\cos(\theta_p/2)}{1 - \cos(\theta_p/2)} \quad (3.7)$$

Peak currents and its relationship to the tube are characterized in Figures 3.2 d-f, along with their average values. Power relationships in both grid and plate circuits are illustrated

in Figure 3.2 g and h. These figures provide a concise picture as to what is physically happening in a triode tube under oscillation or amplification conditions.

3.2 Tank and Cavity Circuits

The most common oscillator circuit utilized for RF frequency generation is the lumped element “tank circuit”. Discrete element inductors and capacitors are employed to create a resonant circuit tuned to the desired operating frequency. Energy is coupled out of this tank circuit to provide the feedback necessary for self-excited operation. Three basic types of tank oscillator circuits are in common usage. These are: Hartley, Colpitts, and tuned-grid tuned-plate.

A Hartley oscillator circuit, illustrated in Figure 3.3, has a single resonant circuit. Oscillation at the desired frequency is achieved by tuning the plate capacitor C_p such that the total system capacitance of C_p and C_{gp} is sufficient to resonate with the inductance of the plate inductor L_p . Feedback necessary for oscillation is achieved by extracting a signal from the plate inductor with proper phase and magnitude. In this manner, an exciting signal is created having an alternating voltage ratio determined by the relative reactances on the two sides of the cathode connection.

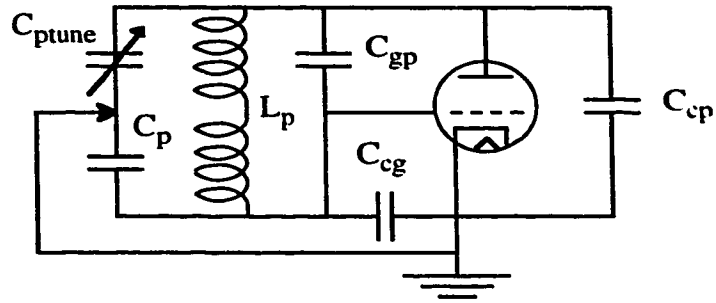


Figure 3.4 Colpitts Oscillator Circuit.

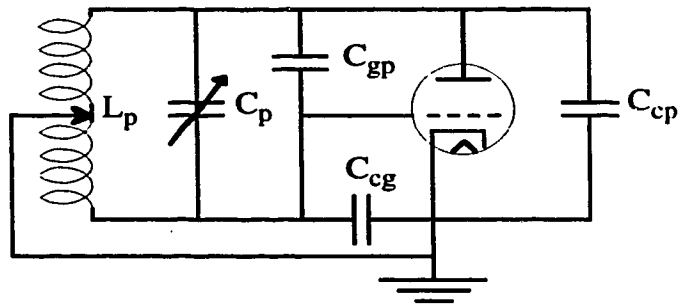


Figure 3.3 Hartley Oscillator Circuit.

Feedback can also be coupled back to the cathode by taking a signal from the plate capacitance. This type of circuit, shown in Figure 3.4, is called a Colpitts oscillator.

The last type of oscillator using a tank circuit is the tuned-grid-tuned-plate. Such a circuit, shown in Figure 3.5, is comprised of two resonant circuits; one for the cathode-

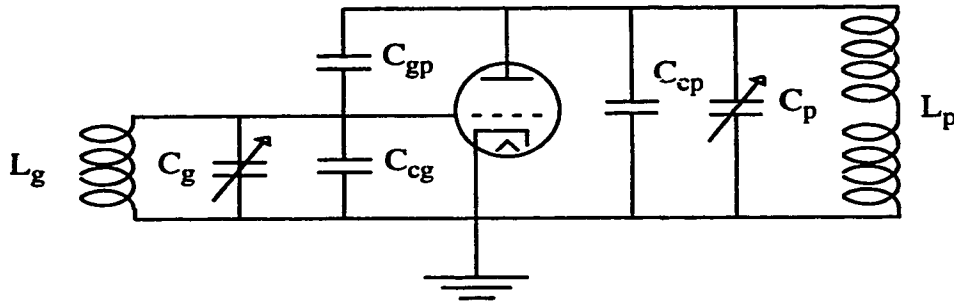


Figure 3.5 Tuned-Grid Tuned-Plate Circuit.

grid, and the other for the cathode-plate. Under normal conditions both circuits L_g, C_g , and L_p, C_p are adjusted to present an inductive reactance at the desired frequency of operation. Magnitude of feedback is determined in the same manner as in the Hartley circuit, since both resonant circuits can be modeled as inductors. Thus, the ratio of exciting voltage to alternating plate-cathode voltage is determined by the relative detuning of the plate and grid circuits.

A less familiar but equally important method of constructing an oscillator circuit employs coaxial resonant cavities to provide output and feedback circuits³¹. Figure 3.6 illustrates such a circuit utilizing two cavities. Both cavities slide over the tube, with spring finger contacts making the electrical connections. It is meaningless to speak of a single RF ground point, since each resonant circuit has high and low potential planes in common. The important aspect here is that there are two distinct cavities, and the term grid-separation oscillator is usually employed. One cavity links the cathode and grid, thereby driving the oscillations. The other links grid and plate, and embodies the output energy of the oscillator. Feedback is derived by extracting energy out of the plate circuit via a small loop, and conducting this signal into the cathode-grid circuit. Proper feedback

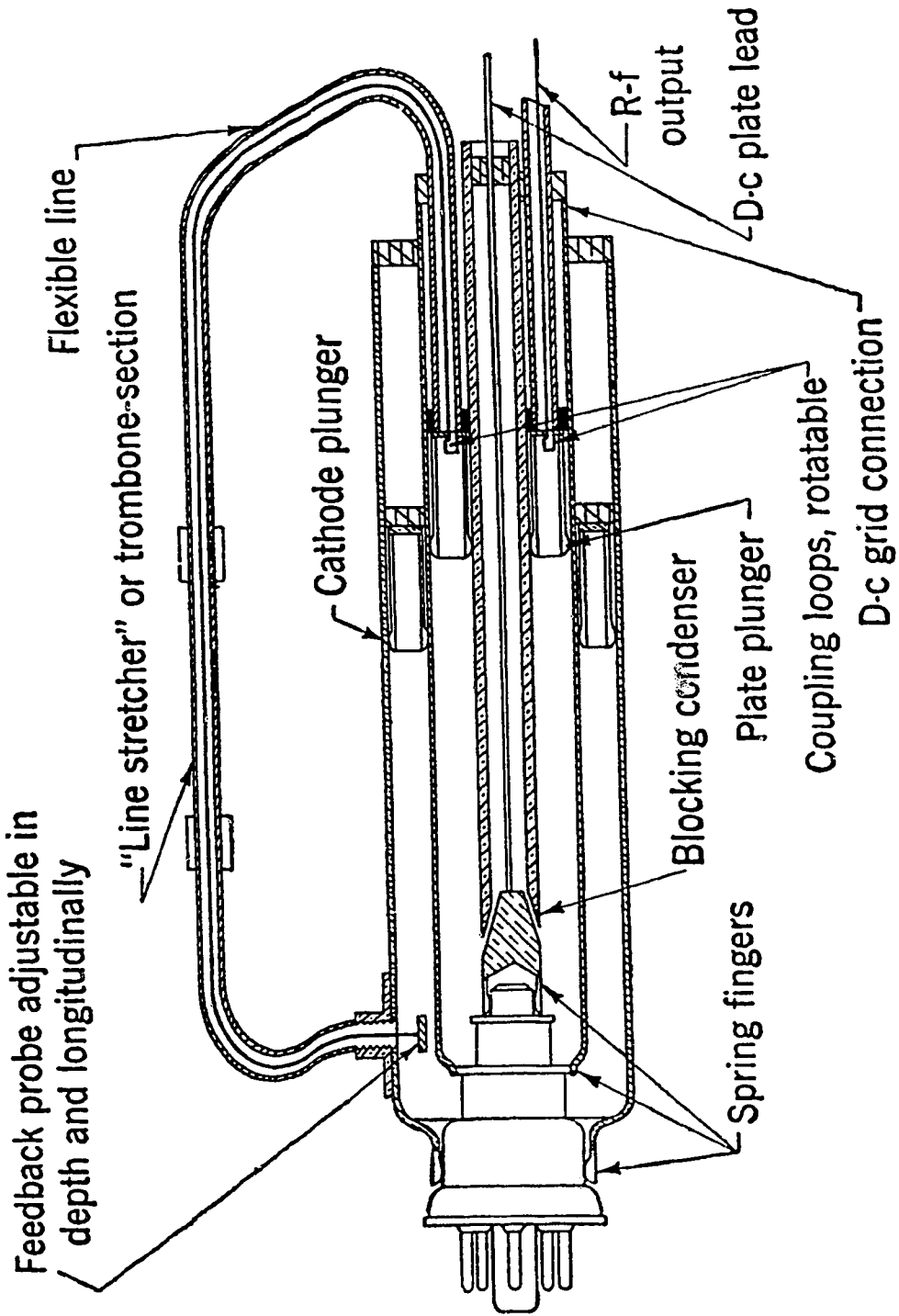


Figure 3.6 Two Cavity Grid Separation Oscillator³¹.

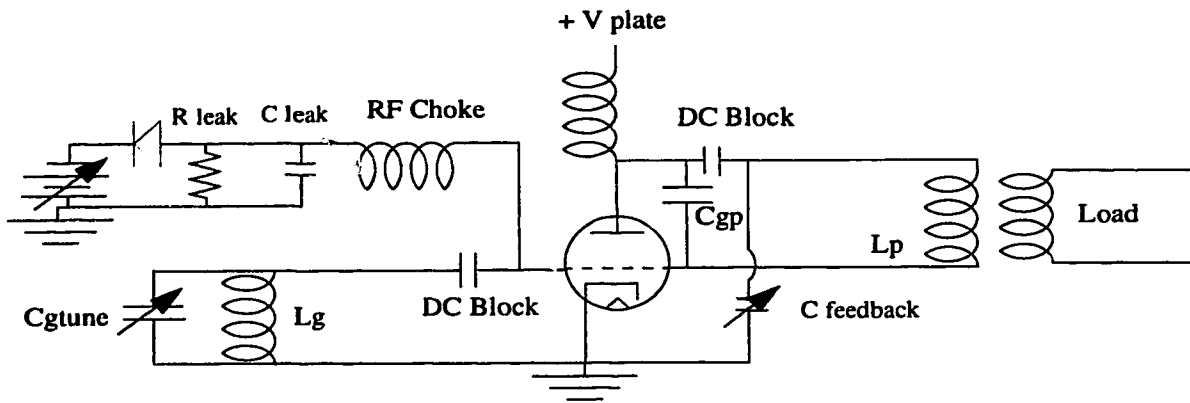


Figure 3.7 Electrical Schematic of Two Cavity Grid Separation Oscillator.

phase and power conditions must be achieved in order to initiate and sustain oscillations. Internal feedback also exists via the tube's internal cathode to plate capacitance. Although grid-separation oscillators have low effective cathode-plate capacitances, the value can still constitute several percent of the grid-plate capacitance. Under such conditions, sufficient feedback voltage is generated internally within the tube to maintain oscillation. Thus, external feedback is not required. If control over the level of feedback is desired, then the tube must be neutralized to eliminate this inherent internal capacitance.

The electrical schematic of the two cavity grid-separation oscillator investigated is shown in Figure 3.7. An Eimac 3CW45,000H3 power triode vacuum tube was used. This ceramic tube has a maximum plate dissipation of 45,000 watts, with nominal interelectrode capacitance values of C_{cg} , C_{cp} , and C_{gp} of 73 pF, 2.3 pF, and 43 pF respectively. Operating frequency is defined by the resonant frequency of $C_{gp}L_p$. Because the cathode-grid circuit is defined by the reactances of C_{gtune} and L_g , their resonance must also coincide with the operating frequency, thereby creating a two cavity coupled system. It is

desirable in the design of the cathode-grid cavity to have the capacitance required for resonance much larger than the tube's internal cathode-grid capacitance. In this manner a much more stable circuit is created, with a greater range of tunability. Feedback necessary to maintain oscillations is achieved by adding an additional capacitor in parallel with the tube's internal cathode-plate capacitance. This capacitance has the effect of increasing coupling between the two cavities and hence the amount of power feedback for driving the tube.

The operating class of the oscillator is determined by the level of grid bias employed. Auto, or self bias is the simplest method. A combination of fixed and self bias derived from the circuitry of Figure 3.7 was used to achieve added flexibility in determining an efficient operating regime. Indeed, it is often preferable to have some externally applied grid bias to prevent low level oscillations. This aspect is particularly important when driving a dynamic load such as a gas discharge. When the tube is biased well below cutoff, operation becomes Class C. This class of operation is much preferable over Class A, since it is inherently more efficient. Practical efficiencies in excess of 70% are not uncommon.

Although there are several choices in oscillator circuits, only the two-cavity grid separation oscillator under Class C operation has proven cost effective in driving a multi-channel laser. Conventional tank circuits were eliminated from consideration, due to the need for a multi-port power splitter. Indeed, the requirement specified is for a uniform division of 100 kW of RF power into 48 individual gas discharge loads while maintaining good isolation between all loads. Theory and experiment have documented that these

stringent requirements can be satisfied by using a coaxial resonant cavity with magnetic coupling loops. An added benefit that is derived by utilizing a resonant cavity power splitter is the elimination of a matching circuit in the output of the oscillator. In the usual construction of tank oscillators, power is coupled out of the circuit either capacitively or inductively, and then matched to a single load impedance, typically 50 ohms. However, by using magnetic coupling loops to extract energy out of a resonant cavity, the oscillating magnetic field induces an emf into each loop. The loops then act as independent voltage sources, capable of delivering RF energy into virtually any impedance. This aspect thereby eliminates the need for matching networks on each of the dynamic loads that a multi-channel gas discharge device comprises. Because of these unique and important advantages, only the cavity coupled oscillator is discussed in this work.

3.3 Oscillator Operational Characteristics

The optimum operating region of the coaxial cavity grid-separation oscillator depends heavily on the internal characteristics of the triode itself. Several tube parameters must be considered when designing an oscillator. Maximum frequency of operation, maximum plate voltage, current, and dissipation, to name a few. Under normal conditions, electron transit time within the tube is negligible compared to the period of oscillation. However, when transit times become an appreciable fraction of a cycle, the feedback voltage on the control grid is no longer of proper phase, thereby causing a reduction in output power. Another effect that limits operation at high frequency is tube inductance. With higher frequencies, the inductance of the grid leads can cause significant loss in drive signal, as well as changing the resonant characteristics of the cavity.

Other operational characteristics, such as maximum plate voltage and current, as well as grid voltage and current are specified by the manufacturer. These factors, which limit the power extractable from the tube under both low or high load conditions, are usually not significant in design unless maximum possible power is to be achieved. Total plate dissipation is another significant characteristic to consider in designing for maximum power deliverable. If tube efficiency is not high, this parameter can easily be exceeded at reduced plate voltage and current ratings. Table 3.1 summarizes the typical operating conditions for the triode as specified by the manufacturer.

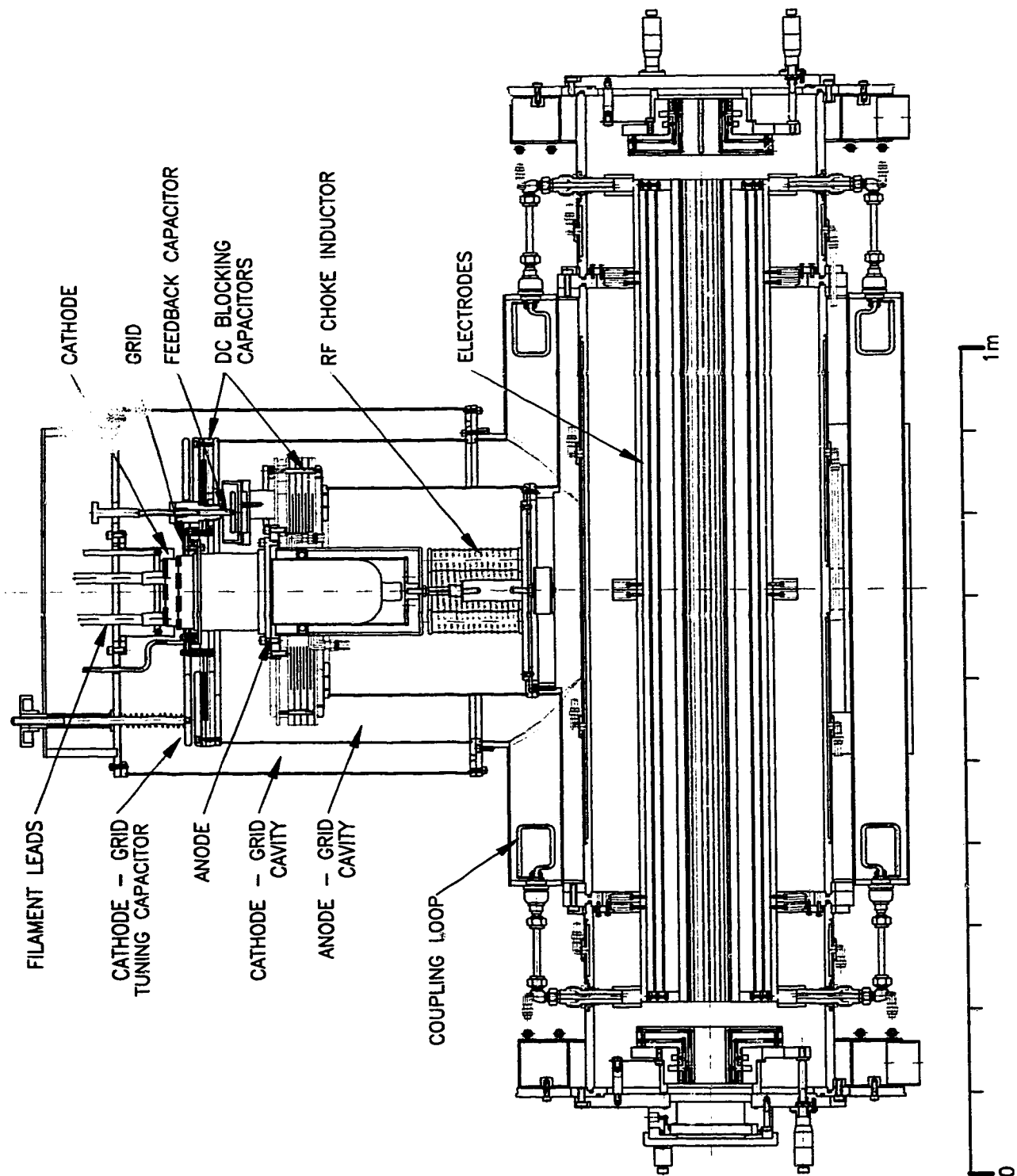


Figure 3.8 Schematic of Zodiac Laser System.

Table 3.1 Technical data for industrial 3CW45,000H3 triode Class C oscillator.

	Maximum Ratings	Typical Operation		
Plate Voltage	14.0 kV	7.0 kV	10.0 kV	13.0 kV
Plate Current	11.5 A	7.7 A	9.0 A	11.5 A
Grid Voltage	- 1.2 kV	- 700 V	- 850 V	- 1000 V
Grid Current	1.2 A	0.53 A	0.74 A	1.01 A
Peak Positive Grid Voltage	na	440 V	550 V	455V
Driving Power	na	600 W	1040 W	1450 W
Plate Input Power	na	54 kW	90 kW	150 kW
Plate Dissipation	na	16 kW	20 kW	29 kW
Plate Output Power	na	37.7 kW	70 kW	120 kW
Approximate Load Impedance	na	408 Ω	526 Ω	570 Ω

3.3.1 Grid Separation Oscillator Design

In designing any oscillator a critical feature is the operating frequency. It is obvious when referring to Figure 3.7, that the anode circuit's frequency of operation is determined by the resonance of L_p with the series combination of C_{gp} and the DC blocking capacitor. DC blocking capacitor design is such that it should have negligible effect on the circuit. This assumption is valid provided that the value of the DC blocking capacitor is at least ten times that of C_{gp} . Thus only the value of the grid to plate capacitance at the frequency of interest need be considered. In Chapter 2, equation 2.2 was developed relating the effective length of a resonant cavity with a specific amount of capacitive loading was developed. Consequently, equation 2.2 can be used in designing the resonant cavity to operate at a desired frequency.

The second cavity which must be constructed is the cathode-grid cavity. Equation 2.2 can again be used to determine the required cavity length and its effective impedance. Since the effects of lead inductances on both circuits can easily change the design

frequency, a generous amount of tuning range should be built into the cathode-grid cavity. This feature is used to accommodate any frequency shifts that may occur due to unspecified stray capacitance or lead inductance. Such tuning is easily achieved by constructing a parallel plate capacitor in parallel with the internal cathode-grid capacitance. If this tuning capacitor is of a value which is made larger than that of the tube itself, it will dominate. Figure 3.8 depicts a cross sectional view of the two cavities, and the cathode-grid cavity tuning capacitor. Adjusting the external cathode to grid capacitance tunes the cathode-grid cavity to co-resonance with the grid-anode cavity. Coarse tuning may be observed by inserting a loop or probe into the two cavities and noting resonance on a network analyzer. Once the tube circuit begins to oscillate, fine tuning is performed while monitoring the tube's operating voltage and current levels.

Other operational parameters that must be determined are the grid bias, as well as the amount of external feedback. If both the amplification factor of the tube and the desired operating voltage are known, one can approximate the required grid bias from Equation 3.7. As an example, consider a tube having a μ of 21, operating in the Class C mode with a plate conduction angle of 120 degrees, and a plate voltage of 7 kV. Equation 3.7 predicts that the grid voltage should be approximately -820 V. This value is consistent with the -700 V recommended by the manufacturer in Table 3.1. With a typical operating grid current of 530 mA, this grid bias can be achieved with a grid leak resistor of about 1.5 k Ω . The disadvantage of using self bias is that bias is only achieved with grid current flow. Because of this fact, the tube cannot be biased below cutoff at start-up. A more flexible circuit was used consisting of a combination of both fixed and self bias circuitry. In this way, a lower fixed bias applied to the tube insures that the tube will be cutoff. Hence

oscillations will not initiate until either a small RF “tickler” signal is introduced into the grid cavity, or until the anode voltage is sufficiently high that the tube turns on by itself. Once the tube is on, the self bias circuitry adds additional grid bias to bring the tube into a more optimum operating region. Experience has shown that a good design for this hybrid bias arrangement is to supply half, or about 400 volts, through the fixed bias supply, and have the other half of the voltage created by the self bias resistor.

The last variable in the design of a self-excited oscillator is the amount of external feedback required for high power operation. As explained earlier, the tube itself has sufficient internal feedback to initiate oscillations. If this oscillation level is somewhat lower in power than required, additional drive power can be obtained by coupling power out of the anode cavity and feeding it back into the cathode. This has the effect of increasing the average plate current, as well as increasing the grid current. The amount of external feedback that the tube can then tolerate is limited to the amount of grid current that the tube can handle.

Taking all the above factors into consideration the basic procedure for optimizing operation of a self-excited oscillator is as follows: The cathode-grid and grid-anode cavities are “cold” tuned with a network analyzer for approximate resonance with each other. Then, while the tube is running, the cathode-grid cavity is tuned to provide maximum grid current under minimum external feedback. Grid bias can then be adjusted to give an adequate level of bias, as specified in the typical operating conditions of Table 3.1. If the level of grid current is low, then the amount of external feedback is increased until the grid current has risen to its typical operating value. If at that point the tube is drawing less average

plate current it is because the tube is driving a load which is of higher impedance than the manufacturer's typical operating conditions. In the event that still more power is required, the dynamic plate resistance must be reduced. This condition implies that the tube be more heavily loaded, hence a greater amount of coupling is needed.

3.3.2 Grid Separation Oscillator Operating Conditions

The operation of a grid separation oscillator in driving a laser is complicated because the changing gas impedance gives rise to time varying load characteristics. Such a dynamic load in turn changes the coupling, or loaded Q of the anode-grid cavity. Since efficiency and power transfer are related to the cavity's unloaded and loaded Q, this variation also changes the amount of RF power that can be delivered to the gas discharge loads. A magnified effect is seen, since as the discharge impedance drops, the cavity is more heavily loaded, which in turn drives the tube harder. Consequently, more RF power is deposited into the discharge loads and a concomitant lesser percentage is dissipated in the cavity itself. Thus, high efficiency in RF energy transfer requires heavy cavity loading.

Equation 2.18 describing power transfer efficiency of a cavity circuit, does not apply directly to the two cavity grid separation oscillator circuit. It describes the efficiency of power transfer through a passive two port system. However, by having the tube mounted integrally with the cavity, energy is no longer coupled into the cavity from an external source, but rather the cavity itself now becomes the RF energy source. Because of this fact the equation for efficiency of power transfer now becomes:

$$\eta = \left(1 - \frac{Q_L}{Q_u} \right) \quad (3.8)$$

The reason that this equation is different from Equation 2.18 is that since the tube is now part of the energy distribution system, it also affects the cavity Q. Indeed, the dynamic plate resistance of the tube will change to match the output coupling of the cavity. Consequently, the Q of the cavity drops to about half of what it is when the tube is off. As an example, consider the case of a cavity that has a Q of 500 with the tube mounted inside it. Without any power being extracted, the tube's dynamic plate resistance will be equal to the parallel resistance of the unloaded cavity. Hence the tube will have the same Q as the cavity of 500. Equation 2.11 describes how the cavity Q's affect each other and the resulting Q will be 250. Since this is the Q of the cavity without any power extracted, yet with all the voltages and currents running through the tube, this now becomes the effective unloaded Q of the cavity as per Equation 3.8. If power is extracted out of the cavity and the loaded Q of the cavity is lowered to 25. Equation 3.8 predicts that the efficiency will be 90%. Comparing this to the case of a two port cavity using Equation 2.18 with an unloaded Q of 500, gives a power transfer efficiency of 90% also. So, in fact, although the two efficiency equations are different, the cavity still operates the same once the effect of the tube on the cavity Q is taken into consideration.

Measurement of cavity Q under operating conditions is not a simple matter. However, the unloaded Q can be measured with a network analyzer. This was found to be around 700 for the anode-grid structure. Hence, the effective unloaded Q when the tube is on will be only 350. Previously, cavity Q measurements of the two port T cavity gave values of the unloaded Q of around 2000. Thus, the effect of having the tube inside the cavity

with DC blocking capacitors and coupled to another lower Q cavity, caused the unloaded Q of the anode unit to fall quite significantly. This has a detrimental effect on the efficiency of power transfer.

Measurements of both the tube's efficiency and the cavity's energy transfer efficiency were performed by recording power lost in heating those respective elements. In the first instance, knowing the DC input power and subtracting power lost in anode heating, the RF output power can be inferred. Through measuring the heat absorbed in the electrodes, an estimate of RF power delivered to the gas discharges can also be obtained. Comparison of these two values then gives an estimate of the cavity's power transfer efficiency.

Table 3.2 represents the Class C oscillator's operating conditions for the case where the load consists of two 50 ohm loads coupled by loops 15 x 4 cm² in area. Tube

Table 3.2 Triode operating conditions while driving two 50 ohm loads.

Grid Bias	Grid Current	Plate Voltage	Plate Current	Power Out 1	Power Out 2	Anode Temp. Rise in °C	Freq. in MHz
-675 V	240 mA	3 kV	1.6 A	650 W	800 W	1 3/4	80.37
-530 V	250 mA	3 kV	1.2 A	600 W	800 W	1 1/4	80.02
-690 V	360 mA	4 kV	1.5 A	1200 W	1450 W	1 1/2	80.03
-640 V	250 mA	4 kV	1.4 A	1200 W	1450 W	1 1/2	79.79
-700 V	370 mA	5 kV	1.7 A	1800 W	2100 W	2	79.82
-775 V	530 mA	6 kV	2.1 A	2600 W	3100 W	2 3/4	79.83
-700 V	370 mA	6 kV	1.8 A	2500 W	3000 W	2 1/2	79.94
-750 V	480 mA	7 kV	2.1 A	3300 W	4000 W	3 1/4	79.94

efficiencies and cavity transfer efficiencies obtained were approximately 60% and 80% respectively. There is an uncertainty of about ± 10% in both of these measurements due to

the error in measuring water temperature and powermeter accuracy. Even with this relatively large uncertainty it was still apparent that significant improvement in the tube's efficiency was achieved through proper tuning of the cathode-grid cavity. Indeed when the cathode-grid cavity was retuned, thereby lowering the operating frequency slightly from 80.37 MHz to 80.02 MHz, plate current was reduced without any loss in RF output power. This data, illustrated in Table 3.2 represents a significant enhancement in efficiency.

Under experimental conditions where the tube drove four 50 ohm loads coupled to the cavity by four loops each 15 x 4 cm² in area, plate current increased, as compared to the two load case. This observation is consistent with a heavier loaded cavity, since when plate resistance drops, a corresponding increase is expected in plate current. Tube and cavity efficiencies were not measured during this test. Table 3.3 gives the operating conditions for this four load case with loads 3 and 4 limited to 1000 and 500 watts respectively.

Table 3.3 Operating conditions driving four 50 ohm loads.

Grid Bias	Grid Current	Plate Voltage	Plate Current	Load 1	Load 2	Load 3	Load 4
-60 V	100 mA	1 kV	900 mA	80 W	100 W	100 W	136 W
-140 V	190 mA	1.3 kV	1.1 A	100 W	130 W	120 W	165 W
-330 V	340 mA	2 kV	1.7 A	360 W	440 W	440 W	490 W
-540 V	350 mA	2 kV	1.6 A	400 W	420 W	480 W	433 W
-610 V	470 mA	2.5 kV	2 A	600 W	460 W	700 W	619 W
-670 V	400 mA	2.5 kV	1.8 A	600 W	640 W	720 W	419 W
-710 V	500 mA	3 kV	2.1 A	800 W	860 W	940 W	535 W

When the RF load was a gas discharge, power meters could not be used, as there was no provision to install them between the cavity and electrode. Under these conditions, power deposited into the gas was determined by measuring temperature rise of the elec-

trodes. This was accomplished by installing a flow meter and thermometer in-line with one electrode. With this set up, cooling water flow and temperature could be monitored simultaneously. Table 3.4 gives the operating conditions for driving two discharge channels, along with estimates of the tube's operating efficiency, and cavity's power transfer efficiency. Errors in discharge power measurements are quite high at plus or minus 200

Table 3.4 Triode operating conditions while driving two discharge channels @ 80.5 MHz.

Grid Bias	Grid Current	Plate Voltage	Plate Current	RF Output	RF in Discharge	Tube Eff.	Cavity Eff.
-370 V	80 mA	4.4 kV	3.3 A	6.3 kW	620 W	45%	10%
-470 V	310 mA	4.2 kV	2.2 A	4.9 kW	830 W	55%	17%
-470 V	300 mA	4.5 kV	2.4 A	5.6 kW	620 W	53%	11%
-740 V	400 mA	5 kV	2.2 A	5.8 kW	1000 W	54%	18%

watts, due to the accuracy of temperature measurement. With only two discharge channels running, the approximate cavity efficiency drops to only 15%. The tube however, ran above 50% efficiency. Comparing the above performance with the two 50 ohm load case, it is clear that cavity efficiencies are much lower when driving the discharge. This is caused by the fact that the discharge has an effective impedance much higher than 50 ohms, under the drive conditions of 500 watts per discharge channel with 20 torr gas pressure.

In order to examine the effect of increased loading on energy transport efficiency, several additional electrodes were magnetically coupled into the cavity. Table 3.5 gives

the operating conditions with five discharge channels operating at a gas pressure of 15 torr.

Table 3.5 Triode operating conditions while driving five discharge loads @ 80.5 MHz.

Grid Bias	Grid Current	Plate Voltage	Plate Current	RF Output	RF in Discharge	Tube Eff.	Cavity Eff.
-480 V	300 mA	5.3 kV	3.0 A	10 kW	1.9 kW	65%	19%
-690 V	360 mA	5.3 kV	2.7 A	9 kW	3.0 kW	65%	33%
-720 V	415 mA	6 kV	2.95 A	11.9 kW	3.0 kW	69%	25%
-780 V	515 mA	7 kV	3.4 A	14.8 kW	2.4 kW	64%	16%

Since it was not practical to monitor the temperature on all six electrodes, discharge power was estimated by monitoring the heat deposited into only one electrode, and multiplying this number by 5. There was a significant error in measuring the RF power deposited into the discharge using the above procedure, at low power levels, due to the fact that not all the discharge channels were uniformly excited. As an example, Table 3.5 indicates that at 7 kV plate voltage, discharge power dropped as the tube was driven harder. Visually however, the discharge appeared brighter. This apparent anomaly resulted when other discharge channels started to fill, and consequently energy was taken away from the electrode under measurement.

Table 3.6 gives the observed operating tube conditions while driving eight discharge channels. As can be seen from the data, cavity efficiency increased from about

Table 3.6 Triode operating conditions while driving eight discharge loads @ 80.5 MHz.

Plate Voltage	Plate Current	RF Output	RF in Discharge	Tube Eff.	Cavity Eff.	Gas Pressure
6 kV	5.2 A	18.7 kW	3.4 kW	63%	18%	15 torr
6 kV	4.2 A	15.3 kW	3.4 kW	63%	22%	15 torr
6 kV	4.4 A	16.4 kW	4.2 kW	64%	26%	20 torr
7 kV	5.0 A	20.9 kW	5.1 kW	62%	24%	20 torr
7 kV	5.1 A	21.5 kW	6.7 kW	63%	31%	25 torr

Table 3.6 Triode operating conditions while driving eight discharge loads @ 80.5 MHz.

Plate Voltage	Plate Current	RF Output	RF in Discharge	Tube Eff.	Cavity Eff.	Gas Pressure
8 kV	6.0 A	27.7 kW	7.6 kW	60%	27%	25 torr
8 kV	6.2 A	27.5 kW	7.6 kW	58%	28%	30 torr
8 kV	5.8 A	26.2 kW	8.4 kW	59%	32%	30 torr
8 kV	5.0 A	22.0 kW	8.4 kW	57%	38%	30 torr
8 kV	4.3 A	20.1 kW	8.4 kW	60%	42%	30 torr
9 kV	4.6 A	24.9 kW	9.3 kW	62%	37%	30 torr

20% with 5 discharges, to well over 30% when driving 8 discharge loads. Tube efficiency in both cases remained near 60%. However, close examination reveals that there was significant change in the tube's current-voltage characteristics. This was caused by changes in the level of external feedback applied, and the required retuning of the cathode-grid cavity.

Although very interesting from the standpoint of tube efficiencies, the data of Table 3.6 was not particularly impressive with respect to cavity efficiency. This being the case, preliminary attempts at optimization were made. Specifically, two potential loss mechanisms were identified which detracted from system performance. One was a lossy movable short circuit in the cathode-grid cavity, used to provide a greater range of tuning. The second was a fully coupled loop installed into the cathode-grid cavity, used to inject a low level RF trigger signal. The effect of removing this lossy short was a reduction in grid current by 45%, with no change in grid bias, or plate voltage and current. This feature meant that additional external feedback could be applied, thereby yielding increased overall output power, without overloading the grid. Decoupling the grid trigger loop enhanced feedback power within the grid-cathode cavity by up to 135 watts. This design

change further elevated grid current by 25% to 30% with a corresponding 7% decrease in plate current.

Each of the above effects resulted in an improvement in the cavity, as is illustrated in Table 3.7. It is apparent from the data that the tube becomes less efficient as it is driven harder. This is to be expected, since as the cavity heats up, retuning is necessary to bring the oscillator back into the high efficiency operation region. Comparing the cavity efficiencies above with those in Table 3.6 reveals that an improvement in efficiency of about 10% was achieved by properly tuning the grid cavity to the desired frequency of operation.

Table 3.7 Triode optimized operating conditions while driving eight discharge loads @ 80.5 MHz.

Plate Voltage	Plate Current	RF Output	RF in Discharge	Tube Eff.	Cavity Eff.	Gas Pressure
7 kV	2.95 A	14.9 kW	6 kW	74%	40%	15 torr
7 kV	3.3 A	16.8 kW	7.6 kW	75%	45%	24 torr
8 kV	3.8 A	20.9 kW	8.9 kW	70%	43%	24 torr
9 kV	4.2 A	23.3 kW	9.2 kW	63%	40%	23 torr
9 kV	4.5 A	25.8 kW	10.1 kW	65%	39%	30 torr

It is clear from the trend illustrated in Tables 3.6, and 3.7 that energy transport efficiency of the cavity improves markedly with increased discharge loading. Thus, when the full 24 channels are magnetically coupled into the system, significantly higher cavity efficiencies are anticipated.

Chapter 4

4.0 Results

Radio frequency energy was used to excite a multi-channel laser consisting of 24 electrodes, each 5 cm in width and 1 meter long. The gap separating the electrodes was adjustable by means of support rings. For the case under consideration here, the electrode gap was chosen to be approximately 3 mm. This electrode structure is illustrated in Figure 4.1. For efficient laser operation, uniform excitation of the gas discharge along the entire length of the electrode is necessary. When energy is fed into the discharge channels at both ends, multiple reflections produce a standing wave over the full electrode length³². If the length of the electrode is a significant proportion of the excitation wavelength, the non-uniform wave amplitude can become excessive. Under such conditions this non-uniform voltage distribution must be corrected through the use of reactive elements judiciously selected and distributed along the electrode length.

In this chapter an effective technique for improving the uniformity of voltage distribution along the length of a strip-line electrode will be presented. RF power deposition measurements confirm that a reasonably uniform discharge can indeed be achieved. Preliminary optical extraction measurements, featuring up to eight discharge channels, serve as an indicator of the usefulness of this smoothing technique and its scalability for driving a multi-channel laser system.

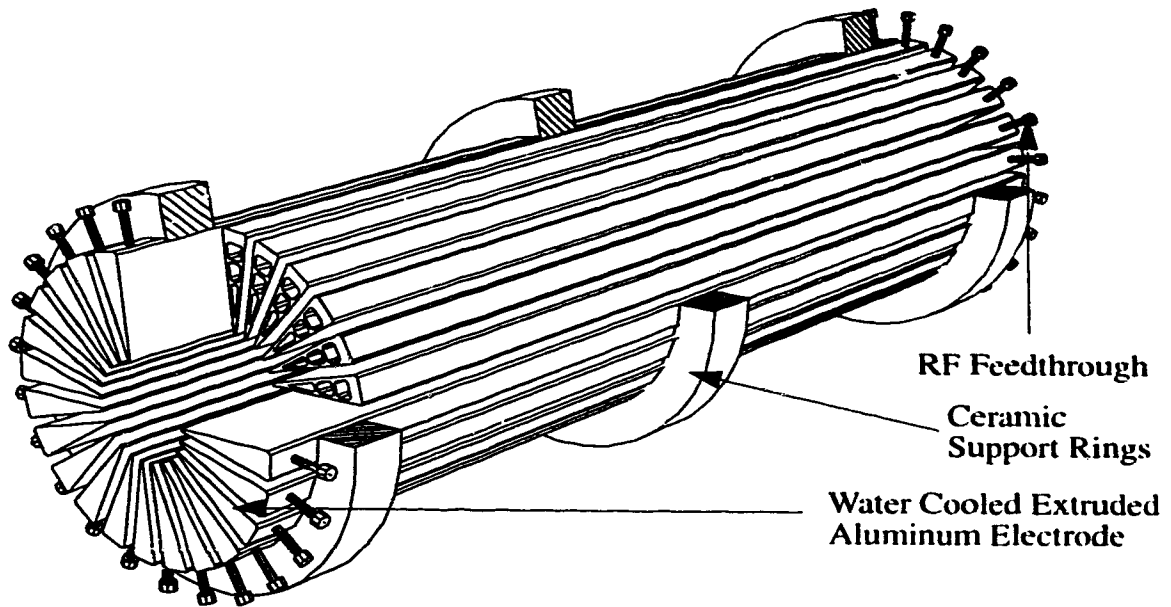


Figure 4.1 Radial Slab Electrode Array.

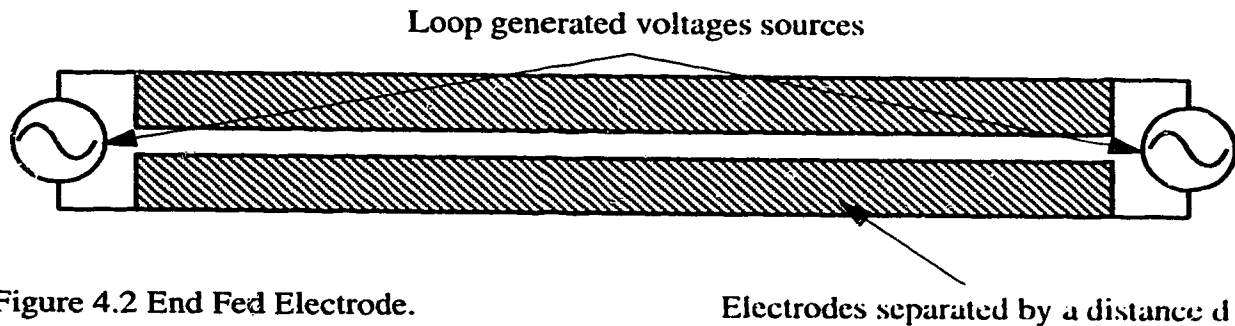


Figure 4.2 End Fed Electrode.

4.1 Discharge Uniformity

Each gain channel is enclosed by two parallel plate electrodes comprising a strip transmission line 5 cm in width and separated by a gap of 3 mm. As RF energy propagates along the 1 meter transmission line, reflections occur at each end due to impedance mismatches. Since the electrode is fed from both ends, the mismatch is between the impedance of the transmission line and the feedthroughs characteristic impedance. Figure 4.2 illustrates this double end fed electrode.

Modeling voltage uniformity along the transmission line may be accomplished by dividing the electrode into many segments. Each segment can then be described by the following equations²⁴:

$$V_i(z) = A_i e^{-\gamma_i z} + B_i e^{\gamma_i z} \quad (4.1)$$

$$I_i(z) = \frac{A_i}{Z_{0i}} e^{-\gamma_i z} + \frac{B_i}{Z_{0i}} e^{\gamma_i z} \quad (4.2)$$

where A_i , and B_i are respectively the amplitude of forward and reverse travelling wave modes on the i^{th} segment, and V_i , I_i are respectively the voltage and currents phasors on the i^{th} segment.

The propagation constant γ , and the line impedance Z_0 are given by:

$$\gamma = \sqrt{(R + j\omega L)(G + j\omega C)} \quad (4.3)$$

$$Z_0 = \sqrt{\frac{R + j\omega L}{G + j\omega C}} \quad (4.4)$$

Values of R , G , L , and C represent the transmission line's resistance, shunt conductance, inductance and capacitance respectively, all defined per unit length. In the absence of a discharge these parameters become:

$$R = \frac{2}{w\sigma\delta_s} \quad L = \frac{\mu_0 d}{w} \quad G = 0 \quad C = \frac{\epsilon_0 w}{d} \quad (4.5)$$

where w is the electrode width, d the electrode separation, σ the electrical conductivity, and δ_s the surface resistivity of the electrode material. In the presence of a discharge, the magnitudes of L , G , and C will be altered due to plasma resistivity and sheath capacitance.

The established method of compensating for a non-uniform transmission line voltage requires that the shunt resistance of the discharge be large, compared to the capacitive reactance of the electrode, and that the capacitive loading contributed by plasma sheaths be negligible in comparison to the electrodes' static capacitance^{33,34,35}. This condition is not necessarily true, particularly at high power loading in wide electrodes. In some instances, the condition is created by adding a distributed capacitance in parallel with the electrode assembly. In this approach, a high dielectric material such as alumina is sandwiched between the parallel plates comprising the electrode. An order of magnitude increase in the effective electrode capacitance can thus be achieved. Under this condition, the transmission line can be modeled as a low loss line.

Capacitively loading the transmission line in this manner has two disadvantages. The first stems from impeded gas re-circulation within the inter-electrode volume, resulting in degradation of laser performance. Secondly, the additional distributed electrode capacitive loading shortens the wavelength of the exciting RF energy. A shorter RF wavelength demands more distributed inductors to nullify standing waves along the line. More inductors also leads to a circuit which is more sensitive to power variations. For reasons outlined above, no distributed capacitance is added between the electrode channels in the Zodiac laser. Consequently, a more exact model must be used to account for discharge effects upon the shunt conductance, and net capacitance of the lossy transmission line.

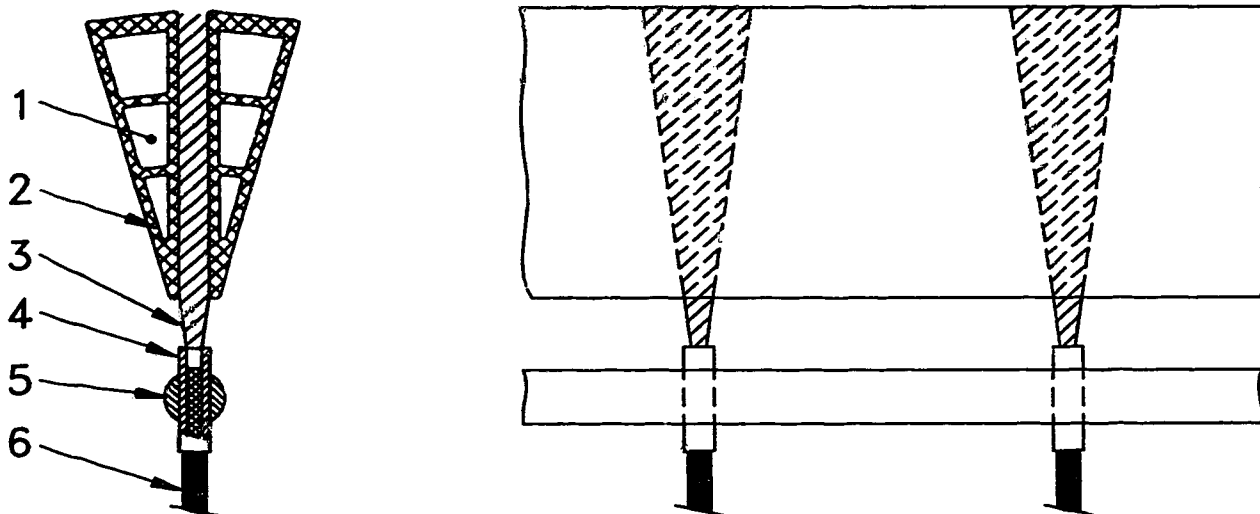


Figure 4.3 Discharge Uniformity Detector.

(1) Water Cooling Channel (2) Extruded Aluminum Electrode (3) Field of View of Optical Detector (4) Ceramic Tube (5) Aluminum Support Rod (6) 1 mm Diameter Fibre Optic Cable

Recent publication of relevant parameters characteristic of a slab discharge³⁶ has permitted the development of a computer code which predicts inductor placement to achieve a desired voltage uniformity profile. This model, developed as part of a Ph.D. dissertation³⁷, was verified experimentally through luminosity measurements using a fiber optic detector array developed specifically for the purpose.

The fiber optic detector, illustrated in Figure 4.3, consists of 11 fibers, spaced 10 cm apart along an aluminum rod. Each 1 mm diameter plastic fiber, is fitted through a ceramic tube to restrict its field of view such that only a localized portion of the discharge is sampled. Discharge luminosity is then measured by a phototransistor and amplified with an operational amplifier, or op amp, to give a suitable signal-to-noise ratio.

To ascertain the relationship between discharge luminosity and input power, at varying gas pressures, a sample discharge cell was constructed. Specifically, a small elec-

trode segment 2 cm in width, and 5 cm long was built to eliminate length effects. Electrode separation of 3 mm was identical to that of the laser electrodes. Discharge luminosity was also measured using an identical collecting fiber and amplifying circuit, as used in the uniformity measurements. Figure 4.4 illustrates the results of this experiment. From the data it is obvious that a linear correlation does indeed exist between discharge luminosity and input power. Because of this fact, a convenient and accurate diagnostic method was achieved for discerning uniformity of RF power deposition within the inter-electrode volume.

The amplifying circuit used to obtain discharge luminosity data from this inter-electrode region is illustrated in Figure 4.5. A Siemens phototransistor SHF-350 was used, since it has a linear optical energy response. The measurement signal was further amplified through the use of a stable, low drift, op amp. Each fiber had its own circuit, which was subsequently calibrated. After exploring a number of calibration procedures, the best method involved the use of a movable fluorescent light assembly. With this apparatus, each fiber opening viewed the same luminous region under the light. Each amplifying circuit was then adjusted to give the same reading.

A series of experiments were then performed to validate the discharge uniformity model³⁷. One channel, driven by two electrodes, was excited by an external 10 kW RF generator operating at 82 MHz. Input power to the electrodes was determined via calorimetry measurements. These were accomplished on the electrode's cooling water, through the use of an in-line flow meter, and a thermometer. Optical luminosity measurements were performed at various power levels. The most uniform case occurred at a gas pressure

Discharge Luminosity vs. Input Power

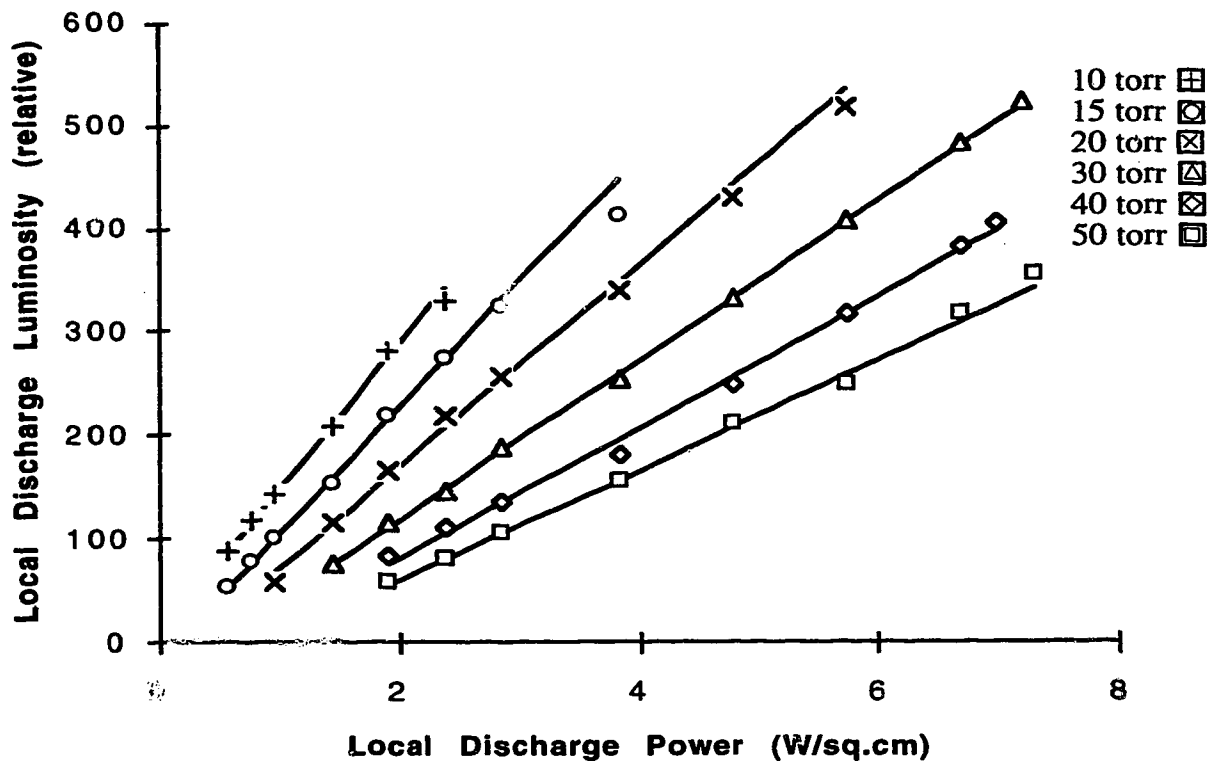


Figure 4.4 Discharge Luminosity at Various Pressures.

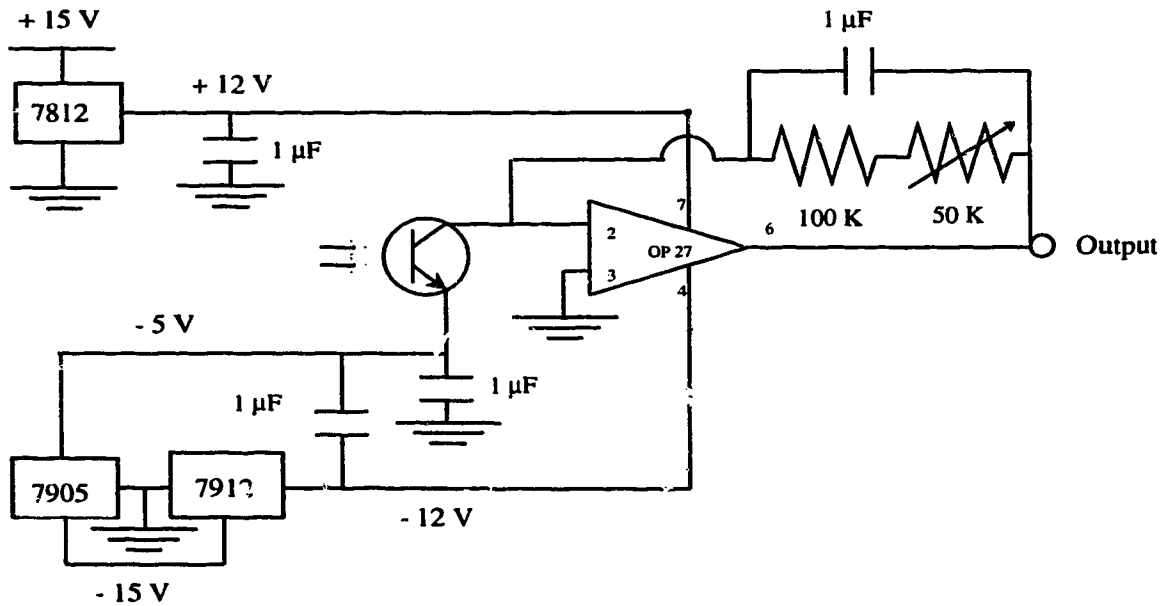


Figure 4.5 Electrical Schematic of Detector Amplifier Circuit.

of 20 torr, under an input RF drive power of 1700 watts. This data is shown plotted in Figure 4.6, along with a theoretical power distribution curve derived from the discharge uniformity model^{38,39}. Two inductors, each 15 ohms @ 82 MHz, were used in this experiment. The position of the inductors was 37.5 cm from the ends of the electrode, and correspond in position to the reduced power level represented by the theoretical curve of Figure 4.6.

Theoretical simulation and experimental data reveal that if the discharge volume is not excited to the same level for which the smoothing inductors are chosen, then the discharge will become increasingly non-uniform. In a weakly excited discharge, the discharge half way down the length of the electrode becomes weaker. However, in the case of over excitation, the discharge is more intense centrally. Figure 4.7 illustrates the situation where the gas is weakly excited. This case employs four inductors to smooth the voltage standing wave. Inductor values @ 82 MHz are 17, 13, 13, and 17 ohms respectively, placed 20, 40, 60, and 80 cm from the front of the electrode. Here it is clear that power deposition into the discharge is indeed much weaker in the center of the electrode. Exciting the gas at an optimum power level increases uniformity, as is shown in Figure 4.8. One noticeable aspect of Figure 4.8 is the skew in the curve. An asymmetric voltage feed of 1% between the two ends of the electrodes can give rise to such a distribution. Theoretically this effect is more pronounced in the four inductor case, as compared to the two inductor case. Because of this, and the fact that using only two inductors yields a much larger dynamic range of uniformity with respect to input drive power variations, the two inductor case will be examined in detail herein for driving multiple discharge channels.

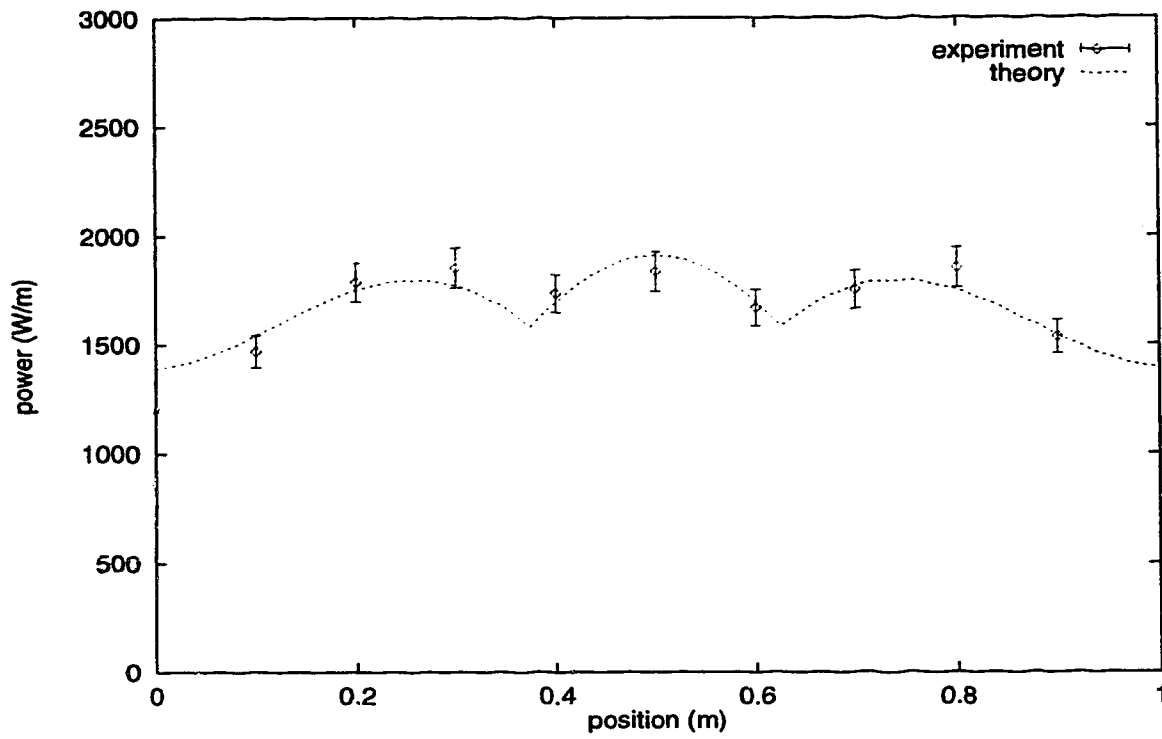


Figure 4.6 Discharge Uniformity With Two Inductors At 20 Torr Gas Pressure³⁷.

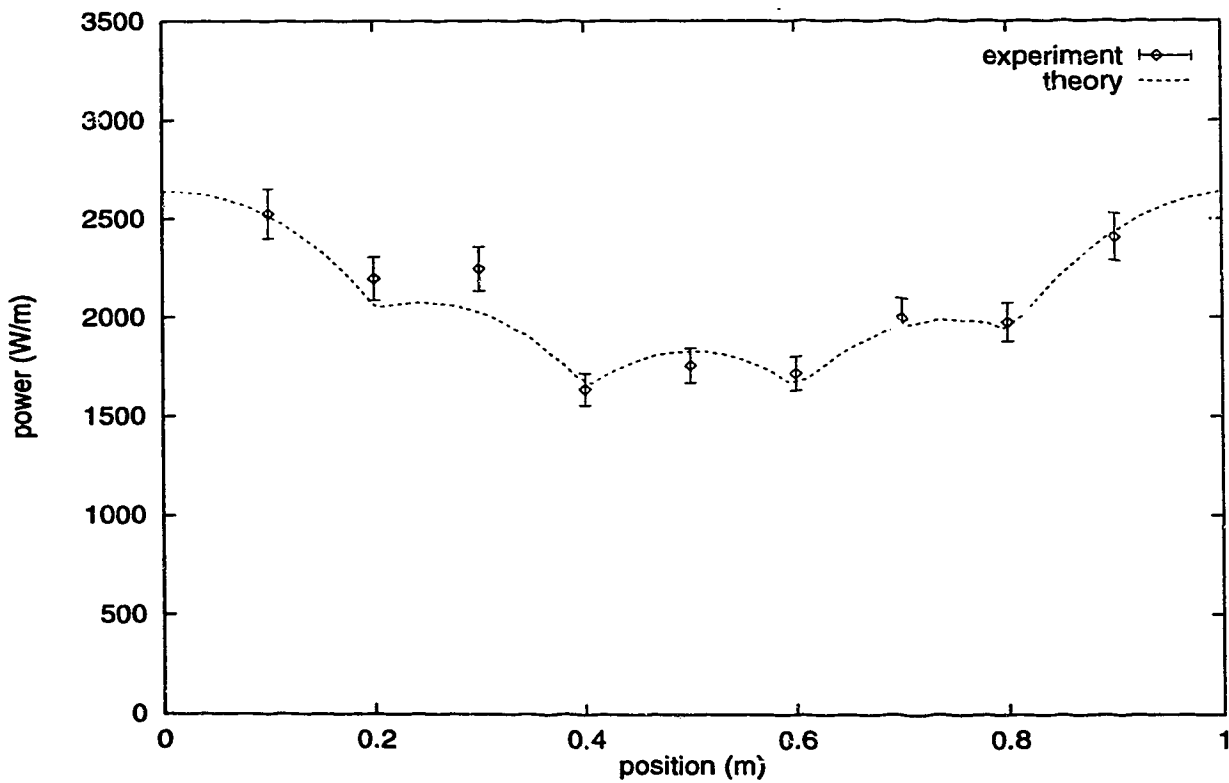


Figure 4.7 Four Inductor Discharge Uniformity at 20 Torr Gas Pressure Driven Weakly³⁷.

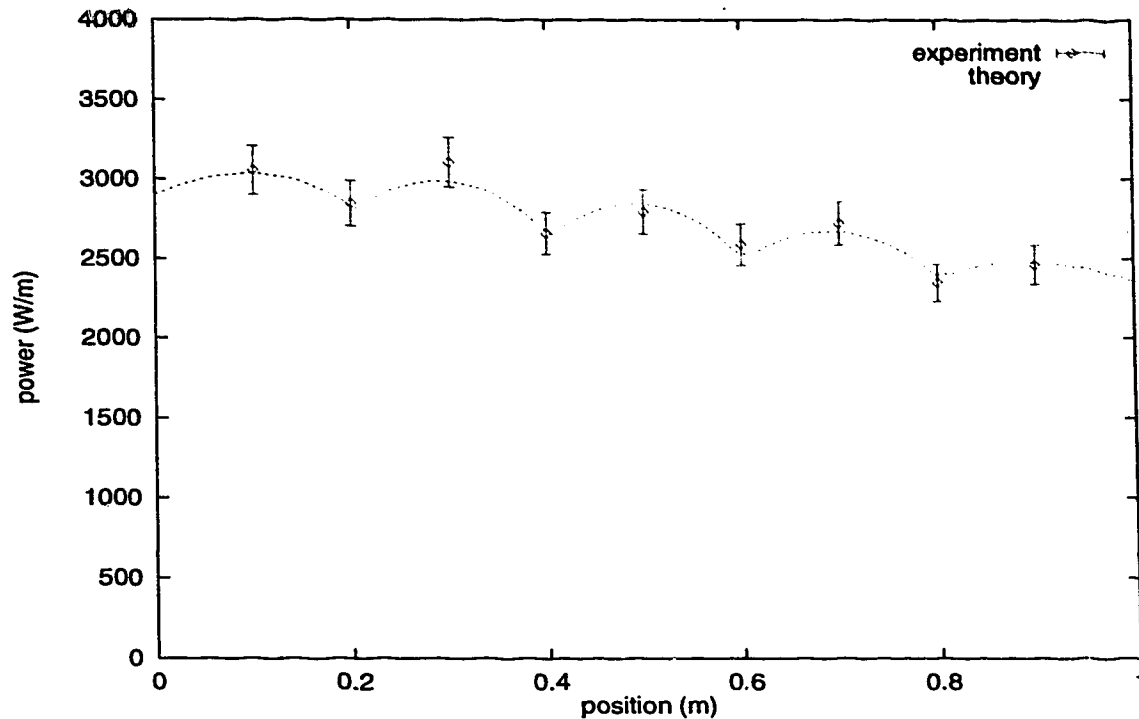


Figure 4.8 Four Inductor Discharge Uniformity At 20 Torr Gas Pressure Driven Optimally³⁷.

4.2 Laser Output Power

Once a reasonably uniform discharge had been achieved, mirrors were placed in the vacuum vessel to extract optical power. This section of the thesis is divided into two parts; optical extraction from a single discharge channel, followed by multi-channel optical extraction.

4.2.1 Single Channel Optical Extraction

Optical experiments were performed to ascertain the output power capability of a single channel, and its associated optimum mirror output coupling. Output coupling of a mirror refers to the percentage of the geometric exit aperture of the slab electrode. In this terminology, a 50 mm wide electrode with an output coupling of 25% would have a laser

beam 12.5 mm wide. Every laser has an optimum coupling under which the maximum amount of optical stimulated radiation can be extracted. If too little coupling is used, then beam intensity inside the resonator (between the mirrors), becomes too large and correspondingly saturates the gain medium. Conversely, if too much coupling is employed, beam intensity never becomes sufficient to stimulate the maximum amount of photons possible. An ideal level of coupling therefore features an intra-cavity beam whose intensity is just strong enough to stimulate maximum photon emission.

Tests were performed on a single pair of electrodes to determine proper output coupling. Power was extracted using aluminum mirrors 5.7 cm in diameter. Three sets of optics were machined with curvatures giving a geometric output coupling of 13%, 25%, and 35%. The dependence of the laser power on discharge power and pressure is shown in Figures 4.9 to 4.11. Figure 4.12 illustrates the three different coupling factor cases by comparing extractable laser power under the same excitation level and pressure conditions. It is obvious that an output coupling factor of 25% is the best of the three cases examined, and was subsequently chosen for extracting power from the multiple electrode array.

In the initial phases of this study, and before a discharge computer model was developed^{38,39}, a first attempt at plasma uniformity was achieved largely by trial and error. In this process, smoothing inductors were placed across the electrodes, and visual acuity employed to identify the most uniform case. Through this iterative experimental procedure, inductor impedances were chosen with values of 45, 20, 20, and 45 ohms @ 82 MHz to give the most visibly uniform profile. Placement of these inductors were 23,

Output Power with 13% Output Coupling

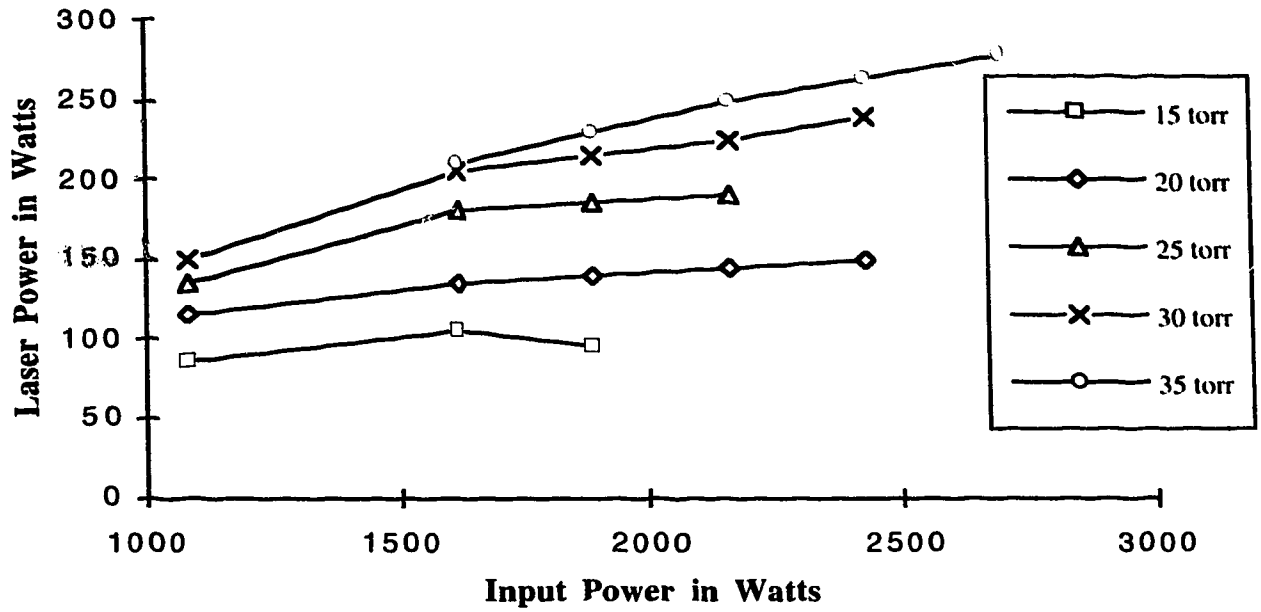


Figure 4.9 Laser Power with 13% Output Coupling.

Output Power with 25% Output Coupling

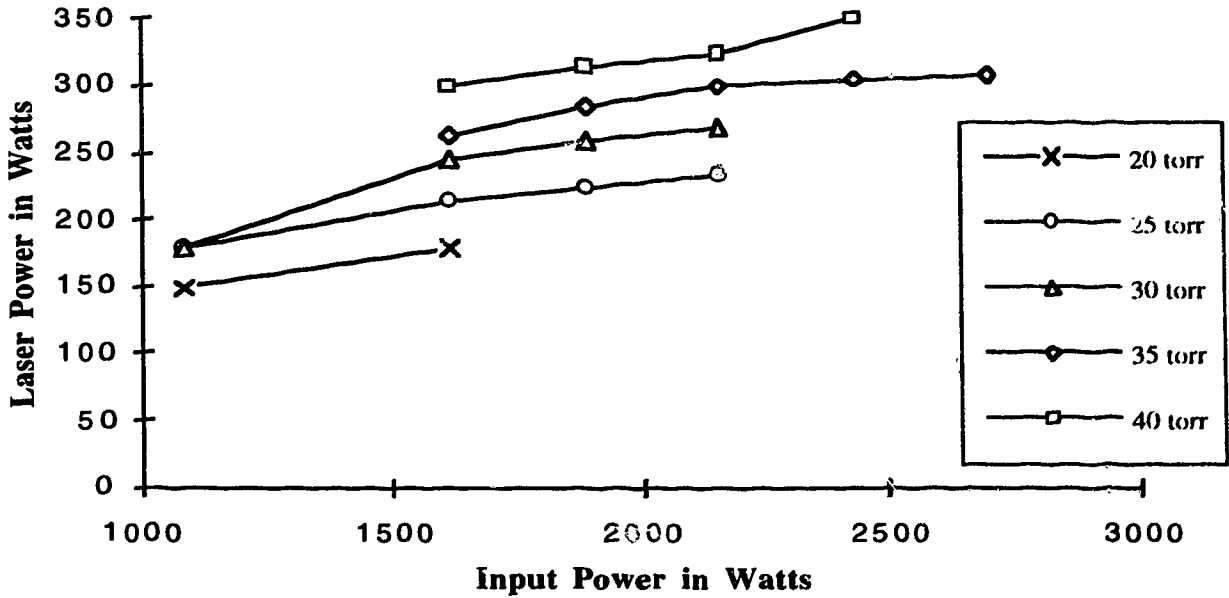


Figure 4.10 Laser Power with 25% Output Coupling.

Output Power with 35% Output Coupling

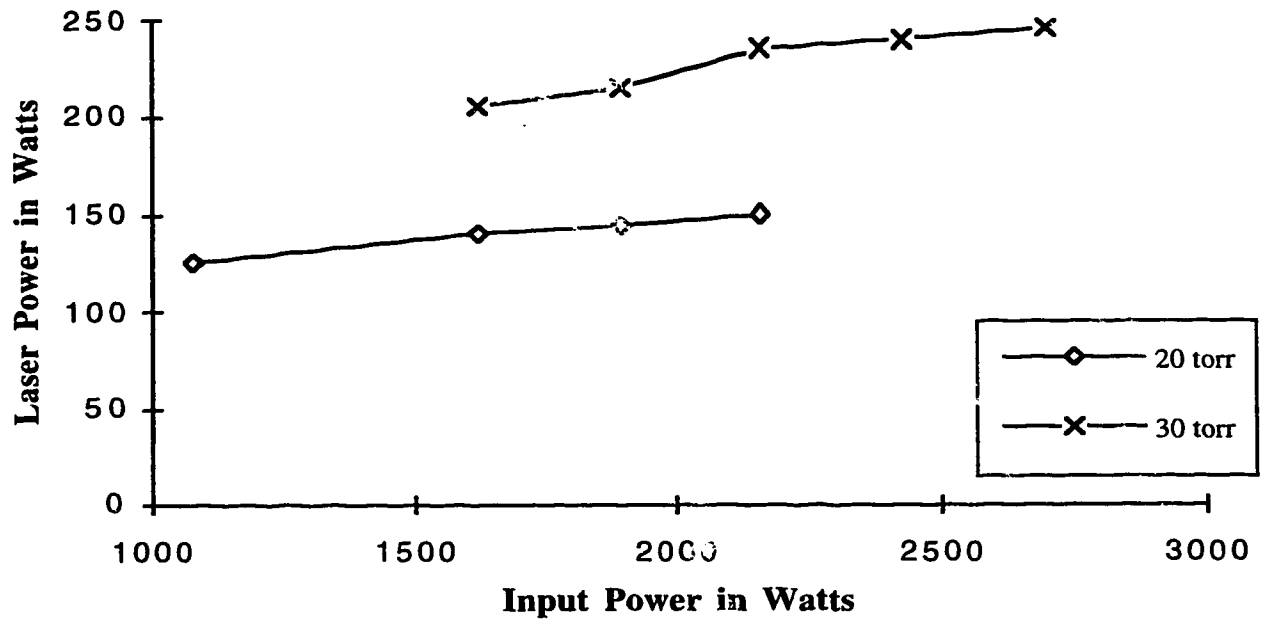


Figure 4.11 Laser Power with 35% Output Coupling.

Output Coupling vs. Output Power

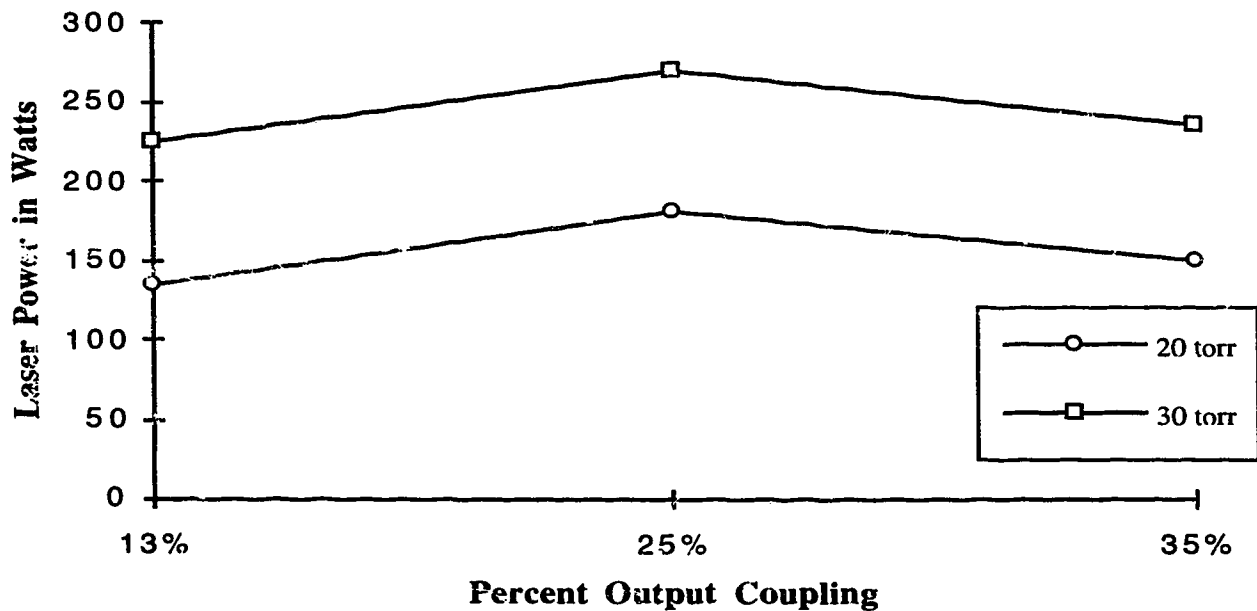


Figure 4.12 Optimum Output Coupling.

42, 58, and 75 cm from the front end of the electrode. Although visual inspection did indicate a very uniform discharge, no discharge uniformity measurements were actually performed. Figure 4.10 reveals that 350 watts of laser output was achievable with only 2.5 kW of input power. This result, corresponding to an efficiency of 14%, suggests that a fairly uniform discharge must indeed have been established. To verify this assumption, a newly developed theoretical model^{38,39} was used to predict uniformity curves for four different input power levels, utilizing the same inductors as in the actual experiment. Figure 4.13 illustrates this case. It can be seen from Figure 4.13 that as the gas is driven progressively harder, it assumes an optimum uniformity at a power loading of 4.6 W/cm². The RF drive level estimated under the conditions presented for 350 watts laser output extraction was 5 W/cm² (2500 watts input in an electrode of 500 cm²). Although still not optimal, this excitation level was nevertheless adequate to provide a reasonable approximation to a uniform discharge.

Driving the discharge harder makes the uniformity markedly worse. Given this fact, it is reasonable to expect that greater optical output power may be achieved, provided smoothing inductors are chosen to optimize discharge uniformity at higher RF drive levels.

4.2.2 Multi-Channel Optical Extraction

Once the highly encouraging results outlined above had been achieved in single channel experiments, multi-channel tests were initiated. For these experiments a radial slab array, shown pictorially in Figure 4.1, was used. Array excitation was accomplished via loops, coupled to the magnetic field of the resonant cavity around its short circuit

Discharge Uniformity vs. Drive Power

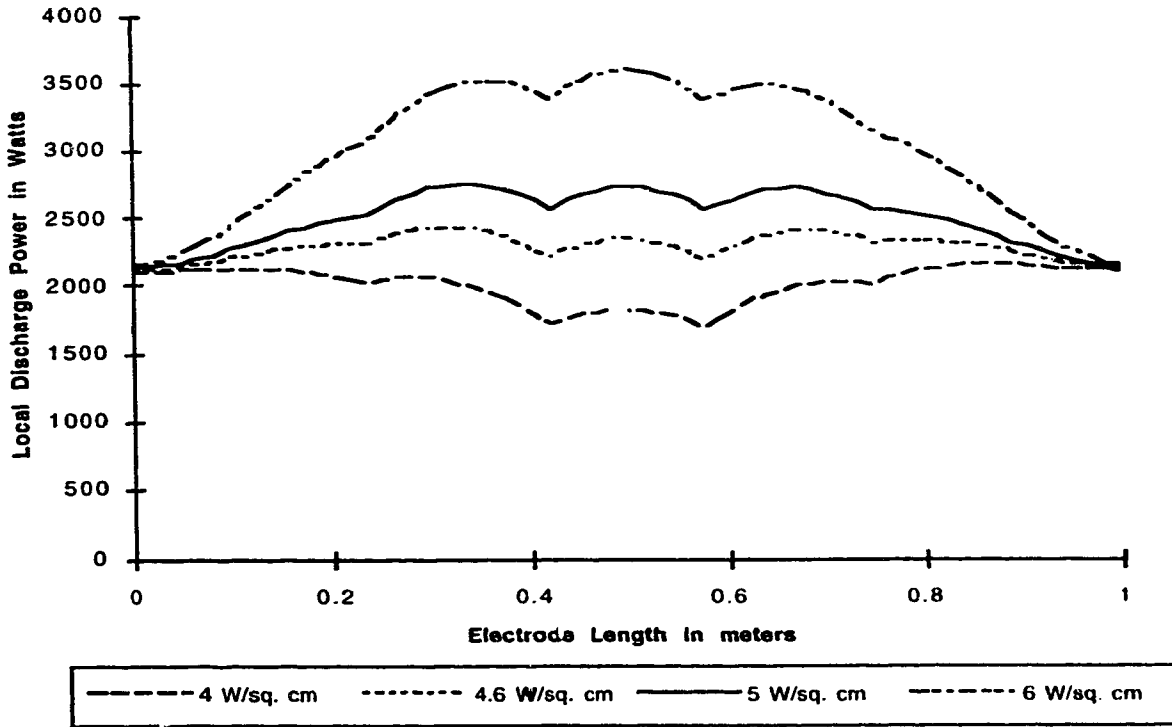


Figure 4.13 Theoretical Discharge Uniformity with 4 Inductors at 40 torr Gas Pressure.

plane. Since this particular T cavity had an inherently non-uniform magnetic field, progressively larger loops were required to drive the electrode elements, as energy was azimuthally extracted around the circumference of the cavity. To achieve equal drive to each electrode, the following loop sizes were used. The top eight loops were 23, 20, 18, 15.5, 15.5, 18, 20, and 23 cm respectively in length. Each loop had a common width of 4 cm. The 15.5 cm long loops were located 7.5° on either side of the top centerline of the cavity, while the remaining loops were mounted at 15° intervals along the circumference of the short circuit plane. Figure 4.14 illustrates this loop placement.

RF power was supplied from a triode oscillator described in Chapter 3. Optical output powers of up to 1300 watts have thus far been extracted from only eight channels.

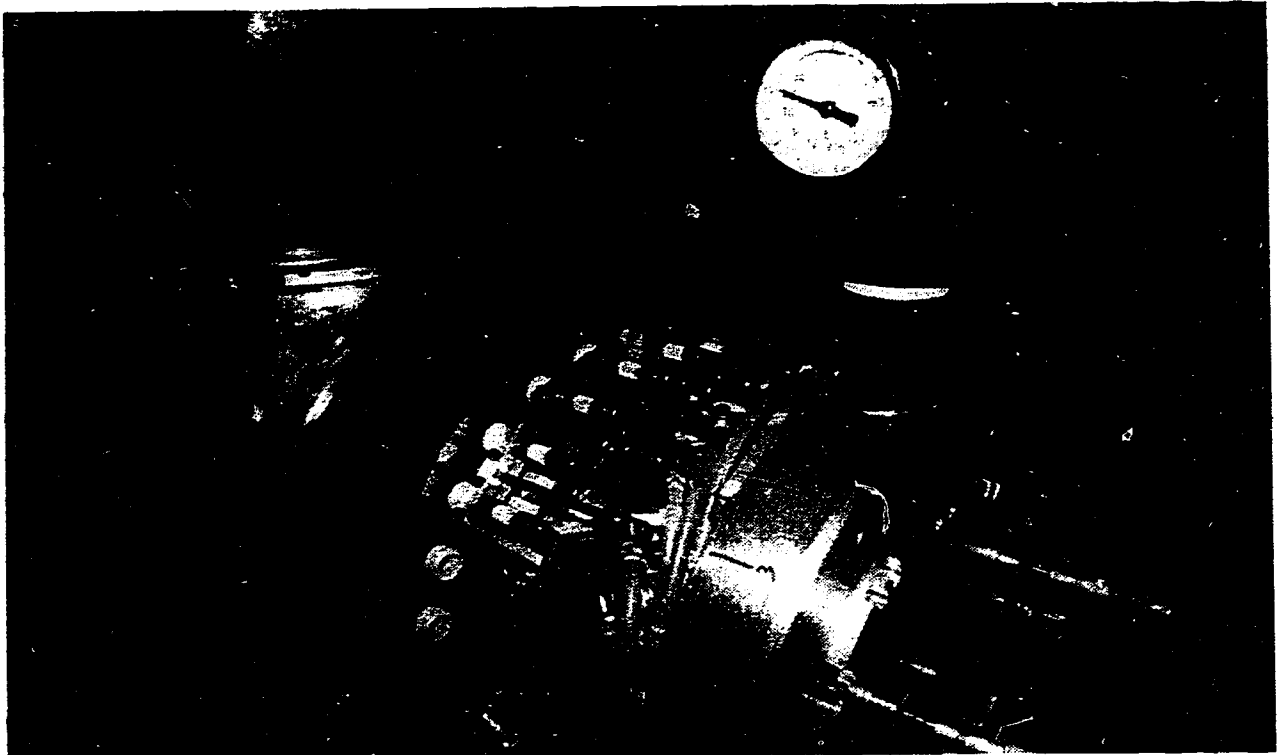


Figure 4.14 Loop Placement along Short Circuit Plane.

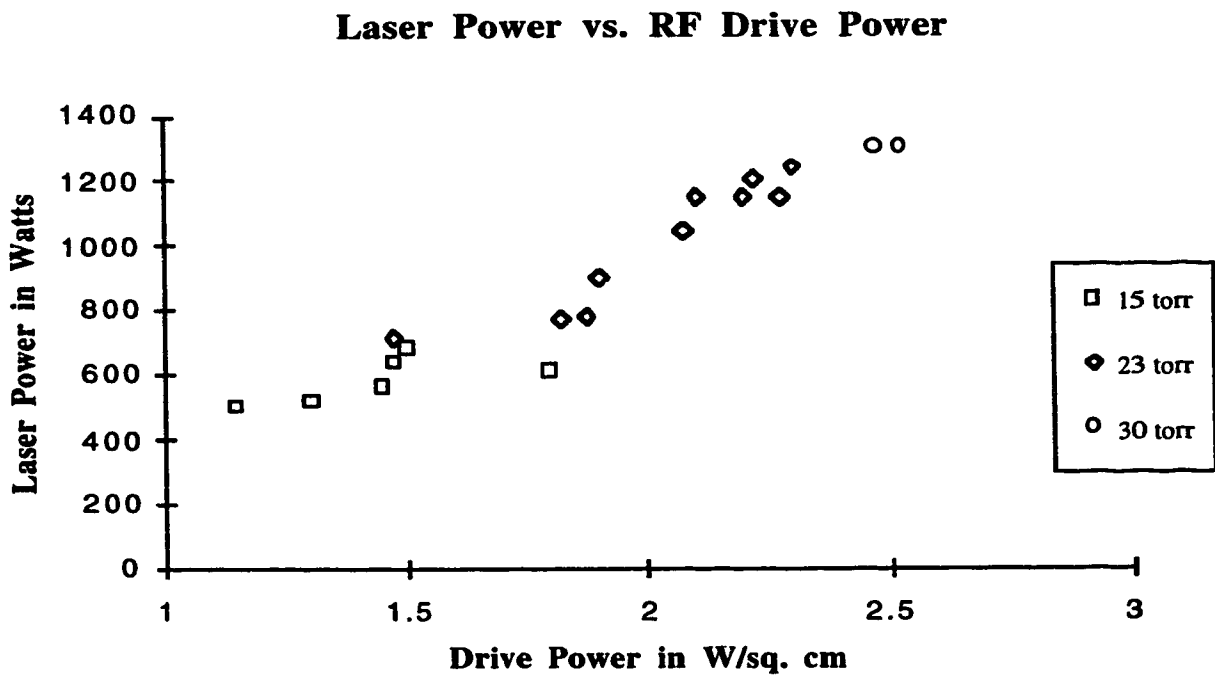


Figure 4.15 Multi-Channel Laser Power.

Output Power vs. Input Drive Power

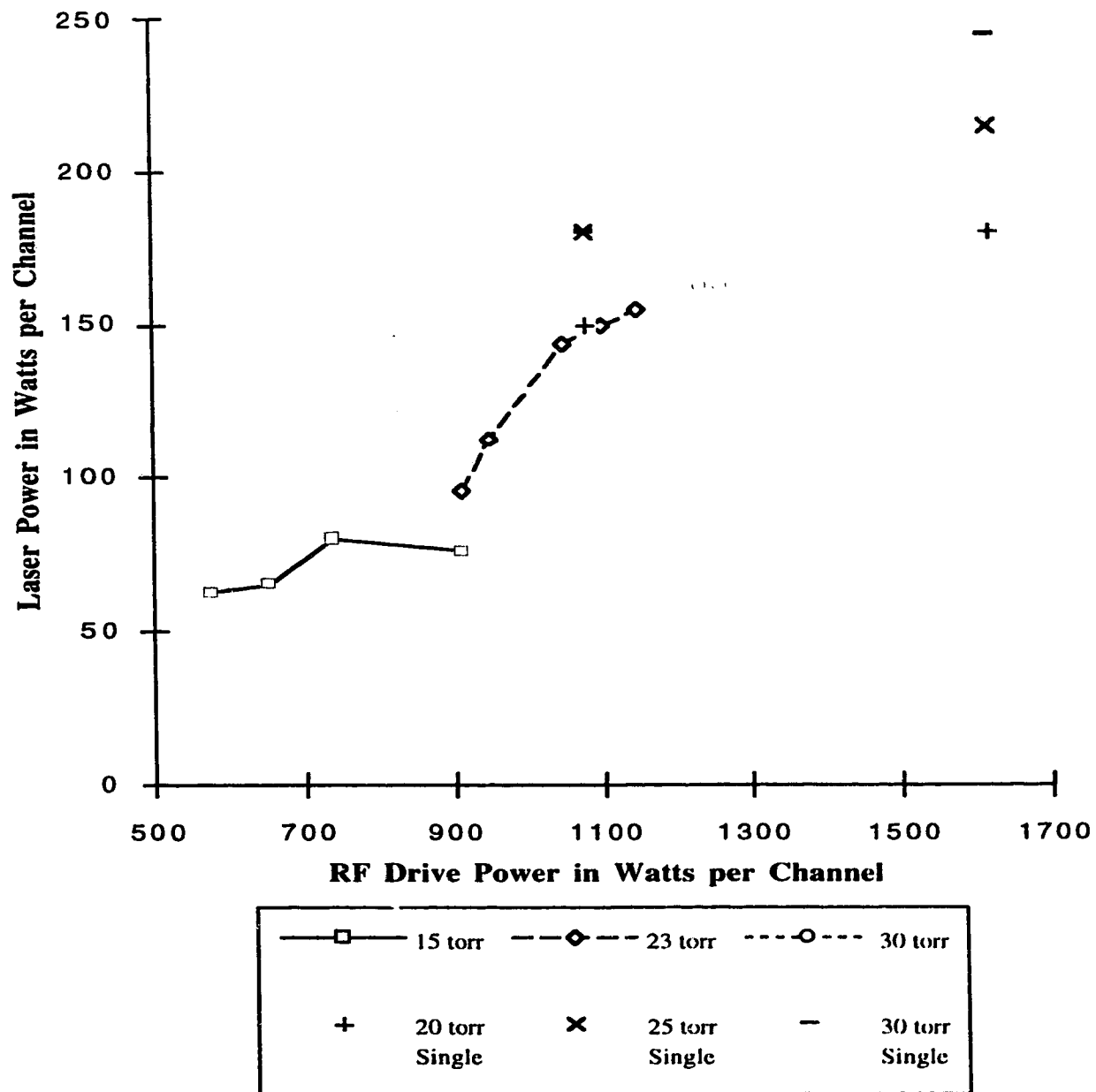


Figure 4.16 Comparison Between Single and Multi-Channel Laser Power.

Figure 4.15 illustrates measured laser power as a function of gas pressure and drive power. It is clear from the near linear dependence in Figure 4.15 of output power with RF input power and gas pressure, that even better performance is achievable with this system. Indeed, comparing these results in watts per channel with the single channel data, given in Figure 4.16, it is evident that power extracted as a function of drive power is consistent with single channel performance as illustrated in Figure 4.16 at the 1200 W, or 2.4 W/cm² level. This level is well below optimum for maximum optical extraction. Indeed, slab scaling laws predict an optimum RF drive level of 9 W/cm², at an operating pressure of 45 torr. Consequently, although the initial performance derived from this multi-channel system was impressive, it was well below its ultimate potential.

4.3 Optical Resonance

In the previous section, laser power was observed from several independent channels lasing at the same time. This section will briefly outline the types of modes supported within the parallel plate waveguide for the purpose of defining dimensional constraints which may prevent selective channels from lasing.

For lasing to occur, the length of the optical resonator must be an integer number of optical half wavelengths. This condition defines the frequency of the axial mode, and spacing between each axial mode is determined by $\frac{c}{2L_r}$, where L_r is the length between the mirrors and c is the velocity of light. If one mode is well out of phase with respect to this resonance condition, then lasing will not occur. Because of this, it is important to determine if any phase shifts can occur as the beam propagates between the mirrors. In a

parallel plate waveguide, such as the narrow gap slab electrode. three modes are supported, namely TEM, TE_n, or TM_n where n is an integer greater than one. With a TEM mode, both the phase and group velocities are the same. This implies that if the guide, or inter-electrode gap width varies, no phase shift will occur between modes in other channels. This is however not true for TE_n or TM_n modes which have a cutoff wavelength given by twice the electrode separation or 2d/n. Because of this fact, these waveguide modes will have group velocities less than the velocity of light in that medium. Consequently, phase shifts due to propagation delay will be experienced if each electrode gap does not have the same dimensions.

To examine this situation, the phase difference between two low order waveguide modes, specifically TE₁ or TM₁, is given in Table 4.1. These values are calculated from the formula for group velocity of a waveguide mode given by²⁴:

$$v_g = \frac{c\beta}{k} \quad (4.6)$$

where the propagation constant β , cutoff wavenumber k_c , and free space wavenumber k are given as:

$$\beta = \sqrt{k^2 - k_c^2} \quad k_c = \frac{n\pi}{d} \quad k = \omega\sqrt{\mu\epsilon} \quad (4.7)$$

Here d is again the gap dimension, while μ and ϵ are the gain medium permeability and permittivity seen previously.

For this test case, the phase difference is compared to that of a waveguide with an electrode separation of 3 mm. Illustrated in Table 4.1, a change in electrode separation to

2.7 mm gives rise to a total phase delay or shift of 0.0366λ within the optical resonator. For a laser with a resonator length of 1.06 m encompassing 100,000 wavelengths, this phase shift can be matched if the lasing mode has a frequency shift of only 11 MHz. Considering that at gas pressures of 40 torr, the pressure broadened linewidth is 260 MHz, this phase shift will not inhibit the lasing resonance condition. Consequently, for the Zodiac laser, fully resonant lasing occurs in all the independent waveguide channels simultaneously without any significant phase distortion at the output coupler caused by minor variations in electrode separation.

Table 4.1 Phase shift for TE_1 , or TM_1 mode after 1.06 m propagation with respect to a 3 mm parallel plate waveguide.

Guide dimension in mm	Phase shift in wavelengths
2.7	0.0366
2.8	0.0231
2.9	0.0109
3.0	0.0
3.1	-0.0099
3.2	-0.0189
3.3	-0.0271

4.4 Beam Characteristics

The optical resonator initially selected for extracting power from the multi-channel array had a toric configuration. This optical system is still classified as an unstable resonator, since the beam does not retrace its path before leaving the structure. Figure 4.17 is a schematic of this particular type of resonator. Beamlets start at the outer edge of the mirror and walk toward the center, where the entire beam is extracted through a 4.8 cm diameter central aperture in the front mirror. Since the optimum geometric coupling is 25%, each electrode tip should extend 12.5 mm past the edge of the central hole in the front mirror. In an ideal situation, the final beam pass would then be fully confined between the waveguide electrodes. Unfortunately, in the case of the 3 mm electrode gap used in these experiments, the last 3 mm of the laser beamlets' final pass was not confined. Consequently, propagation of this portion of the beam across the vacuum vessel was in a

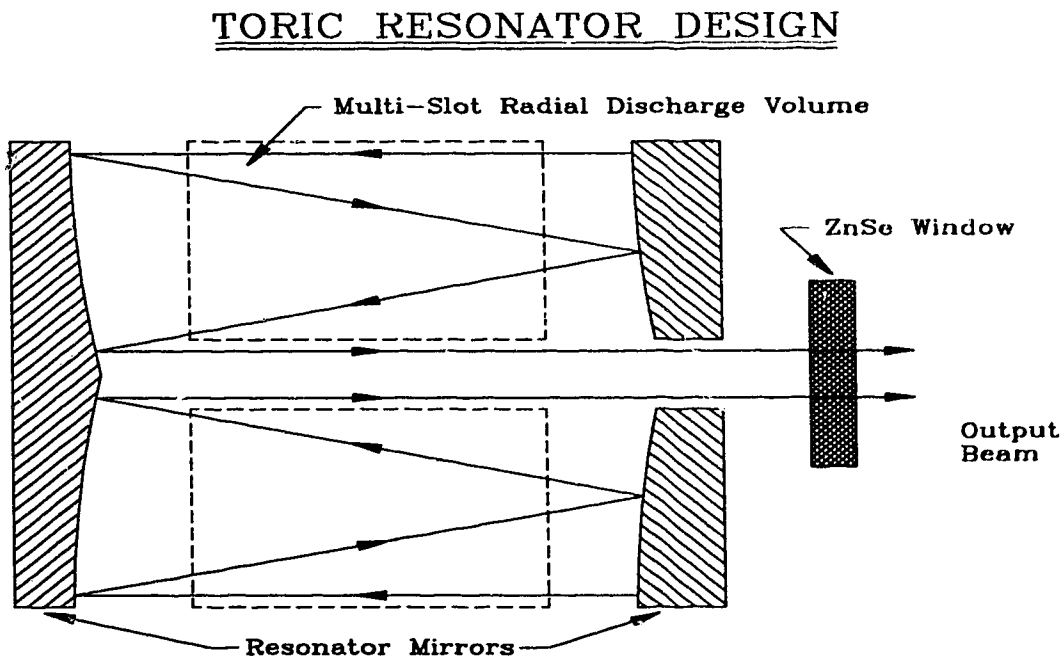


Figure 4.17 Toric Resonator.



Figure 4.18 Near Field Burn Pattern In Plexiglass.

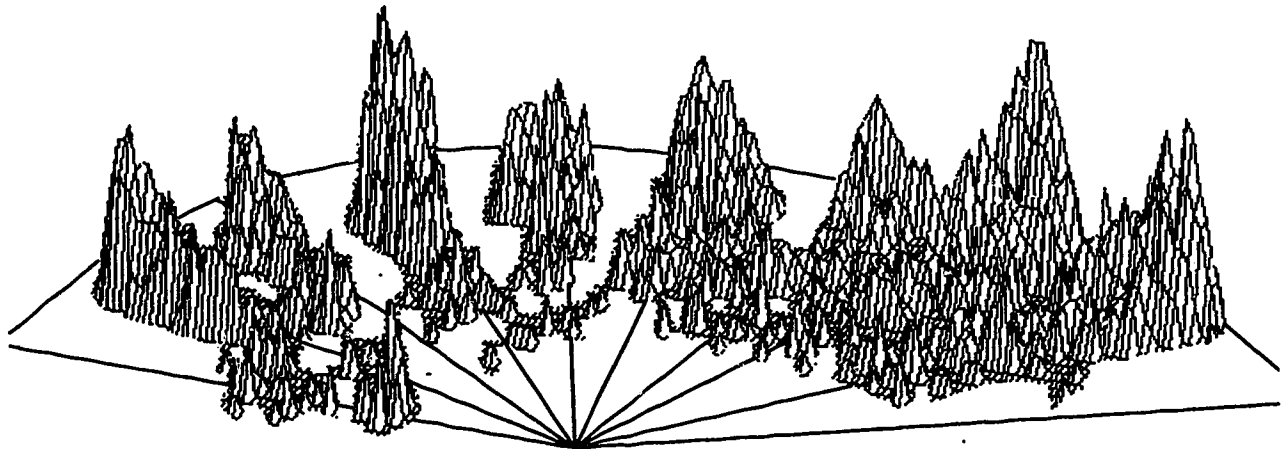


Figure 4.19 Digitized 3-D View Of Near Field Burn Pattern.

highly divergent free-space mode. Consequently, the beam profile was significantly degraded by excessive non-uniform divergence in the final optical pass.

Using the unstable Toric resonator of Figure 4.17, a near field burn pattern, illustrated Figure 4.18, was obtained in plexiglass. Figure 4.19 reconstructs a digitized, 3 dimensional view of this pattern. It is clear that the part of the beam that is confined between the electrodes on the last pass through the resonator exhibits a typical waveguide mode. However, the last 3 mm portion of the beam shows evidence of distortion. This aspect is a particularly sensitive feature of the toric resonator, which because of its increasingly sharp curvature near its centerline, can distort a beam in an azimuthal direction, if not confined within a waveguide. Consequently, beam distortion, as observed in this case will occur.

Notwithstanding the above situation, beam propagation experiments revealed that the overall divergence of the composite beam was quite low, and that it retained its profile exceedingly well. A picture of a burn pattern in plexiglass, taken 3.7 m from the output mirror is shown in Figure 4.20. As can be seen from this figure, divergence of the individual beamlets has caused the beam to lose all indication of the beamlets that created it. This azimuthal smoothing feature is expected, and is due to the much larger azimuthal divergence characteristic of a waveguide mode. One benefit is that the waveguide divergence has only a slight effect on the effective propagating divergence, since the beam is profiled in a radial array. This aspect was verified by beam propagation over a distance of 16.5 meters. In this case, the beam diameter only increased to about twice its near field profile. At a distance of 12 meters, the beam was focused with a 25 cm focal length lens. A typical



Figure 4.20 Far Field Burn Pattern In Plexiglass 3.7 m From Laser.

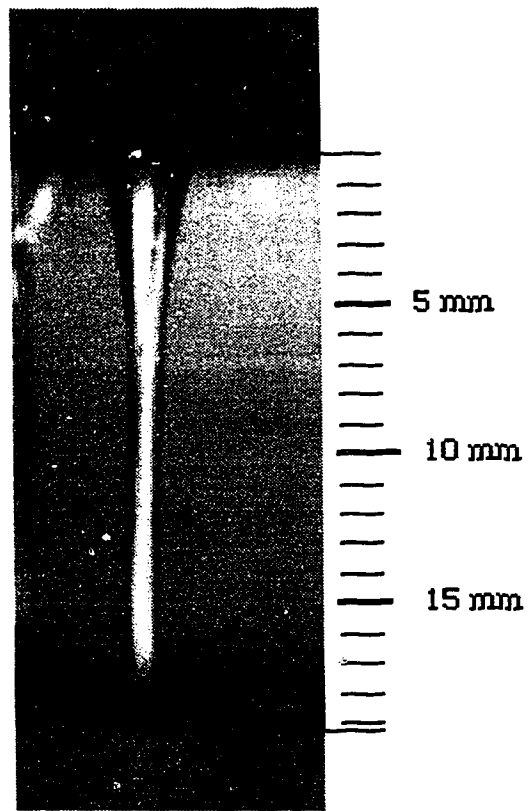


Figure 4.21 Focal Burn Pattern 12 m From Laser.

burn pattern obtained is shown in Figure 4.21. It can be seen here that the composite Zodiac laser beam has excellent focal properties. In order to better understand the beam quality obtained with these beamlets, a theoretical comparison between circular and asymmetrically profiled gaussian beams of similar shape will be discussed.

4.5 Focal Beam Quality

In determining the quality of a non phase locked zodiac laser beam, we first summarize the propagation characteristics of a single beam. An ideal laser beam has a gaussian intensity profile given by⁴⁰:

$$I(r) = \frac{2P}{\pi\omega^2} e^{-2r^2/\omega^2} \quad (4.8)$$

where ω is defined as the radial beam spot size, and P is the total power in the beam. The spot size of the propagating beam is described by³:

$$\omega^2(z) = \omega_0^2 + \frac{\lambda^2 z^2}{\pi^2 \omega_0^2} \quad (4.9)$$

where ω_0 is referred to as the beam waist, and is defined at the location where the radius of curvature of the wavefront is infinite. When such a gaussian beam is incident upon a lens of focal length f, a new beam waist ω'_0 will be created with a spot size given by³:

$$\omega'_0 = \frac{\omega_0 f}{z_0 \sqrt{1 - (f/z_0)^2}} \quad (4.10)$$

$$z_0 = \frac{\pi \omega_0^2}{\lambda} \quad (4.11)$$

For $f \ll z_0$ Eq. 4.10 simplifies to:

$$\omega'_0 = \frac{\lambda f}{\pi \omega_0} \quad (4.12)$$

For the case investigated here, we have a nearfield beam whose dimensions are 3 mm by 12 mm in cross-section, incident upon a lens with a focal length of 0.25 m. If the beam was an ideal gaussian profiled beam with circular symmetry having $\omega_0 = 6$ mm, Eq. 4.12 would predict a focal spot size of $\omega'_0 = 0.14$ mm. Due to the asymmetric nature of a slab laser beam, an averaged radial spot size is necessary to adequately describe the focal properties of the beam. With the present beam of 3×12 mm² in cross-section, an aspect ratio of 4:1 is defined. As previously documented²³, a beam of this aspect ratio can be assumed to be circularly symmetric, provided the combined stacked beam has sufficient overlapping of the individual beamlets. For the 24 channel zodiac discussed here, this is indeed the case. One exception is that a minimum of 12 adjacent beamlets are necessary to give a full fill factor. With the present system, there will be a small region in the focal plane that is not adequately described by this averaging effect due to the fact that only 8 adjacent channels were lasing.

Nevertheless, if such a composite stacked beam were incident upon a lens at the optic axis, we would have a new beam waist given by⁴¹:

$$W'_{r0} = \sqrt{2} \sigma'_{r0} \quad (4.13)$$

where the primed values signify far field quantities, and σ_{r0} is defined by⁴¹:

$$\sigma_{\omega}^2 = \frac{W_{x0}^2}{4} + \frac{W_{y0}^2}{4} \quad (4.14)$$

The upper case W is used to distinguish the actual laser beam spot size from the ideal gaussian beam spot size of ω . With W_{x0} , W_{y0} equal to 1.5, and 6 mm respectively we have focal spot sizes in these transverse dimensions given by $W'_{x0} = 0.606$ mm, and $W'_{y0} = 0.141$ mm. Consequently, the net combined beam with radial symmetry will have a spot size of $W'_{\omega} = 0.44$ mm, or a focal beam diameter of 0.88 mm.

Tests were done where the full beam consisting of 8 channels at 1 kW of power was propagated a distance of 12 m and then focused with a 25 cm focal length lens. The focal spot size as obtained by a hole drilled in a perspex rod at full power is shown in Fig. 4.21. Measurements of the hole diameter at a position of constant diameter, half way through the rod, gave a clean hole of ≈ 0.94 mm in diameter. For a gaussian beam, $\approx 86\%$ of the total power is contained within the focal spot size. Consequently, the focal beam diameter of Fig. 4.21 contains at least this amount of power. This was determined by the fact that there was no melting around the entrance aperture, signifying that virtually all of the laser beam power was focused within this spot size.

Another important beam parameter which can also be used in determining the focal spot size is the M^2 factor. The M^2 factor is defined as the product of the spatial variance and the spatial frequency variance of the beam. For an ideal symmetric gaussian this factor is equal to one. For an asymmetric gaussian beam with an aspect ratio of a , the M^2 can be derived as³⁷:

$$M^2 = \frac{(1 + a^2)}{2a} \quad (4.15)$$

For a beam with an aspect ratio of 4, the stacked beam will have a radial $M_r^2 = 2.125$ on the optic axis. Since the effective beam spot size is defined as⁴¹ $W_r = \sqrt{2}\sigma_r$, the M^2 factor can be applied to the focal spot size in the following manner³⁷:

$$W_r' = \frac{M_r^2 \lambda f}{\pi W_{r0}} \quad (4.16)$$

Equation 4.16 is identical to Eq. 4.12 for a circular gaussian beam, with the additional M^2 correction factor for a non ideal beam.

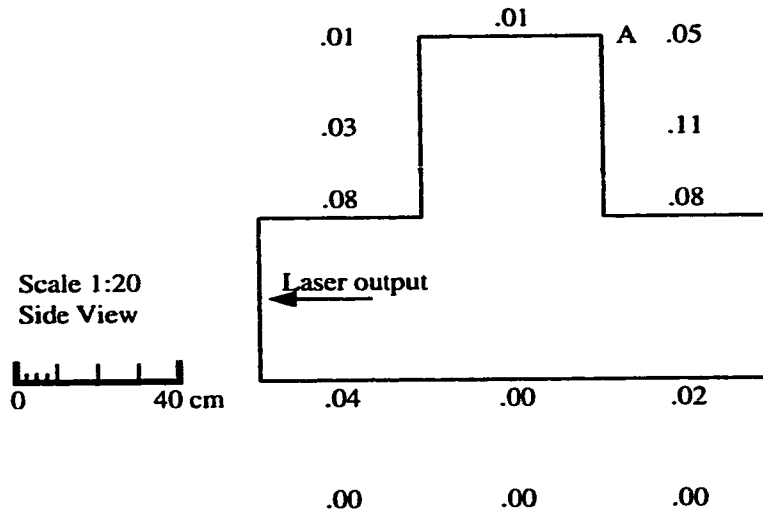
For the case studied here W_{x0} , W_{y0} are 1.5, and 6 mm respectively giving a combined spot size of $W_{r0} = 4.37$ mm. Substituting this value in Eq. 4.16 gives a focal spot size of 0.44 mm, or a focal beam diameter of 0.88 mm, identical to the previous calculation.

These results are even more impressive considering that only 8 out of the 24 channels were used. As such, the highly beneficial multiple beamlet power averaging effect made possible through radial beam stacking²³ was only partially achieved but was still sufficient to generate a adequately uniform and symmetric beam profile.

4.6 Radiation Safety

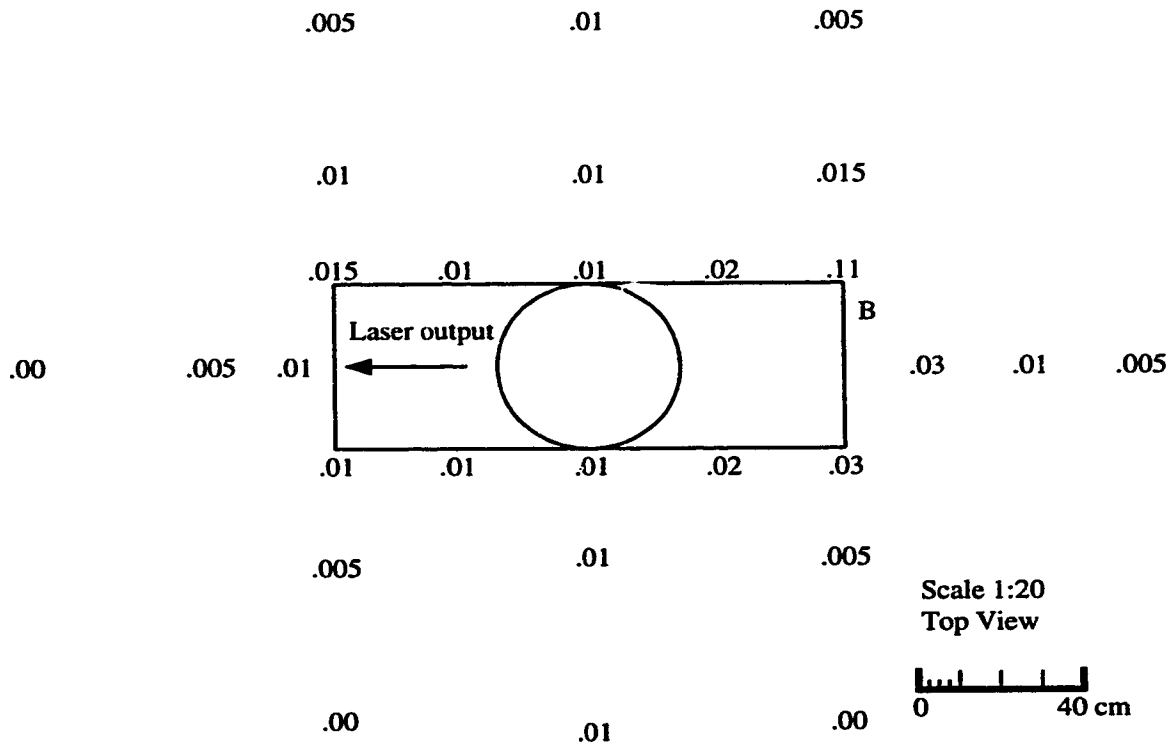
In all high power RF excited lasers there is a real concern of exposure to high levels of RF radiation. Radio frequency interference, or RFI, is a concern for any device operating outside the ISM radiation bands. Due to the cavity nature of the zodiac laser, there will always exist a full metal jacket enclosing the high strength RF fields. Since the skin depth of RF energy at these frequencies is only a few micrometers, a thin layer of metal is extremely effective in attenuating the RF fields. To determine the level of field strength around the zodiac laser, a Narda Model 8520 field strength meter was used which has a measuring bandwidth of 50 - 220 MHz. Illustrated in Figure 4.22, and 4.23 are these field strengths. The accepted standard for radiation exposure in the frequency range under consideration is 1 mW/cm^2 . As can be seen from these figures, the radiated field strength is quite low very close to the laser itself, with the exception of the filament power leads. The relatively higher fields at these leads can be reduced with better RF filtering inside the RF cavity itself, and is indeed being addressed in the next phase of the project.

The entire laser system is illustrated in Figure 4.24 and shows a photograph of the overall T cavity configured Zodiac laser in its present form. Front and rear water manifolds are also apparent in this illustration, along with front mirror mount micrometers, and a ZnSe output window.



A) Filament leads radiate 2.5 mW/cm^2 at this position
 Typical values along the filaments leads are $0.1\text{-}1.0 \text{ mW/cm}^2$

Figure 4.22 Zodiac Radiation Profile Side View.



B) Plate HT line radiates 0.13 mW/cm^2 at this position.
 All numbers are in mW/cm^2 for field strength readings

Figure 4.23 Zodiac Radiation Profile Top View.

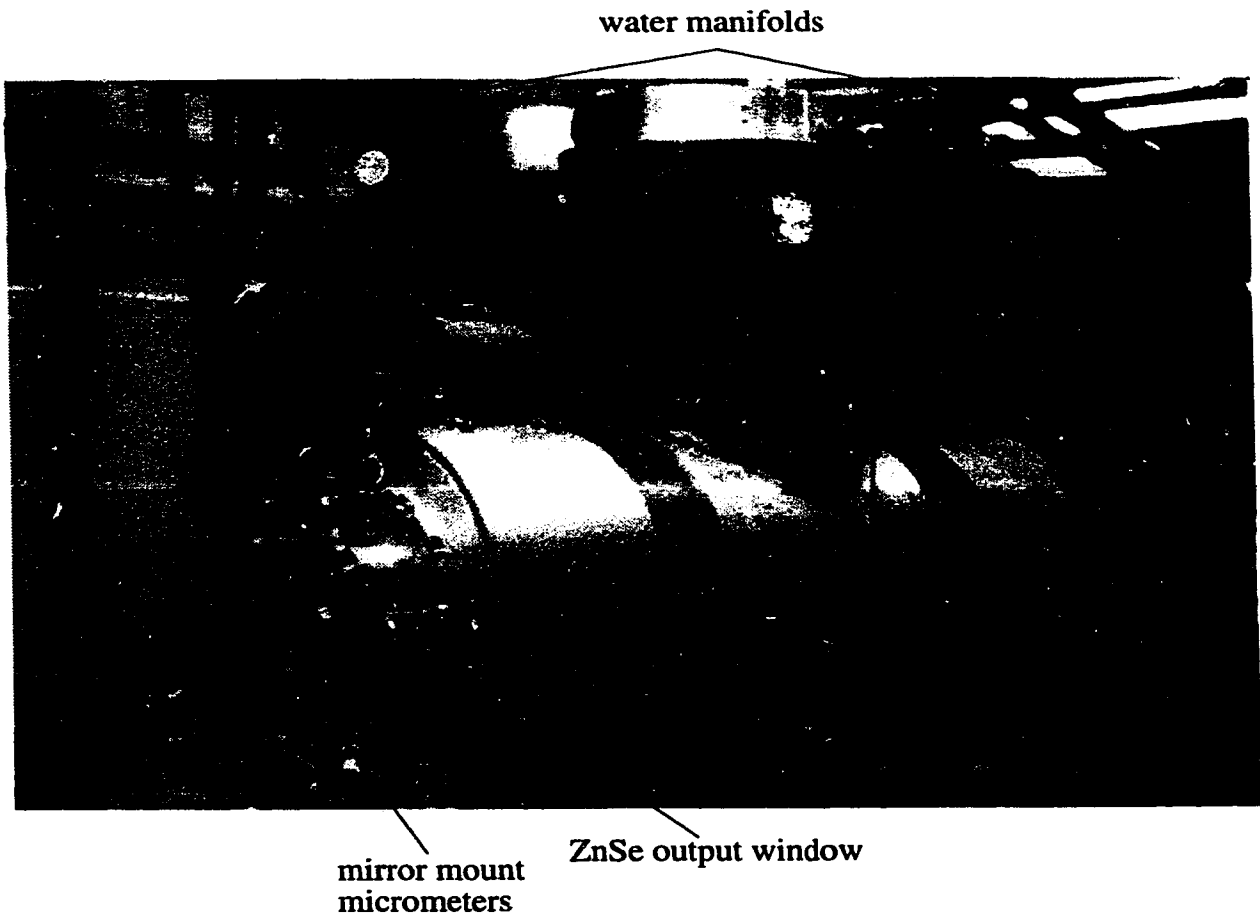


Figure 4.24 Zodiac Laser System.

Chapter 5

5.0 Conclusions And Proposals For Future Research

5.1 Summary Of This Investigation

Results in this thesis have clearly documented the viability of driving multi-channel systems with resonant cavities. In addition, the scalability of this radial array configuration to multi-kilowatt power levels in a compact and practical device has also been demonstrated. Furthermore, the effective utilization of a grid-separation, cavity-coupled triode oscillator has created a low cost, easy to operate source of high power RF energy necessary for multi-kilowatt laser excitation.

Quarter and half wavelength cavities have been described in detail, including the special case of a T shaped resonant structure. Length of these short-circuited coaxial transmission lines has been reduced by capacitive loading the open circuit junction, thereby yielding a resonant cavity of convenient length. Formulas for both loaded and unloaded cavity Q's have been presented. The need for heavy loading to achieve high cavity power transfer efficiency has also been demonstrated. Output energy coupling from many parallel loops, and the size of loops required for this purpose has been modeled in terms of cavity loading. Maximum cavity power transfer necessitated that the level of input and output coupling be the same. Measured efficiencies of $\approx 95\%$ with only four parallel 50Ω loads have proven that resonant cavities are effective and highly efficient power splitters. Equally important, the use of cavities as power splitters negates the need for matching networks, since the loops match virtually any impedance. In addition, power isolation is inversely proportional to the number of loops used in the system For a system with N

loops, each loop couples $1/N$ of the total power in the cavity. Because of all these features, cavity resonators are ideal for driving a large radial array CO_2 laser.

A triode oscillator was designed and constructed using two coaxial resonant cavities. Cavity resonant circuits were necessary since the RF output must be split into many independent sources. Traditional tank circuits cannot fulfill this essential requirement. Consequently, a non-conventional design employing dual cavity methodology was pursued.

Low mu tubes have inherently low cathode-anode isolation due to the loosely wound grid, which gives rise to significant electrical coupling of the two resonant circuits. This feature creates sufficient internal cathode-anode feedback that the two circuits of a tuned-grid, tuned-plate oscillator initiate and maintain oscillations in a self excited manner. Additional coupling may be added to augment feedback under high loading conditions. Although self bias is sufficient for constant triode loading, such as with resistive loads, a combination of fixed and self bias circuitry is preferred for dynamic loading conditions. This approach insures that the tube will be off until there is sufficient plate voltage to initiate oscillations. Once oscillations commence, the self bias circuitry further increases voltage on the grid into a more optimum operating region. Integrating the RF source into the laser head provides a self-tuned load circuit with the laser and triode oscillator sharing the same output cavity. Incorporation of the tube into the laser head requires a high circuit Q in order to achieve efficient power transfer to the discharge loads. This desired condition was shown not to occur in the case of 16 loops driving only 8 discharges. Dissipation losses of up to 60% were measured. A low operating plate current of

3.3 A and a plate voltage of 7 kV was clear evidence of such behavior, signifying an undercoupled circuit. Indeed, the manufacturer's specifications for this particular tube suggest optimum values of 7.7 A @ 7 k V. However, under a heavier plate loading situation, as in the case of four 50 Ω terminated loops coupling energy out of the cavity, efficiencies near 80% have been achieved with this same triode oscillator circuit. With 8 discharge loads, efficiencies of only 40% were achieved. Notwithstanding this heavily undercoupled situation, RF output power in excess of 25 kW has been extracted from the tube with efficiencies of 65%.

Uniform discharges have been achieved with the help of a theoretical model to design the size and placement of inductors, and less rigorously through experimental observation. Extensive investigation of the number, placement, and size of inductors revealed that a sufficiently uniform discharge, with power uniformity to within 10% across the electrode length, could be achieved with only two inductors. Although limited in output power, 8 discharges with acceptable uniformity were sustained at pressures up to 20 torr, under input RF drive powers of 10 kW. Optical powers in excess of 1,200 watts were observed at these drive levels. It was further shown that independent slab laser beamlets exit the laser cavity, and that the composite radial beam profile so generated, produces a beam with circular symmetry, low beam divergence, and excellent focal properties, without need for beam conditioning optics. This feature was possible due to the unique nature of radial beam stacking, inherently provided by the zodiac geometry.

5.2 Proposals For Future Research

The T shaped cavity resonator initially employed for tube integration revealed an inherent flaw, in that uniform magnetic fields were not produced throughout the structure. This unsatisfactory condition stemmed from the fact that there was only one RF feed point into the cavity. Consequently, a major distortion of the circulating magnetic field occurs in close proximity to the T junction. To eliminate this effect, the RF source should be kept separate from the laser head cavity. RF drive to the laser head should then be accomplished with at least two diametrically opposing feeds, and preferably more, in order to establish a uniform and symmetric field distribution within the cavity. An additional benefit derived from separating the RF source is that of increasing the laser head cavity Q. Since loading effects on the tube are separated from the laser head cavity, the laser head cavity Q will increase significantly. Consequently, power transfer efficiencies from the laser head to the gas discharge will increase, while at the same time providing a means of varying the triode plate loading. This is due to the fact that the output cavity of the triode would be separated from the laser head cavity, so the loading of each cavity could be adjusted independently. With such an arrangement, the tube could be operated at near optimum loading, and output powers in excess of 60 kW should be possible. With this increase in available RF drive power, plus symmetric magnetic fields established within the laser head cavity, it should be a simple task to drive all 24 electrodes efficiently.

Once the system has been made fully operational, additional investigations of radial beam parameters in terms of material processing applications can be undertaken. Other significant features such as M^2 , beam compaction techniques, phase locking, and resonator design can also be studied. Pulse shaping experiments could also be carried out.

This would require circuitry for pulse modulation of the oscillator. Under pulsed output, performance parameters with respect to peak power, and energy per pulse can be optimized for applications such as paint stripping.

References

- 1 C.K.N. Patel, *Interpretation of CO₂ Optical Maser Experiments*, Phys. Rev. Lett., **12**, 588, (1964).
- 2 K.D. Laakmann, *Waveguide gas laser with high frequency transverse discharge excitation*, U.S. Patent #4,169,251.
- 3 Amnon Yariv, *Optical Electronics*, CBS College Publishing, New York, (1985).
- 4 H.J. Baker, I. Laidler, *Electrical characterization of pulsed and CW fast axial flow RF excited CO₂ lasers*, SPIE Vol. **1225**, 349, (1990).
- 5 W. Schock, Th. Hall, E. Wildermuth, K. Wessel, E. Gehringer, P. Schnee, F. Hadinger, *Compact transverse flow CO₂ laser with RF excitation*, SPIE Vol. **1031**, 76, (1988).
- 6 R. Nowack, H. Opower, U. Schaefer, K. Wessel, Th. Hall, H. Kruger, H. Weber, *High Power CO₂ Waveguide Laser of the 1 kW Category*, SPIE Vol. **1276**, 18, (1990).
- 7 R.T. Brown, L.A. Newman, M.W. Murray, R.A. Hart, *Large-Volume Pulsed-RF Excited Waveguide CO₂ Lasers*, IEEE J. Quantum Electron, **QE-28**, 404, (1992).
- 8 D. He, D.R. Hall, *Frequency Dependence in RF Discharge Excited Waveguide CO₂ Lasers*, IEEE J. Quantum Electron. **QE-20**, 509, (1984).
- 9 P.P. Vitruk, H.J. Baker, D.R. Hall, *The characteristics and stability of high power transverse radio frequency discharges for waveguide CO₂ slab laser excitation*, J.Phys. D:Appl. Phys., **25**, 1767, (1992).
- 10 D. He, D.R. Hall, *A 30 watt radiofrequency excited waveguide CO₂ laser*, Appl. Phys. Lett. **43**, 726, (1983).

- 11 H. Hugel, W. Schock, *Compact CO₂ laser with transverse rf excitation*, Presented at CLEO, Phoenix, AZ, 1982, paper THN3.
- 12 P.P. Vitruk, N.A. Yatsenko, *Small intermediate-power CO₂ grooved-waveguide laser with rf pumping*, Sov. Tech, Phys. Lett. **16**, 163, (1989).
- 13 O.R. Kachurin, F.V. Lebedev, A.P. Napartovich, *Properties of an array of phase-locked CO₂ lasers*, Sov. J. Quantum Electron. **18**, 1128, (1988).
- 14 P.E. Jackson, H.J. Baker, D.R. Hall, *CO₂ large-area discharge laser using an unstable-waveguide hybrid resonator*, Appl. Phys. Lett. **54**, 1950, (1989).
- 15 C.J. Shackleton, K.M. Abramski, H.J. Baker, D.R. Hall, *Lateral and transverse mode properties of CO₂ slab waveguide lasers*, Opt. Commun. **89**, 423, (1992).
- 16 K.M. Abramski, A.D. Cooley, H.J. Baker, D.R. Hall, *Power scaling of large-area transverse radio frequency discharge CO₂ lasers*, Appl. Phys. Lett., **54**, 1833, (1989).
- 17 A. Lapucci, G. Cangioli, *Triple slab radio-frequency discharged CO₂ laser*, Appl. Phys. Lett., **62**, 7, (1993).
- 18 A. Lapucci, G. Cangioli, *Phase-Locked Operation of a Compact Three-Slab-Sections Radiofrequency Discharge CO₂ Laser*, IEEE J. Quantum Electron. **QE-29**, 2962 (1993).
- 19 A. Lapucci, F. Rossetti, *Experimental characterization of RF-discharged open slab CO₂ lasers*, Opt. Laser Technol., **27**, 167, (1995).
- 20 E.F. Yelden, H.J.J. Seguin, C.E. Capjack, S.K. Nikumb, *A multi-channel slot discharge CO₂ laser employing a toric unstable resonator*, Opt. Commun. **82**, 503, (1991).

- 21 E.F. Yelden, H.J.J. Seguin, C.E. Capjack, S.K. Nikumb, H. Reshef, *Toric unstable CO₂ laser resonator: an experimental study*, Appl. Opt. **31**, 1965, (1992).
- 22 E.F. Yelden, H.J.J. Seguin, C.E. Capjack, H. Reshef, *Phase-locking phenomena in a radial multislotted CO₂ laser array*, J. Opt. Soc. Am. B., **10**, 1475, (1993).
- 23 E.F. Yelden, S.W.C. Scott, J.D. Stroschein, H.J.J. Seguin, C.E. Capjack, H.W. Reshef, *Symmetry Enhancement and Spot-Size Reduction Through Radial Beam Stacking in a Multichannel CO₂ Laser Array*, IEEE J. Quantum Electron. **QE-30**, 1868, (1994).
- 24 David M. Pozar, *Microwave Engineering*, Addison-Wesley, New York (1990).
- 25 W. Tinga, *Microwave Engineering EE597*, University of Alberta, (1993).
- 26 F.E. Terman, *Radio Engineers' Handbook*, McGraw-Hill, New York (1943).
- 27 R.F. Arnesen, *CAD does coupling loops for tunable coax cavities*, Microwaves & RF, **25**, No. 12, 137, (1986).
- 28 H.J. Reich, ed., *Very High Frequency Techniques*, McGraw-Hill, New York (1947).
- 29 E.F. Yelden, H.J.J. Seguin, C.E. Capjack, S.K. Nikumb, *Multichannel slab discharge for CO₂ laser excitation*, Appl. Phys. Lett., **58**, 693, (1991).
- 30 F.E. Terman, *Radio Engineers' Handbook*, McGraw-Hill, p. 445, New York (1943).
- 31 D.R. Hamilton, J.K. Knipp, J.B. Horner Kuper, *Klystrons And Microwave Triodes*, p. 174, New York (1948).
- 32 R.L. Sinclair, J. Tulip, *Parameters affecting the performance of a rf excited CO₂ waveguide laser*, J. Appl. Phys. **56** (9), 2497 (1984).

- 33 D. He, D.R. Hall, *Longitudinal Voltage Distribution in Transverse RF Discharge Waveguide Lasers*, J. Appl. Phys. **54** (8), 4367 (1983).
- 34 Young-Myung Kim, Chan Eui Youn, Jung Woong Ra, Yeong Sik Kim, *Method for reducing the longitudinal voltage variation in transverse radio-frequency discharge waveguide lasers*, J. Appl. Phys. **67** (2), 1127 (1990).
- 35 L.A. Newman, R.A. Hart, *Technology Trends in Low to Medium Power CO₂ Lasers*, SPIE Vol. **737**, 36 (1987).
- 36 P.P. Vitruk, H.J. Baker, D.R. Hall, *Similarity and Scaling in Diffusion-Cooled RF-Excited Carbon Dioxide Lasers*, IEEE J. Quantum Electron, **QE-30** (7) 1623 (1994).
- 37 J.D. Stroschein, personal communication.
- 38 J.D. Stroschein, W.D. Bilida, H.J.J. Seguin, C.E. Capjack, *Enhancing Discharge Uniformity in a Multi-kilowatt Radio Frequency Excited CO₂ Laser Array*, accepted for publication Appl. Phys. Lett.
- 39 J.D. Stroschein, W.D. Bilida, H.J.J. Seguin, C.E. Capjack, *Computational Model of Longitudinal Discharge Uniformity in RF-Excited CO₂ Slab Lasers*, Submitted to IEEE J. Quantum Electron.
- 40 A.E. Siegman, *Lasers*, University Science Books, Mill Valley, California (1986).
- 41 A.E. Siegman, *New Developments in Laser Resonators*, SPIE Vol. **1224**, 2-14 (1990).